



Some Topics in Topological Mechanics

Citation

Plumb-Reyes, Thomas B. 2021. Some Topics in Topological Mechanics. Doctoral dissertation, Harvard University Graduate School of Arts and Sciences.

Permanent link

<https://nrs.harvard.edu/URN-3:HUL.INSTREPOS:37370208>

Terms of Use

This article was downloaded from Harvard University's DASH repository, and is made available under the terms and conditions applicable to Other Posted Material, as set forth at <http://nrs.harvard.edu/urn-3:HUL.InstRepos:dash.current.terms-of-use#LAA>

Share Your Story

The Harvard community has made this article openly available.
Please share how this access benefits you. [Submit a story](#).

[Accessibility](#)

HARVARD UNIVERSITY
Graduate School of Arts and Sciences




DISSERTATION ACCEPTANCE CERTIFICATE


The undersigned, appointed by the


Harvard John A. Paulson School of Engineering and Applied Sciences
have examined a dissertation entitled:

“Some Topics in Topological Mechanics”

presented by: Thomas B. Plumb-Reyes

Signature  _____
Typed name: Professor L. Mahadevan

Signature  _____
Typed name: Professor Z. Suo

Signature  _____
Typed name: Professor V. Manoharan

August 31, 2021

Some Topics in Topological Mechanics

A DISSERTATION PRESENTED
BY
THOMAS B. PLUMB-REYES
TO
THE DEPARTMENT OF APPLIED PHYSICS

IN PARTIAL FULFILLMENT OF THE REQUIREMENTS
FOR THE DEGREE OF
DOCTOR OF PHILOSOPHY
IN THE SUBJECT OF
APPLIED PHYSICS

HARVARD UNIVERSITY
CAMBRIDGE, MASSACHUSETTS
AUGUST 2021

©2021 – THOMAS B. PLUMB-REYES
ALL RIGHTS RESERVED.

Some Topics in Topological Mechanics

ABSTRACT

We apply mechanical theories of the elasticity of thin rods and topological theories of entanglement to model experimental systems of detangling hair with a comb and the internal structure of bird's nests. By applying these theoretical frameworks to novel systems, we open up new ways of studying classes of problems including the above, the carding and decarding of textiles, and biologically-inspired materials engineering. In the first section, we take a pedagogical approach to analyzing the topology, geometry and mechanics of a single elastic filament. We walk advanced undergraduate or early graduate student readers through Cosserat elastic rod theory. We then introduce a topological quantity called Link and connect it to the geometry and mechanics of a single filament. In the experimental sections that follow, we investigate physical entanglement in two model systems: detangling filaments in a double helix and analyzing the relationship between physical stress and internal geometry and topology of a system of randomly packed steel rods. In the first system, we use a double helix filament geometry as a simplified model for detangling hair by combing. We investigate the relationships between geometry, mechanics and topology of the double helix to analyze the key role that topology plays in the mechanics of detangling. We also use the model to design a feedback-driven hair combing robot that uses force-sensing and computer vision to find an optimal hair combing procedure. In the second system, we use a network of randomly packed steel rods as a simplified model to study the roles of geometry and topology in the mechanical properties of bird's nests made of entangled sticks. Finally, we discuss areas for further research including: studying detangling in more varieties of human and animal hair, characterizing more complex hair interactions using topology and studying disentanglement in randomly packed steel rods.

Contents

o	INTRODUCTION	1
1	MODELING ELASTIC FILAMENTS	7
1.1	Introduction	9
1.2	Geometry, topology, and mechanics of elastic filaments	10
1.3	Analyzing a helical spring	23
1.4	Conclusion	26
2	COMBING A DOUBLE HELIX	28
2.1	Abstract	30
2.2	Introduction	31
2.3	Minimal model of hair curl	31
2.4	Experimental observations of combing	34
2.5	Numerical analysis of combing	40
2.6	Optimal combing strategy	45
2.7	Conclusions	46

2.8	Appendix	47
3	DETANGLING HAIR USING FEEDBACK-DRIVEN ROBOTIC BRUSHING	62
3.1	Abstract	64
3.2	Introduction	64
3.3	Methods	67
3.4	Experimental Setup	75
3.5	Experimental Results	77
3.6	Discussion & Conclusion	85
4	TOPOLOGY AND MECHANICS OF ENTANGLED RIGID RODS	87
4.1	Abstract	89
4.2	Introduction	89
4.3	Results	90
4.4	Discussion	97
4.5	Materials and Methods	98
4.6	Supplemental information	101
5	CONCLUSION AND FUTURE DIRECTIONS	107
	REFERENCES	118

Listing of figures

o.1	'La Coiffure'	3
o.2	Large bird's nests	5
1.1	Examples of modeling filaments	9
1.2	Visualizing geometric torsion	12
1.3	Geometric torsion vs. intrinsic twist	14
1.4	Cosserat rod theory	15
1.5	Two curves with varying linking number	16
1.6	Oriented link crossings	17
1.7	Planar rod with non-zero twist	18
1.8	Converting between twist and writhe	20
1.9	Link, twist, and writhe of a single helix	25
1.10	Stretching a helical spring	27
2.1	Characterizing and counting hair tangles	32
2.1	(continued)	33

2.2	Experimental combing of a double helix	38
2.2	(continued)	39
2.3	Numerical analysis of combing a double helix	42
2.3	(continued)	43
2.4	Optimal combing strategy	46
2.5	Numerical analysis of hair curl interactions	48
2.6	Combing force with varying tine radius	53
2.7	Variations in force-displacement curves	54
2.8	Link current out of the double helix	55
2.9	Table: double helix simulation parameters	59
2.10	Table: hair crossings simulation parameters	59
2.11	Experimental image of combing a double helix	60
2.12	Computational image of combing a double helix	61
3.1	Robotic hair brushing diagram	65
3.2	Minimal model for hair combing	70
3.3	Hair combing optimization problem	72
3.4	Hair combing vision pipeline	76
3.5	Experimental setup for robotic brushing	77
3.6	Hair brushing force timeseries	78
3.7	Maximum force for different brushstrokes and hair curliness	79
3.8	Brushing force for different speeds	79
3.9	Optimized function for starting brush height	80
3.10	Maximum force and brushing length for different hair curliness	82
3.10	(continued)	83

3.1.1	Comparing different brushing strategies	84
4.1	Bird's nests and entangled rods	90
4.2	Mechanical testing of entangled rod networks	93
4.3	Visualizing entangled rod networks	95
4.4	Statistics of entangled rod network	96
4.5	Rod volume fraction as a function of aspect ratio	101
4.6	Cyclic softening of entangled rod network	102
4.7	Orientalional distribution of entangled rod network	103
4.8	Rod contact number distribution	104
4.9	Identifying rods after a watershed transform	105
5.1	Combing real hair	108
5.2	Borromean rings	110
5.3	Disentangling randomly packed rods	111

TO MY FAMILY, BIRTH AND CHOSEN.

Acknowledgments

I COULD NOT HAVE COMPLETED THIS WORK ALONE, and I would like to acknowledge the many wonderful people who helped me along the way. My advisor, L. Mahadevan, was an endless source of scientific knowledge and enthusiasm throughout my time at Harvard. I am also thankful for the support and advising of my other thesis committee members, Profs. Zuo and Manoharan. My collaborators Nicholas Charles, Josie Hughes, Prof. Daniela Rus, Yeonsu Jung, H. Greg Lin, Hunter King and Elodie Couttenier all made invaluable contributions to the work presented here.

0

Introduction

What is the difference between a pile of sticks and a bird's nest? What is the optimal strategy for combing hair? Simplified answers to these questions can be intuited through experience or common sense. However, a scientific approach to resolving these questions incorporates theories of elasticity and topological notions of entanglement. The physical component at the heart of both hair combing and bird's nests is the thin elastic rod (or string or filament). Rods appear ubiquitously across many different facets of the human and natural worlds: from detangling headphones in your pocket, to bridge construction, to unravelling DNA during transcription and duplication. What particularly unites hair combing and bird's nests is the many-body and geometrically complex nature of the two systems.

When combing hair to detangle it, the soft individual hair fibers are easily contorted by the movement of the comb. However, through their interactions with each other, they can be entangled and become materially stiff, causing sharp increases in the force against the comb. This stiffness arises from what is colloquially called a tangle and it leads to the pain and frustration often associated with combing and taming hair. Figure 0.1 depicts a scene of the quotidian combing task rendered by Edgar Degas, featuring a young woman with an enigmatic facial expression and bodily position that could convey pain, frustration, boredom—or a mixture thereof. The ideal combing strategy, as many people who deal with long hair may already know, is to start near the free hair ends and work upwards towards the scalp. In the Degas painting, the maid holds the ostensibly detangled section of the hair in her left hand, while the sitter's hand suggests more painful tangles closer to the scalp. Shorter brush strokes can also ease the process of detangling hair, but at the expense of a longer time to completion. The maid combing the hair is presumably sensitive to the feelings of her employer and adjusting her behavior accordingly. The feedback-controlled hair combing robot described in Chapter 3 of this dissertation presents the possibility of optimized, responsive help combing hair in the twenty-first century.

Analyzing the problem of entanglement in hair combing is complicated by the many filaments



Figure 0.1: Combing the Hair ('La Coiffure'), Edgar Degas, c. 1896, oil on canvas, The National Gallery, UK.

potentially involved as well as the extended nature of their interactions. Inserting a comb and moving it through a bundle of interacting hairs (in this dissertation, we call this a curl) can necessitate accounting for 2-, 3-, ..., n -body interaction types that could change character and position over the length of a single brush stroke, as well as affect the up- and downstream configurations of the hairs. We simplify this problem by first considering the dry combing (no treatments or lubricants) of hair, where the hairs have an average radius of curvature on the order of their length (i.e., relatively straight). Through computational and experimental analysis we determine that, for this type of hair, 2-body intersections (used as an upper bound on entanglement) dominate higher order interactions between hairs over the length scale of the curliest section of the hairs (the free ends).

Focusing the 2-body regime, we create a minimal model to explore hair combing: a double helix, fixed at one end and free at the other, and pierced by a single stiff tine and pulled until the helices are

separated. This model gives us some important results for understanding the fuller hair combing problem. Using a combination of experiments and numerical modeling, we are able to explore the effects of hair geometry (in the form of the pitch and radius of the double helix) and starting comb position on the mechanics of hair detangling. We also identify the role of an important topological quantity in the hair detangling process: Link. Examining the link of the double helix, a measure of the entanglement of two curves, and how it changes during detangling (via discontinuities and currents) gives us valuable insight into the process. This allows us to formulate and quantify a cost function and optimal combing strategy (starting near the free ends of the hair and working upwards).

Building off the insights from the minimal model, in Chapter 3 we develop a feedback driven hair combing robot with collaborators at MIT. This robot is able to visually determine the curliness of a head of hair in order to pick an initial combing stroke length and comb starting point. Using force feedback, the robot is also able to adjust its combing procedure based on a chosen pain criteria. The simplicity and flexibility of the robot allows it to adapt and optimize hair combing across a variety of hair types. This work also validates our geometric and topological modeling of hair detangling (Chapter 2) in a more applied setting. We are able to benchmark the performance of our hair combing strategy against both a human and a naive robot and found the optimized robot compared favorably across a wide range of hair types and multiple performance metrics. This work could provide a template for using robots to interact non-destructively with soft, complex materials.

In Chapter 4, we are interested in studying another system that exhibits an interesting relationship between its mechanics and its topology. Taking a common bird's nest as the inspiration for a biologically-inspired material, we explore how geometric relations between the individual constituents (rods) of the randomly packed network related to its material response to stress. Where entangled hairs are a more ordered system due to the interplay between gravity and their relatively soft material stiffness (i.e., long hairs on a head mostly hang in the same direction; see Chapter 2

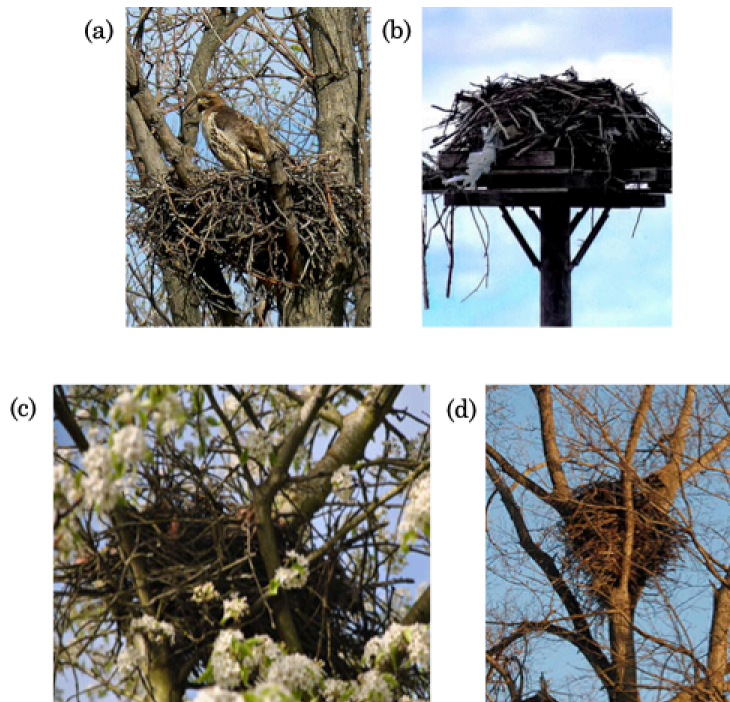


Figure 0.2: Photographs of nests made by large birds. (a) A red-tailed hawk's nest constructed from smaller (2-5 cm diameter) sticks.⁷⁷ (b) An osprey's nest constructed from larger sticks as well as scavenged man-made materials.⁴⁷ (c) A crow's nest showing a looser construction with smaller sticks.⁷⁰ (d) An eagle's nest made from a base of large sticks with softer nesting material on top.⁶¹

Appendix for more details), the rigid rods that make up the entangled networks we study are more naturally disordered and only slightly affected by gravity (see Chapter 4 SI for more details). We examine the mechanical response of these disordered, entangled networks to see what role geometry and topology play in their bulk material properties. This involves connecting the macroscopic story (mechanical stress-strain behavior) with the internal one (geometric and topological). This connection presents potential insights into how to optimize the design and preparation of randomly packed entangled materials.

Our mechanical tests of the rod networks show clear elasto-plastic deformation and aging across the small-strain regime ($\epsilon < 0.15$). We use X-ray computed tomography to reconstruct 3-D images

of the rod networks before and after compression. We are then able to examine internal changes in both coarse-grained (contact number) and fine (volume fraction, orientational order, and entanglement field) geometric and topological properties of the networks in response to strain. We relate the macroscopic compressive stress response to changes in the internal configurations of groups of interacting rods. These geometric and topological tools can be used to characterize many material systems in which physical entanglement is an important characteristic, such as cotton or wool fibers and fiber-reinforced concrete.

Finally, we present some findings for future research directions related to both the hair combing and bird's nests projects. We look at data on combing real curls of horse and human hair and how we can further refine the double helix minimal model for detangling. We also look at ways to account for curlier hair types via applications of braid theory on more complex hair interaction types. Lastly, we examine mechanical data on disentangling rigid rod networks to further our understanding of the physical properties of entangled materials.

A main task on the border between geometria situs and geometria magnitudinus is to count the windings of two closed or infinite lines... m is the number of windings. This value is shared, i.e., it remains the same if the lines are interchanged.

Carl Friedrich Gauss

1

Modeling Elastic Filaments

Communicating science and making complex and interesting subjects accessible and understandable to the general public is a key motivating factor in the work of this dissertation. Using science to help explain seemingly mundane phenomena like hair combing is a way to communicate the diverse uses of science in understanding and unpacking the everyday world. This chapter will focus on making an accessible treatment of the geometric, topological and mechanical properties of thin elastic rods that forms the backbone of the study of any number of interesting topics. For full comprehension, this treatment will assume some background physics knowledge at the level of an advanced undergraduate or early graduate student but with the hope that others can still take away some understanding and insight. This work was completed with the help of L. Mahadevan and Nicholas Charles.

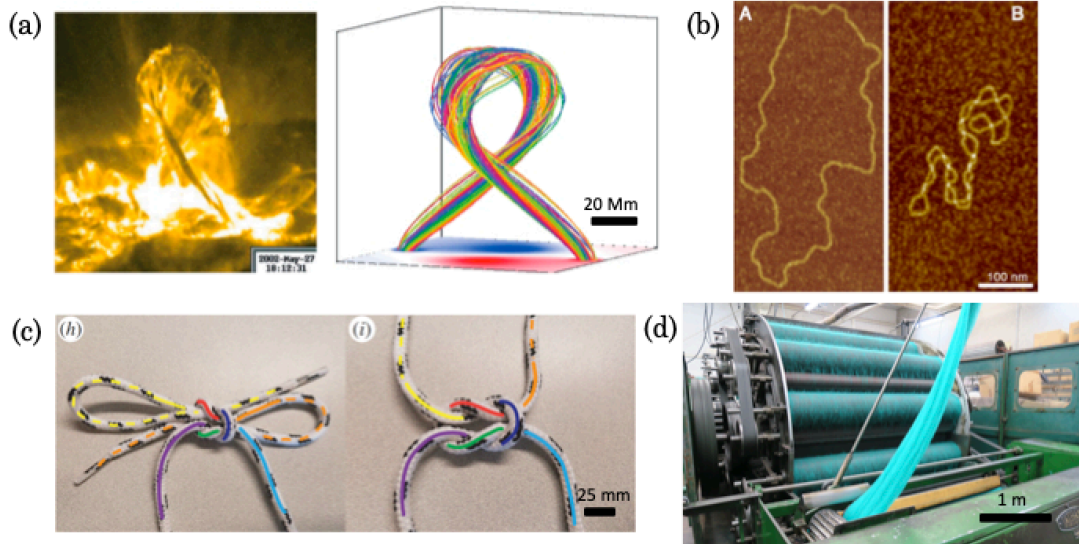


Figure 1.1: Some examples of physical systems at the intersection of elastic rod theory and topology. (a) Image (left) and model (right) of magnetic field lines in solar coronae.⁷⁵ (b) Images of relaxed (left) and supercoiled (right) circular DNA strands.⁸³ (c) Images of the optimally stable shoelace knot.²⁰ (d) Industrial carding machine for straightening tangled wool fibers to be spun into yarns.⁷¹

1.1 INTRODUCTION

Rods, or filaments or strings, and their interactions play a ubiquitous role in physical systems across many orders of magnitude in size, including: DNA winding and unwinding, polymer entanglement in chemistry, vortex line dynamics in fluids, magnetic braids in solar coronae, shoelaces and headphones tangling and detangling, and the carding of fibers in textiles (see Figure 1.1). The unique geometry of thin rods (length $L \gg r$, the radius) simplifies studying their mechanics. Thin rods can also host a number of interesting geometric phenomena (bending, twisting, braiding, knotting, tangling, weaving, etc.).

The rod's high aspect ratio ($\alpha = L/r \gg 1$) allows for a separation of energy scales for different deformation modes. Observe how much easier it is to bend or twist an electronics power cord or phone charging cable than it is to stretch or compress it. Taking this scale separation as a full con-

straint on the motion (no stretching or shearing allowed, though they can be accounted for), we can review a framework for analyzing the deformations of a thin filament.

We will walk through parameterizing the geometry of the rod (how to mathematically describe its shape), accounting for the physical nature of the object (how a rod responds to internal and external forces and torques), and finally introduce the important topological quantity of link. A helical spring will be the case study for the relationships between these geometric, mechanical, and topological descriptions. By the end of this chapter, one example of the relationship between the topology and the mechanics of thin rods will be fully introduced, along with the theoretical tools for analyzing further related problems.

1.2 GEOMETRY, TOPOLOGY, AND MECHANICS OF ELASTIC FILAMENTS

1.2.1 GEOMETRY

We start by assigning a function to trace the shape of the rod (more specifically, its centerline) with respect to a static (also known as lab) reference frame. We will call this parameterization $r(s)$ where s is a variable (parameter) ranging from the start to the end of the rod $s \in (0, L)$. Functions that have a shape that can only be fully described in three Euclidean dimensions are known as space curves. Two nineteenth-century French mathematicians, Joseph Serret and Jean Frenet, independently formulated a coordinate system that could describe the geometric properties of a given space curve. This Frenet-Serret frame (FSF) and the accompanying formulas allow one to parameterize a space curve and carry out simple derivative and vector operations to analyze its geometric features. The Frenet-Serret coordinate system is an orthonormal basis (3D Euclidean space is a common example)

consisting of:

$$\mathbf{T} = \frac{d\mathbf{r}}{ds} \quad (1.1)$$

$$\mathbf{N} = \frac{1}{\kappa} \frac{d\mathbf{T}}{ds} \quad (1.2)$$

$$\mathbf{B} = \mathbf{T} \times \mathbf{N} \quad (1.3)$$

where \mathbf{T} is the tangent vector, \mathbf{N} is the normal vector, \mathbf{B} is the binormal vector and $\kappa = |d\mathbf{T}/ds|$ is the curvature. The FSF attaches to every point along the curve. How it changes from point to point defines the geometry of the space curve through the following relations:

$$\frac{d\mathbf{T}}{ds} = \kappa\mathbf{N} \quad (1.4)$$

$$\frac{d\mathbf{N}}{ds} = -\kappa\mathbf{T} + \tau\mathbf{B} \quad (1.5)$$

$$\frac{d\mathbf{B}}{ds} = -\tau\mathbf{N} \quad (1.6)$$

where $\tau = -\mathbf{N} \cdot d\mathbf{B}/ds$ is the geometric torsion and measures how out of a plane a space curve is. For example, a flat circle in the $r\theta$ -plane parameterized as a pseudo-space curve (because it is only two dimensional) in cylindrical coordinates has a tangent vector $\mathbf{T} = \hat{\theta}$, a normal vector $\mathbf{N} = -\hat{r}$ and a binormal vector $\mathbf{B} = \hat{z}$. Its curvature is $\kappa = 1/R$ where R is the radius of the circle and its torsion is $\tau = 0$ because the curve is contained completely in one plane (flat).

Figure 1.2(a) shows another way to visualize and understand torsion. The tangent and normal vectors define a plane called the osculating plane at all points along the space curve. If this plane ever changes orientation, it is because the curve itself is not confined to a single plane and it therefore has some torsion. Equivalently, changes in the binormal vector are directly proportional to this “out-of-planeness” called torsion, as can be seen in Figure 1.2(b) where the binormal vector of a helical space curve tilts away from a vertical orientation as the helix winds upward from its starting point.

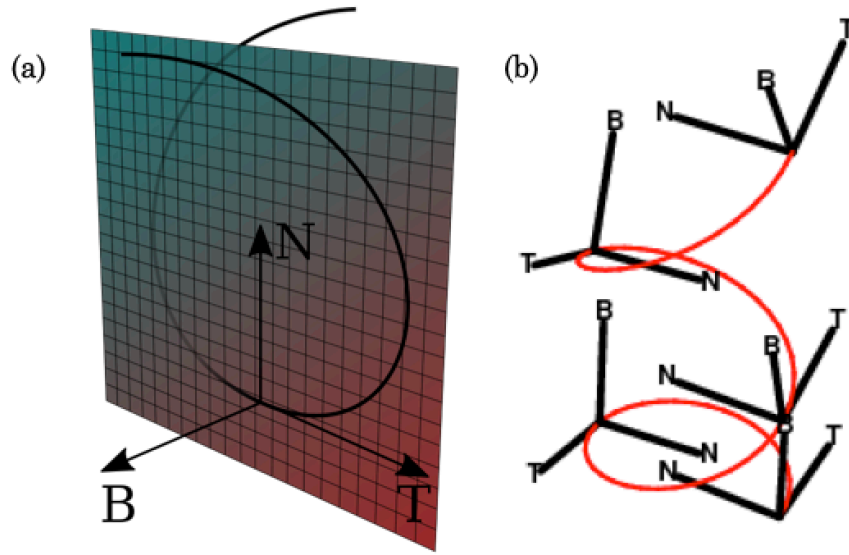


Figure 1.2: The Frenet-Serret frame and torsion. (a) Illustration of the orthonormal basis of the FSF and the osculating plane defined by the tangent and binormal vectors.⁵⁹ (b) The FSF at different points along a helical space curve.⁶⁰

While a curve parameterization, the FSF and its accompanying relations can fully describe the shape of the centerline of a rod, we must also attend to the fact that it is a physical object with an independently defined shape, inertia and material properties. In other words, it takes energy, external forces, and torques to deform a rod that is not fully captured by only using its centerline geometric description. Based on a modernized formulation of work by Kirchoff, Love and Cosserat, we first introduce physical dimensions to the space curve by defining a material body-oriented orthonormal basis of vectors (called directors) $\{\mathbf{d}_1, \mathbf{d}_2, \mathbf{d}_3\}$ where \mathbf{d}_3 points along the centerline tangent (when there is no shear) \mathbf{t} and \mathbf{d}_1 and \mathbf{d}_2 define the normal-binormal plane.²⁶ The dynamics of this new basis differ from the FSF because they describe the orientations of cross-sections of the physical material making up the rod at each point along its arclength s . We can define a rotation matrix $\mathbf{Q} = \{\mathbf{d}_1, \mathbf{d}_2, \mathbf{d}_3\}$ from the directors that can convert generic vectors from the body-centered frame of reference to the lab (or global) frame by $\mathbf{x} = \mathbf{Q}\mathbf{x}'$, where \mathbf{x} and \mathbf{x}' are lab and body-centered

vectors, respectively (see Figure 1.4 for an illustration of the schema).

If the shape of the rod changes over time, we can describe its centerline with a (lab) parameterization $\mathbf{r}(s, t)$ and (local) material frame $\mathbf{Q}(s, t)$. The generalized curvature $\boldsymbol{\kappa} = \{\kappa_1, \kappa_2, \kappa_3\}$ and angular velocity $\boldsymbol{\omega}$ will be defined by changes in the directors over space and time, respectively, such that:

$$\frac{\partial \mathbf{d}_i}{\partial s} = \boldsymbol{\kappa} \times \mathbf{d}_i \quad (1.7)$$

$$\frac{\partial \mathbf{d}_i}{\partial t} = \boldsymbol{\omega} \times \mathbf{d}_i. \quad (1.8)$$

The curvature $\boldsymbol{\kappa}$ and angular velocity $\boldsymbol{\omega}$ can be equivalently defined by

$$\boldsymbol{\kappa} = \text{vec}[(\partial \mathbf{Q} / \partial s)^T \mathbf{Q}] \quad (1.9)$$

$$\boldsymbol{\omega} = \text{vec}[(\partial \mathbf{Q} / \partial t)^T \mathbf{Q}] \quad (1.10)$$

where $\text{vec}[\mathbf{M}]$ is the 3-vector associated with the skew symmetric matrix \mathbf{M} (a 3×3 skew symmetric matrix only has three unique off-diagonal elements). We can then add a full kinematic description of the rod to our geometric one by using the equations

$$\text{Linear velocity: } \frac{\partial \mathbf{r}}{\partial t} = \mathbf{v} \quad (1.11)$$

$$\text{Angular velocity: } \frac{\partial \mathbf{d}_i}{\partial t} = (\mathbf{Q}^T \boldsymbol{\omega}) \times \mathbf{d}_i \quad (1.12)$$

$$+ \text{Initial and Boundary Conditions} \quad (1.13)$$

where the linear and angular velocities are written in the lab and material frames, respectively.

Because the rod may have a non-uniform cross-sectional shape, we must define two curvatures κ_1 and κ_2 associated with bending the rod about the two principal cross-sectional axes defined by \mathbf{d}_1

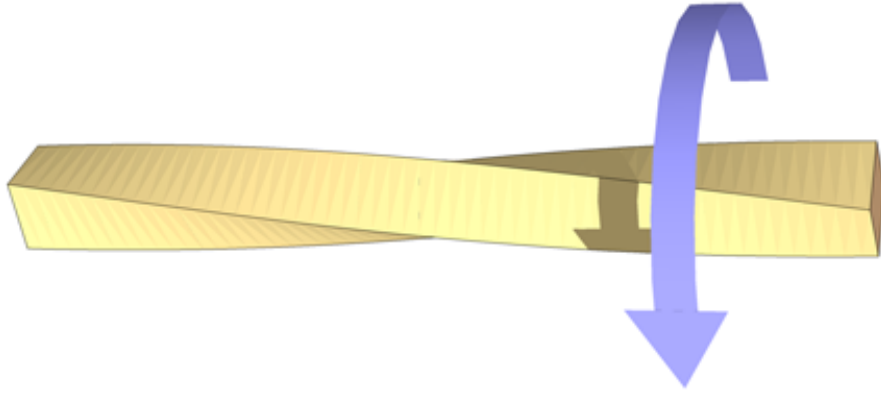


Figure 1.3: An initially straight elastic bar with a square cross section, fixed at one end, is loaded with an external torque at the free end. The bar gains an intrinsic twist at its newly deformed equilibrium.¹

and \mathbf{d}_2 . Another type of curvature, κ_3 , and deformation is associated with twisting the rod about the tangentially-oriented vector \mathbf{d}_3 . This curvature is closely related to but not necessarily equal to the geometric torsion .

We can understand this fuller description of torsion by considering a straight segment of a rigid bar which, by definition, would have zero geometric torsion. The bar is fixed at one end and we grip the bar firmly at the free end and twist our wrist to apply an external torque. The rod will remain straight but we will still exert energy and feel resistance as we twist (see Figure 1.3). This is because cross-sections of the material are being stressed and there is a resultant internal torque and associated energy. In analogy to the FSF, we can think of the osculating plane formed by the directors changing orientation or one of the other directors revolving around \mathbf{d}_3 like the binormal did around the tangent. This type of torsion can be referred to as intrinsic twist.

A full treatment, like the one first developed by the Cosserat brothers, would also include stretching and shearing deformations of the rod.¹⁸ In these deformation modes, the material vector \mathbf{d}_3 can change length and orientation relative to the centerline tangent vector. External loads can distort the material frame by changing the length of the rod (stretching) and rotating the \mathbf{d}_3 director away from being parallel to the tangent vector (shearing). See Figure 1.4 for a fuller schematic picture. We

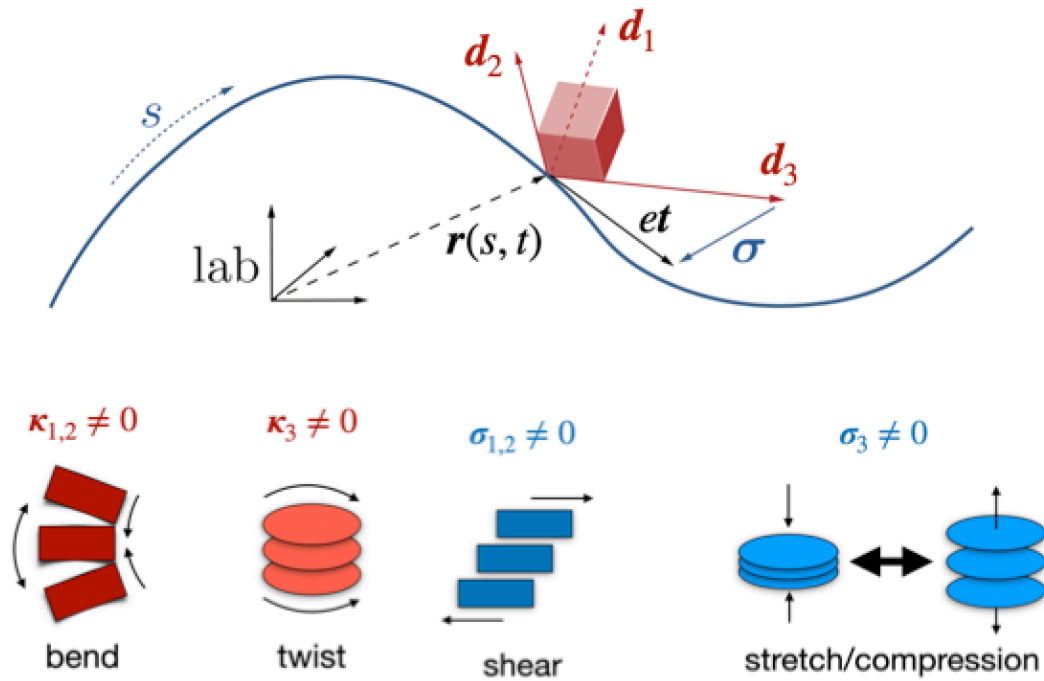


Figure 1.4: Illustration of the Cosserat theory for elastic filaments showing the material-oriented director frame as well as the deformation modes and their associated geometric quantities.

will assume that the separation of energy scales between bending and twisting, and stretching and shearing, is sufficiently large so that we can neglect the latter two. This assumption is especially valid for high aspect ratio rods, as will become clear when we do a fuller treatment of a helical spring.

1.2.2 TOPOLOGY

Analyzing the geometry of an object without respect to its specific size or shape is the key use of topology with regards to thin elastic rods. It can be hard to imagine that we can make simple predictions about the overall shape of a rod after deformations but, under certain conditions—like the rod being a closed loop or held fixed in some way at both ends—we can do exactly that. This understanding relies upon the Calugareanu-Fuller-White (CFW) Theorem, which articulates the funda-

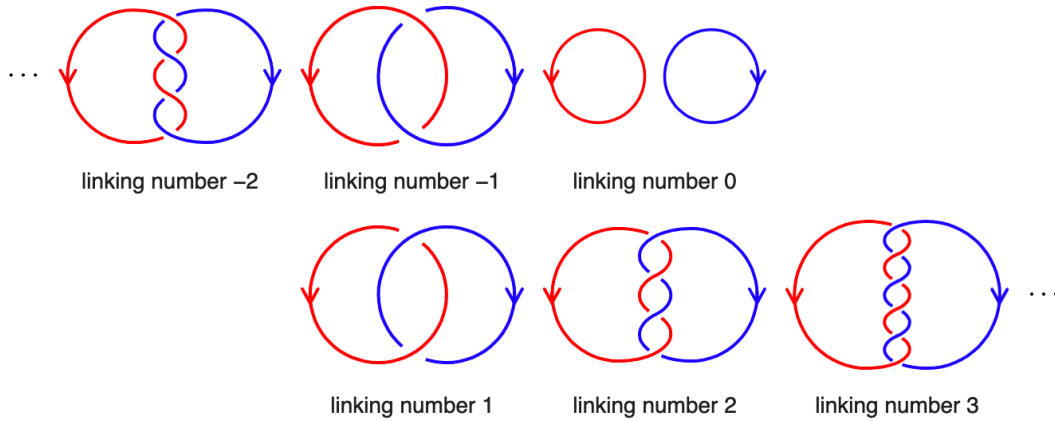


Figure 1.5: The linking number of two closed space curves is a well-defined topological invariant that measures how connected they are to each other.³⁷

mental connection between three relevant geometric and topological attributes of rods, and more specifically helical springs. These attributes—Twist, Writhe and Link—give important information about the configuration of a rod, and their interrelation can be a powerful analytical tool.

While each quantity is relatively true to its name, Link is the easiest to describe and conceptualize of the three. Link was first fully conceived by Gauss in the nineteenth century.²⁵ While studying the line integral of a magnetic field along a closed loop Γ' intersecting a current carrying wire in another closed loop Γ (now recognizable as an example of Ampere's law), Gauss found an interesting result:

$$n = \frac{1}{4\pi} \int_{\Gamma'} \mathbf{B}(x') \cdot d\mathbf{x}' \quad (1.14)$$

where $\mathbf{B}(x')$ is the field of a wire with current equal to 1. Gauss showed that the integer n is dependent only on how many times the closed loop Γ' passes through the current carrying loop Γ . This makes Gauss's integral a topological quantity that is invariant to the size or shape of either curve as long as they do not cross through each other. This integer is called Link and it is a measure of how topologically entangled (or inseparable) two closed curves are with each other (see Figure 1.5).

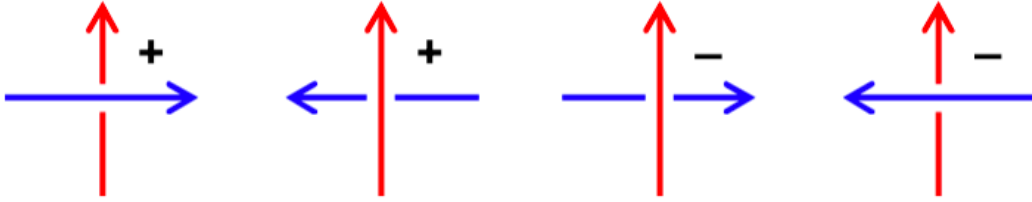


Figure 1.6: The linking number can be calculated by adding the number of signed crossings of two closed curves according to the rules shown above. It can also be calculated using Gauss's linking integral (equation 1.15).³⁶

Given two closed curves \mathbf{x}_1 and \mathbf{x}_2 , the Link can be calculated with the Gauss linking integral:

$$Lk = \frac{1}{4\pi} \oint_{\mathbf{x}_1} \oint_{\mathbf{x}_2} \frac{\mathbf{r}_1 - \mathbf{r}_2}{|\mathbf{r}_1 - \mathbf{r}_2|^3} \cdot (d\mathbf{r}_1 \times \mathbf{r}_2). \quad (1.15)$$

Link Lk can equivalently be calculated by adding the number of signed crossings of two closed curves and dividing by two, as in Figure 1.6.

To get a better understanding of Twist and Writhe, we will introduce the mathematical concept of a ribbon. A ribbon is defined by space curve (like the centerline of a rod) together with a unit vector perpendicular to the space curve at every point (like the normal or binormal vectors). The dynamics of this ribbon as it varies along the arclength of a space curve or rod will define Twist and Writhe.

Twist is defined as the total integral of the torsion over the arclength s ,

$$Tw = \int_0^L \tau(s) ds. \quad (1.16)$$

For physical rods, the torsion includes the geometric part and the intrinsic twist. In this way, Twist quantifies both how far out of a single plane the rod centerline deviates, as well as how much intrinsic twist is present in the rod (think of the ribbon vector as one of the non-tangential material directors). See Figure 1.7 for an example of a planar rod with non-zero Twist.

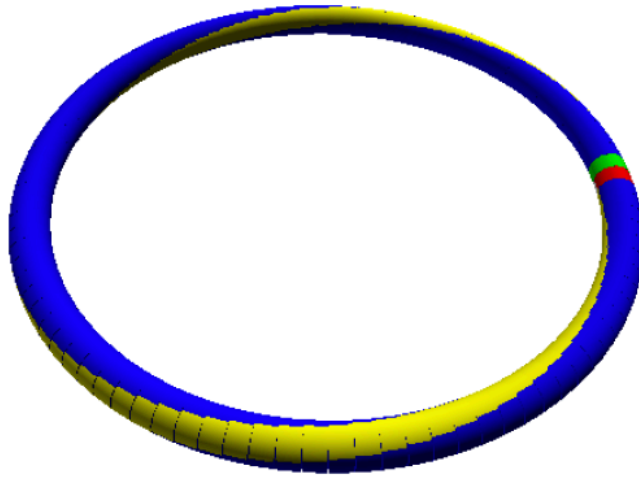


Figure 1.7: Simulation of a circular elastic rod with zero geometric torsion but non-zero intrinsic twist.⁴⁶

Writhe is a measure of how coiled a curve is. Consider the centerlines of helical curves of different radii and pitches. Looking along the vertical axis, the centerline of a helix with a large radius and small pitch crosses over itself extensively over its arclength, while the helix itself has a small height. On the other hand, a helix with the same arclength but a smaller radius and larger pitch crosses over itself with much less overlap, while being much taller in height. Colloquially, the larger radius helix takes up more three-dimensional space while the smaller radius helix is almost one-dimensional (see Figure 1.9(b)). Writhe is a measure of this “three-dimensionality” and the wider, shorter helix has a larger writhing number than the skinny, stretched one. It’s often difficult to calculate a standalone value for Writhe, so we’ll study it further in relation to its two previously mentioned counterparts.

In the mid-twentieth century, Calugareanu¹², White⁸¹ and Fuller²³ formulated the attributes of Link (Lk), Twist (Tw) and Writhe (Wr) and developed an equation on the relationship between them:

$$Lk = Tw + Wr, \tag{1.17}$$

now commonly referred to as the CFW theorem. We can derive this theorem by applying Gauss's linking integral to two curves in a ribbon configuration, where $\mathbf{r}_1(t) = \mathbf{x}(t)$ and $\mathbf{r}_2(t) = \mathbf{x}(t) + \varepsilon \mathbf{u}(t)$. The vector $\mathbf{u}(t)$ is perpendicular to $\mathbf{x}(t)$ at all points and the small parameter ε is varied to zero so that the linking integral can be split in two pieces. One piece is the Writhe and is a double integral over the same space curve:

$$Wr = \frac{1}{4\pi} \oint_{\mathbf{x}} \oint_{\mathbf{x}} \frac{\mathbf{r}_1 - \mathbf{r}_2}{|\mathbf{r}_1 - \mathbf{r}_2|^3} \cdot (d\mathbf{r}_1 \times \mathbf{r}_2) \quad (1.18)$$

where \mathbf{r}_1 and \mathbf{r}_2 are separate points on a single curve \mathbf{x} . The other piece is the Twist and is the same as the earlier definition.

We can consider these three quantities (Lk , Tw , Wr) in the context of a thin elastic rod to see how the CFW theorem can be used to predict configuration dynamics. Let the curve \mathbf{r}_1 be the centerline of the rod and the second curve \mathbf{r}_2 be one of the normal-binormal plane directors to form a ribbon. For a closed rod (or one fixed at both ends), when the centerline changes shape, the Writhe must change value as well. Through the CFW theorem, we know the total Link of the rod is fixed, so the Twist must also change accordingly. In this way, the centerline of the rod and its material-oriented frame (the directors) are not independent of each other. See Figure 1.8 for a clear example of how the CFW theorem converts an initially straight but twisted elastic ribbon into a coiled, writhed shape.

That the CFW theorem only applies to closed or fixed-boundary curves would seem to limit its general usefulness. However, we can relax these conditions somewhat by considering how Link changes if, say, only one end of the rod is fixed and the other is allowed to move freely. In this system, Link could enter or leave according to a Link current j that obeys the local conservation law:

$$\frac{\partial j}{\partial s} = \frac{\partial \lambda}{\partial t} + \frac{\partial \mathbf{t}}{\partial t} \cdot \left(\frac{\partial \mathbf{t}}{\partial s} \times \mathbf{t} \right) \quad (1.19)$$

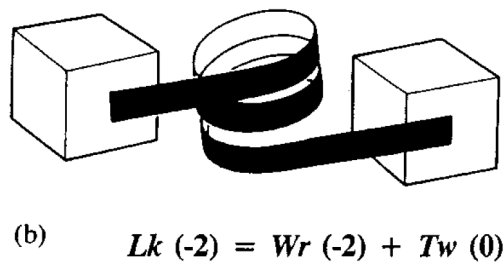
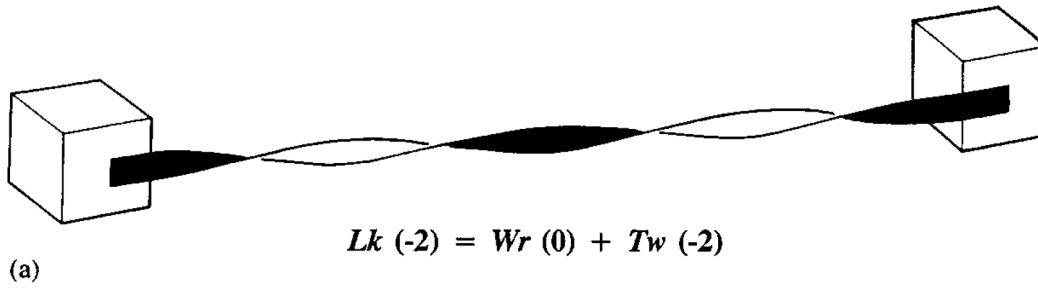


Figure 1.8: An elastic ribbon is fixed at both ends to keep the linking number constant. (a) With the ends far apart, the ribbon is in a twisted state. (b) When the ends are brought together, the Twist is converted to two loops (Writhe) and the linking number remains invariant.⁷⁶

where λ is Twist density and \mathbf{t} is the FSF tangent vector. This equation implies two principal deformation modes in which Link can move into, out of or through a system: crankshaft-like whirling motions of the centerline or twirling motions of the torsional modes.⁴⁰

1.2.3 MECHANICS

We will now introduce physical descriptors of deformations called bending and twisting that directly affect the dynamics of the directors. We also assume that the rod is perfectly elastic so that deformations and their corresponding forces and torques are linearly related. To further study the effects of external loads (forces and torques) on thin elastic rods, we will introduce the relevant con-

stitutive relations and dynamic equations.

In the elastic regime, external torques can generate bending and twisting deformations that are related to internal torques through geometry and continuity as

$$\boldsymbol{\tau} = \mathbf{B}(\boldsymbol{\kappa} - \boldsymbol{\kappa}_0) \quad (1.20)$$

where the vector $\boldsymbol{\tau}$ is the internal torque, the matrix \mathbf{B} is the bending stiffness and the vector $\boldsymbol{\kappa} = \{\boldsymbol{\kappa}_1, \boldsymbol{\kappa}_2, \boldsymbol{\kappa}_3\}$ is the curvature associated with bending about the same-indexed directors. The curvature $\boldsymbol{\kappa}_0$ accounts for objects with unstressed initial shapes other than a straight line (like a helical spring). The bending stiffness matrix is defined as

$$\mathbf{B} = \begin{pmatrix} EI_1 & & \\ & EI_2 & \\ & & GI_3 \end{pmatrix} \quad (1.21)$$

where the diagonal terms define the bending stiffness about each director, with the tangential director \mathbf{d}_3 related to the twisting stiffness. E and G are the Young's modulus and shear modulus, respectively, and I_i is the second area moment of inertia about each director.

Similarly, external forces can generate straining and shearing deformations that are related to internal forces by

$$\mathbf{n} = \mathbf{S}(\boldsymbol{\sigma} - \boldsymbol{\sigma}_0) \quad (1.22)$$

where the vector \mathbf{n} is the internal force, the matrix \mathbf{S} is the shearing stiffness and the vector $\boldsymbol{\sigma}$ is the shear and strain associated with each director. The vector $\boldsymbol{\sigma}_0$ accounts for any initial unstressed shear

or strain in the rod. The shearing stiffness matrix \mathbf{S} is defined as

$$\mathbf{S} = \begin{pmatrix} \alpha_c GA & & \\ & \alpha_c GA & \\ & & EA \end{pmatrix} \quad (1.23)$$

where A is the cross sectional area and the constant α_c is $4/3$ for a circular cross section.

Finally, we can add the dynamical governing equations for changes in linear and angular momentum to the kinematic equations (1.11 and 1.12) we introduced earlier.

$$\text{Linear momentum: } \frac{\partial(\rho A \mathbf{v})}{\partial t} = \frac{\partial \mathbf{n}}{\partial s} + \mathbf{f} \quad (1.24)$$

$$\text{Angular momentum: } \frac{\partial(\rho \mathbf{I} \boldsymbol{\omega})}{\partial t} = \frac{\partial \boldsymbol{\tau}}{\partial s} + \frac{\partial \mathbf{r}}{\partial s} \times \mathbf{n} + \mathbf{c} \quad (1.25)$$

where ρ is the mass density, \mathbf{I} is the second area moment matrix, \mathbf{n} is the external force line density, and \mathbf{c} is the external torque line density. The second area moment is a diagonal matrix whose values quantify how the area of a cross-section perpendicular to the tangent director is distributed relative to each director. Equation 1.24 relates the internal forces (proportional to the shearing stiffness and shear/strain) and the external forces to changes in the linear momentum of the rod. Equation 1.25 relates the internal torques (proportional to the bending stiffness and curvatures), external torques, and external forces not acting along the centerline tangent to changes in angular momentum of the rod. For quasi-static or equilibrium analysis, the left-hand sides of all governing equations (1.11, 1.12, 1.24, 1.25) will be zero and external forces and torques will be balanced by internal changes in curvature $\boldsymbol{\kappa}$ and shear/strain $\boldsymbol{\sigma}$.

Moving forward, we will ignore external and internal forces associated with straining and shearing. They are much more energetically costly than bending or twisting for a high aspect ratio object like a helical spring formed from a thin rod. For a circular cross-section rod, each component of the

bending stiffness is scaled by a factor of r^2 compared to the corresponding shearing stiffness component. When $r \ll L$, then the total energy (integrated over the length of the rod) to bend or twist the rod is significantly less than the energy to shear or strain it.

1.3 ANALYZING A HELICAL SPRING

Now we will bring the geometric, topological, and mechanical framework we've walked through to bear on the system of a thin elastic rod initially shaped into a helix (a helical spring). A helix with pitch p and radius r can be defined by a single pitch angle $\alpha = \arctan(p/2\pi r)$, which is an angle measuring the slope of a single turn of the helix (p is the vertical displacement of the turn and $2\pi r$ is the horizontal). We parameterize the centerline of the helix in cylindrical coordinates as:

$$\mathbf{x} = r\hat{r} + r\alpha\hat{z}. \quad (1.26)$$

Using the FSF and Cosserat framework for an non-sheared and non-strained rod, we get values for the geometric torsion and curvature in the unstressed state of:

$$\tau_0 = \frac{\alpha}{r(1 + \alpha^2)} \quad (1.27)$$

$$\kappa_0 = \frac{1}{r(1 + \alpha^2)}. \quad (1.28)$$

Helices are unique among space curves for having constant and non-zero torsion and curvature. The total arclength of the helix is $S = 2\pi r N \sqrt{1 + \alpha^2}$ where N is the number of turns of the helix.

We can now define our two curves to analyse Link, Twist and Writhe. We will create a ribbon using the centerline of the helix as the base curve and the FSF normal vector as the other curve. As previously discussed, the geometric torsion measures the rate at which the normal vector rotates around the tangent vector. The Twist is the integral of the geometric torsion over the length of the

curve (equation 1.16) plus any intrinsic twist. Parameterizing the arclength for a helix with N turns, we get:

$$\begin{aligned} Tw &= \frac{N}{2\pi} \int_0^{2\pi} \frac{\alpha}{r(1+\alpha^2)} r\sqrt{1+\alpha^2} d\phi \\ &= N \frac{\alpha}{1+\alpha^2}. \end{aligned} \quad (1.29)$$

This gives us the total geometric twist and we will assume that there is no intrinsic twist in the unstressed state of the physical helix.

To calculate Link, we can count the oriented crossings of the curve defined by the helix centerline and the vertical central axis. Though the helix is not technically a closed curve, for our analysis we can assume it is fixed at both ends (no twirling or whirling) so that no Link can leave the system (the Link current from equation 1.19 is zero at the boundaries). Alternatively, we could imagine attaching simple segments that loop around so that two the curves are individually closed and linked together. The centerline will rotate once around the vertical axis for every turn of the helix. Viewed from a particular polar angle θ , like $\pi/4$, the centerline will cross over the vertical axis twice. From the counting method layed out in Figure 1.5, the total Link of the helix will be equal to the number of turns N . Using the CFW theorem, we can then calculate the Writhe of the helix to be

$$Wr = N \left(1 - \frac{\alpha}{1+\alpha^2} \right). \quad (1.30)$$

We can check our intuition for these results by thinking about how Link, Twist and Writhe will interplay as we vary the pitch parameter α of a closed helix with a fixed arclength (link current $j = 0$ and strain $\sigma_3 = 0$). Consequently, the pitch and radius are not independent geometric parameters. For small α , the helix will have a larger radius and smaller pitch. For larger α , the opposite will be true. However, both helices have the same linking number and thus there must be some trade-off

between Twist and Writhe. We can see this clearly in Figure 1.9, where the wider, shorter helix is more writhed and the thinner, taller helix is more twisted. This matches our earlier casual understanding of Writhe as a measure of the three-dimensionality of a curve centerline: the higher Writhe helix expands in all directions more than the almost one-dimensional lower Writhe helix.

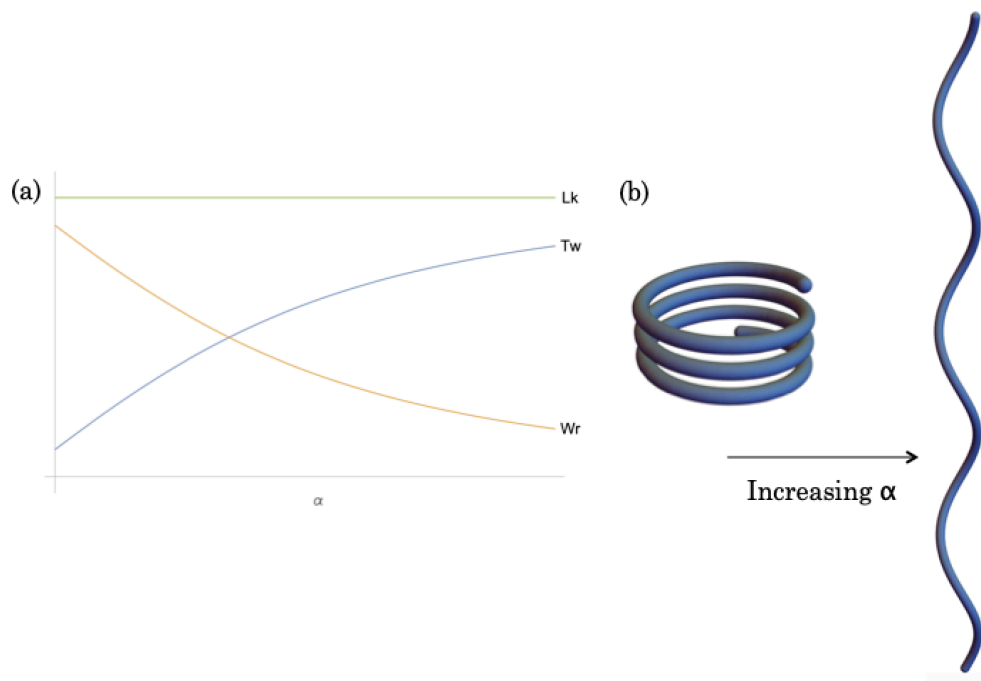


Figure 1.9: The relationship between Link (Lk), Twist (Tw) and Writhe (Wr) for a single helix. (a) Plot of Lk , Tw , and Wr as a function of helix pitch angle $\alpha = \arctan(p/2\pi r)$. The CFW theorem and the changing geometry of the helix (with a fixed arclength) determine their relations. All values have been normalized by the total Link. (b) Increasing the pitch parameter while maintaining a fixed linking number (or number of turns N) shifts the helix from a highly coiled state (left) where the Writhe dominates to a highly twisted state (right) where the Twist dominates.

Finally, we can connect this topological viewpoint to help understand and predict the deformation of a helical spring under external loads. We know from our earlier mechanical framework (assuming no stretching or shearing forces) that, at equilibrium, any external forces or torques applied to the ends of the helix will be balanced by internal changes in shape through bending and twisting modes (equations 1.20 and 1.25). In the elastic regime, this will result in deformation to a new helix

geometry with the same arclength S and new radius $r + \delta r$ and new pitch angle $\alpha + \delta\alpha$. Using work done by A.E.H. Love⁴⁴, we get the following equations of mechanical equilibrium for a helix with an applied force F and applied torque τ

$$F = \frac{1}{Sr^2} [\delta L (C \cos^2 \alpha + B \sin^2 \alpha) + 2\pi r \delta N (C - B) \sin \alpha \cos \alpha] \quad (1.31)$$

$$\tau = \frac{1}{Sr} [\delta L (C - B) \sin \alpha \cos \alpha + 2\pi r \delta N (C \sin^2 \alpha + B \cos^2 \alpha)] \quad (1.32)$$

where δN is the change in the number of turns, δL is the change in the axial length of the helix, B is the bending stiffness and C is the twisting stiffness.

We will consider the case where we apply an axial external force to stretch the helix to a new axial length $L + \delta L$ with $\tau = 0$. Solving for the changes in the number of turns and axial length, we get

$$\delta L = Sr^2 \left(\frac{\sin^2 \alpha}{B} + \frac{\cos^2 \alpha}{C} \right) F \quad (1.33)$$

$$\delta N = \frac{Sr}{2\pi} \sin \alpha \cos \alpha \left(\frac{1}{C} - \frac{1}{B} \right) F. \quad (1.34)$$

If we enforce the constant Link constraint ($\delta N = 0$) when applying the axial force (the ends of the helix are not allowed to whirl or twirl, only move farther apart), a deformed helix must exchange some Writhe for Twist. Through the unique geometry of the helix, this will correspond to a decreased radius and an increased pitch (see Figure 1.10). For a perfectly elastic helical spring with constant link, we could stretch it until its centerline is straight and all Writhe has been converted to Twist (in the form of intrinsic twist).

1.4 CONCLUSION

Combining Kirchoff's rod theory for inextensible and un-shearable filaments with an understanding of Link topology can help our understanding of a wide range of problems across length and time

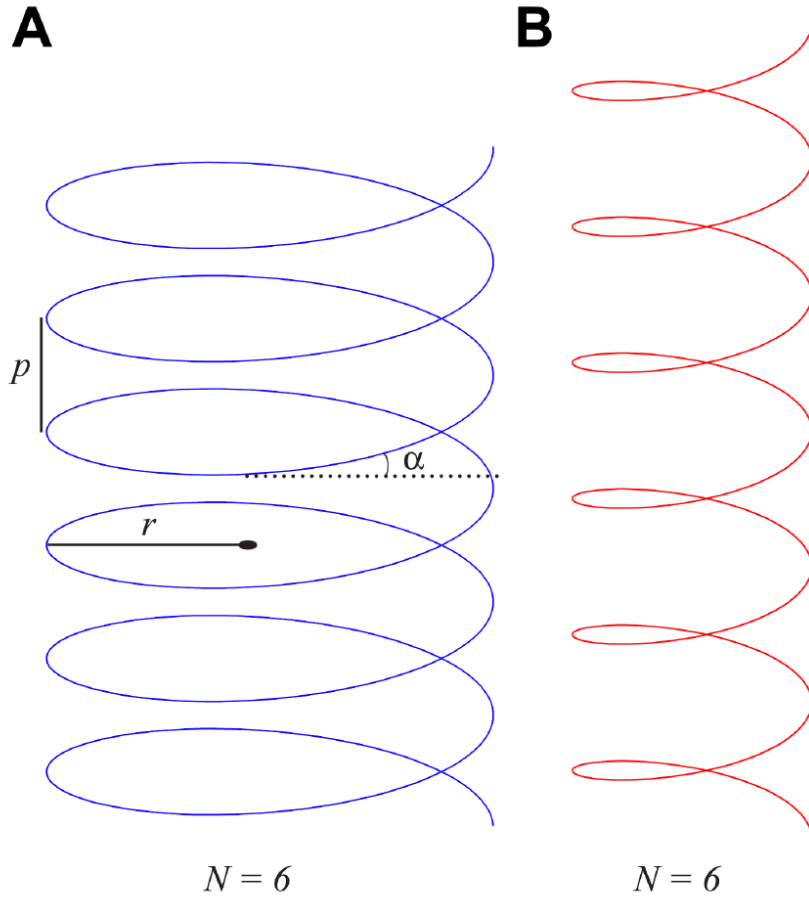


Figure 1.10: (a) A helix with pitch p , radius r , pitch parameter α , axial length L , and number of turns N . (b) The same helix deformed by stretching it to an axial length $L + \delta L$ while keeping the turn number N constant. In other words, there is no link current j (equation 1.19) flowing out either end of the helix.⁴⁶

scales. This framework can help us understand and study coiling and overwinding in cucumber tendrils²⁸, the formation of solenoids and plectonemes in artificial muscle fibers¹⁴ and the detangling process in hair combing (see Chapter 2 of this dissertation). While fully analyzing elastic rod dynamics can have some unavoidable complications (non-linearity/inelastic response, interactions between multiple rods), understanding the underlying topology of the system can still help us make testable predictions and validate results.

The smallest hair casts a shadow.

Sir Francis Bacon

2

Combing a double helix

Now that we've established the framework for combining geometry, mechanics and topology to study thin elastic rods, we can move on to applications. In 2021, Nicholas Charles, L. Mahadevan and I wrote a paper, with a preprint published on ArXiv, on detangling hair with a comb as a problem at the interaction of geometry, mechanics, and topology. This paper is included as the first application of the theory from Chapter 1 because it represents a logical extension of elastic rod topological mechanics: studying the interactions of two topologically entwined elastic filaments as a minimal model for hair combing. The full paper is included here, with minor edits to the format. The references are likewise altered from the original publications to fit this dissertation.

2.1 ABSTRACT

Combing hair involves brushing away the topological tangles in a collective curl. Using a combination of experiment and computation, we study this problem that naturally links topology, geometry and mechanics. Observations show that the dominant interactions in hair are those of a two-body nature, corresponding to a braided homochiral double helix. Using this minimal model, we study the detangling of an elastic double helix via a single stiff tine that moves along it, leaving two untangled filaments in its wake. Our results quantify how the forces of detangling correlate with the link density, a topological quantity, that propagates ahead of the tine and flows out the free end as a link current. This in turn provides a measure of the maximum characteristic length of a single combing stroke in the many-body problem on a head of hair, producing an optimal combing strategy that balances trade-offs between comfort, efficiency and speed of combing in hair of various geometries.

2.2 INTRODUCTION

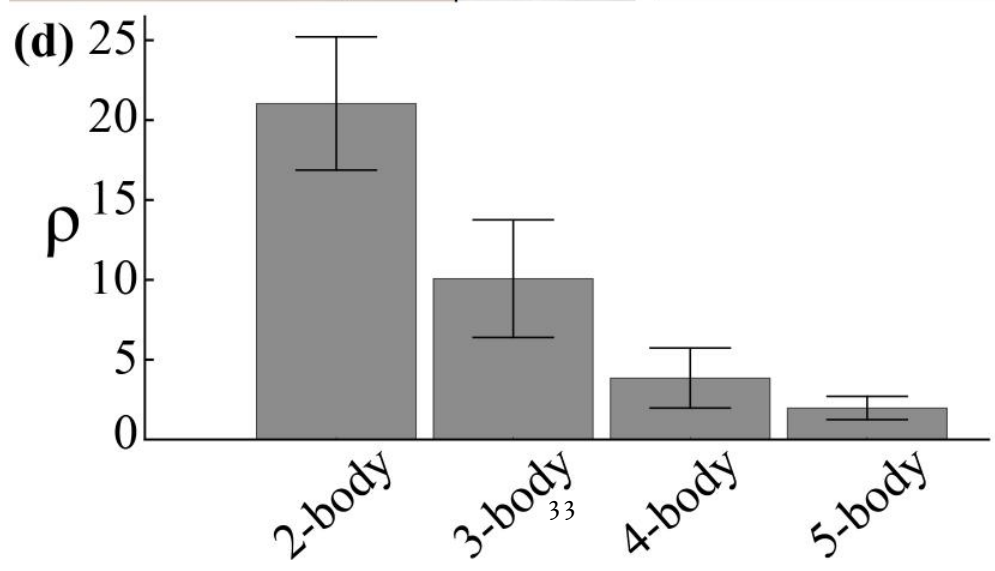
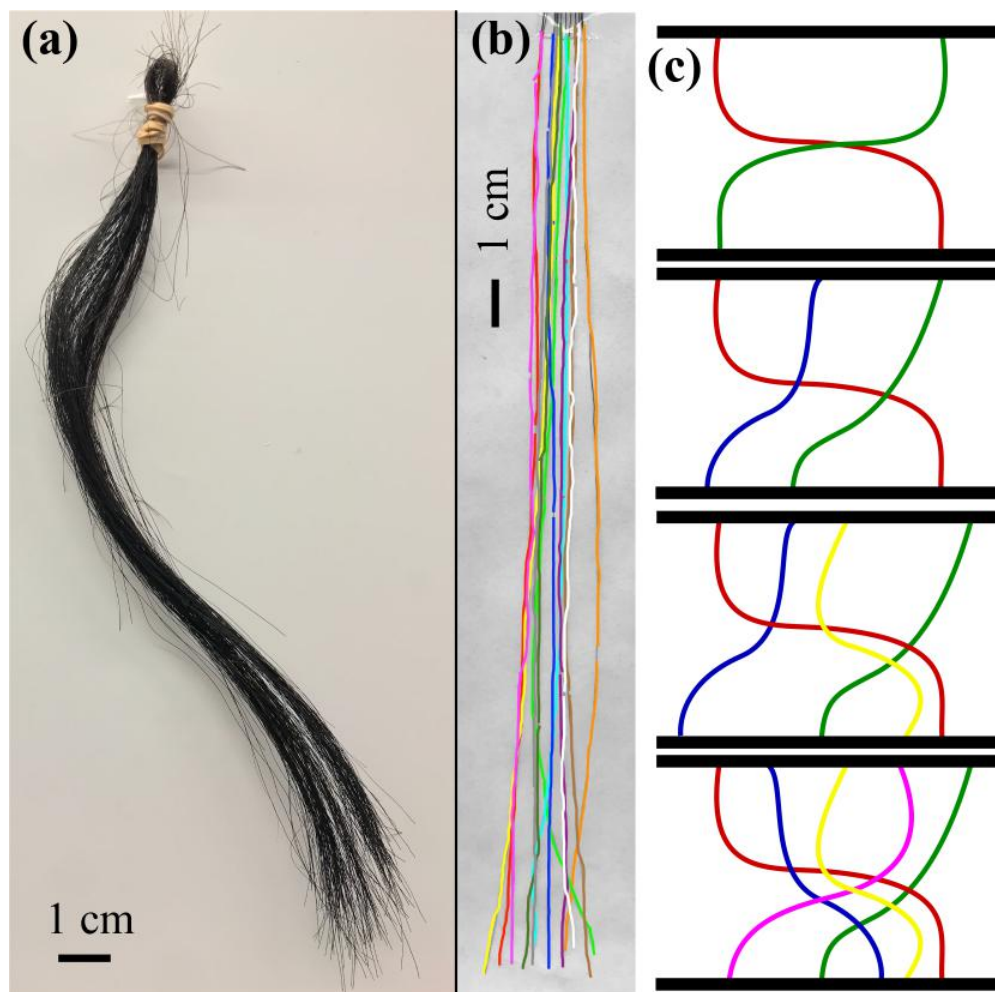
Long-haired people are familiar with a well-known strategy for combing their hair: start combing away the tangles close to the free hair ends, and work steadily upward towards the scalp. This allows for the untangling of a collective *curl*—a bundle of interacting filaments, clamped at one end and characterized by similar local geometry and length—to proceed more efficiently from the free end, minimizing pain but at the expense of time. But how does a comb work its way through a curl? This quotidian problem which lies at the intersection of mechanics, geometry and topology has many cousins—the carding of textiles and felts^{32,42}, and the spontaneous tangling and detangling of polymers in a flow^{72,5}, of flux lines in superconductors⁴⁸ and of magnetic fields in solar coronae⁸. In the context of hair, there has been a recent resurgence of interest in characterizing the effective properties of fiber assemblies and packings^{33,51,52,38,41,79,31,13}, inspired by simple curiosity, technological applications to fields such as robotics, and even the need to model hair animation^{78,7}. Much of these studies neglect individual hair-hair interactions, and little is known about the dynamics of detangling in complex packings of fibers and hair from a mechanical or topological point of view. In the scant literature that addresses individual hair-hair contact⁵³ and fiber assembly topology^{53,57}, the pervasive problem of global detangling an open curl by an external tine is not considered from a mechanical or topological viewpoint.

2.3 MINIMAL MODEL OF HAIR CURL

The complexity of the combing problem is potentially associated with the many-body nature of interacting filaments (hairs) and their potential for long-range interactions—that is, the potential for local hair interactions in one location along the curl’s arclength to affect the local hair interactions at another location along the curl, far away in terms of curl arclength. As an example, observations of a curl of horse hairs (Figure 2.1(a)) show that they are mostly straight, enhanced by gravity that helps

Figure 2.1 (following page): Tangles in hair. **(a)** Curl of horse hair. **(b)** Colored curl of 12 human hairs, clamped at one end. **(c)** Schematics of N-body interactions ($N = 2-5$). **(d)** Histogram of N-body interactions for a sample similar to (b) with ρ = number of interactions per unit length (in meters). We segment the curl into 20 sections, count the interaction types within each section, as defined in (c), and average them across different curls (horse and human).

Figure 2.1: (continued)



straighten the hairs; only near the free end can the hairs adopt their natural curvature (see appendix for further discussion). To quantify the nature of these interactions, we digitally color each strand to track their interactions with their neighbors in a curl (Figure 2.1(b)), segment the curl into sections, and then count and characterize the internal interactions of each strand using the interaction definitions in Figure 2.1(c). Viewing the curl side-on (or equivalently, projecting the curl onto a plane parallel to the curl axis), we define an interaction to be where strands cross each other. Counting true interactions would require accounting for the sign of the crossing—i.e. if a hair moves over or under another—so our metric acts as an upper bound on the true number of interactions. In Figure 2.1(d), we plot the number of N-body interactions, and see that pair-wise interactions form a plurality of the tangle types in our analyzed curls (see appendix for further investigation). While this plurality would likely be less pronounced for curlier hair, we restrict ourselves to relatively straight curls—i.e., an individual hair’s radius of curvature is on the same order as its length.

2.4 EXPERIMENTAL OBSERVATIONS OF COMBING

Given the dominance of two-body interactions, we first consider a minimal model of the comb-curl system: two homochiral entwined helices clamped at the top end and hanging freely at the bottom. Although the curls we consider are relatively straight, we expect our double helix model to effectively capture the most important interactions in the tangled parts of the curl. The filaments are made of nylon (heated to force them to conform to 3-D printed helically grooved cylinders, and then cooled). This assembly is then pierced at the midpoint of the double helix centerline by a single stiff rod (the comb), producing an initial structure with links to both sides of the newly inserted tine. The tine moves downward quasi-statically to detangle the downstream region of the curl. We use an Instron 5566 material testing machine to measure the force extension curves of the rod-helix combing system.

In Figure 2.2(a) we show the response of the helix that can be associated with either kinking or winding. While winding is inevitably required for helix untangling, we frequently observe *kinking*, resulting from sliding and shear between the free-end sides of the two helices, leading to a characteristic bent state (Fig 2.2(a,b)). This spontaneous relative sliding of filaments along their axial direction appears topologically unnecessary for helix detangling, but may indicate a subtle instability of the curl during combing. Over- and under-winding describes the stretching out of the helices behind the tine and a concomitant compression of the free end. As the tine moves through and along the double helix, the force-extension profile of the process evolves. We examine this in terms of the helix radius R , filament radius r , tine radius t , and helix pitch P (Figure 2.2b), expressed in terms of the dimensionless ratios $\pi_1 = P/r$, $\pi_2 = R/r$ and $\pi_3 = t/r$, deferring variation of π_3 to the supporting information since t appeared to have little impact on the nature of helix unwinding. Note that we consider here only helices of constant geometry, acknowledging that, in reality, a curl's pitch and radius of curvature may vary over arclength. It is possible that one could infer the mechanical and topological response of a non-uniform curl to combing by using the results obtained here to interpolate between regions of different geometry. However, we leave the study of more complex curls to future work, making our present goal establishing a connection between the topology and mechanics of uniform curls of hair. Note also that, since combing experiments and simulations occur quasi-statically, precise rate of combing does not affect results. However, future studies could also consider the dynamics and effect of combing rate on hair detangling.

In Figure 2.2(d,e) we show the scaled force on the tine $f = Fl_0^2/B$ as a function of the scaled tine displacement x through the double helix. Smaller pitch and radius helices (more tightly wound) require larger forces required to detangle. There is generally an initial rise in the force extension curve before a leveling off, corresponding to overwinding of the helix in front of the tine. After the initial rise, the force peaks when the tine jams, falling once the tine breaks through, although there is no rise in the force or tine jamming for loose helices, i.e. $P/r > c \approx 20$. We overlay the

force required to equivalently stretch a single helix for comparison (initial angle α and helix radius R extended to final radius angle α_1 and helix radius R_1 ⁴⁵; see appendix for details). In contrast with the force-extension curve for a single helix wherein the force required to stretch diverges as the helix is straightened out, combing through a double helix shows that the force flattens out before either helix is significantly stretched. Instead, the moving tine untangles the two filaments, eventually decoupling the helix strands as the force becomes vanishingly small.

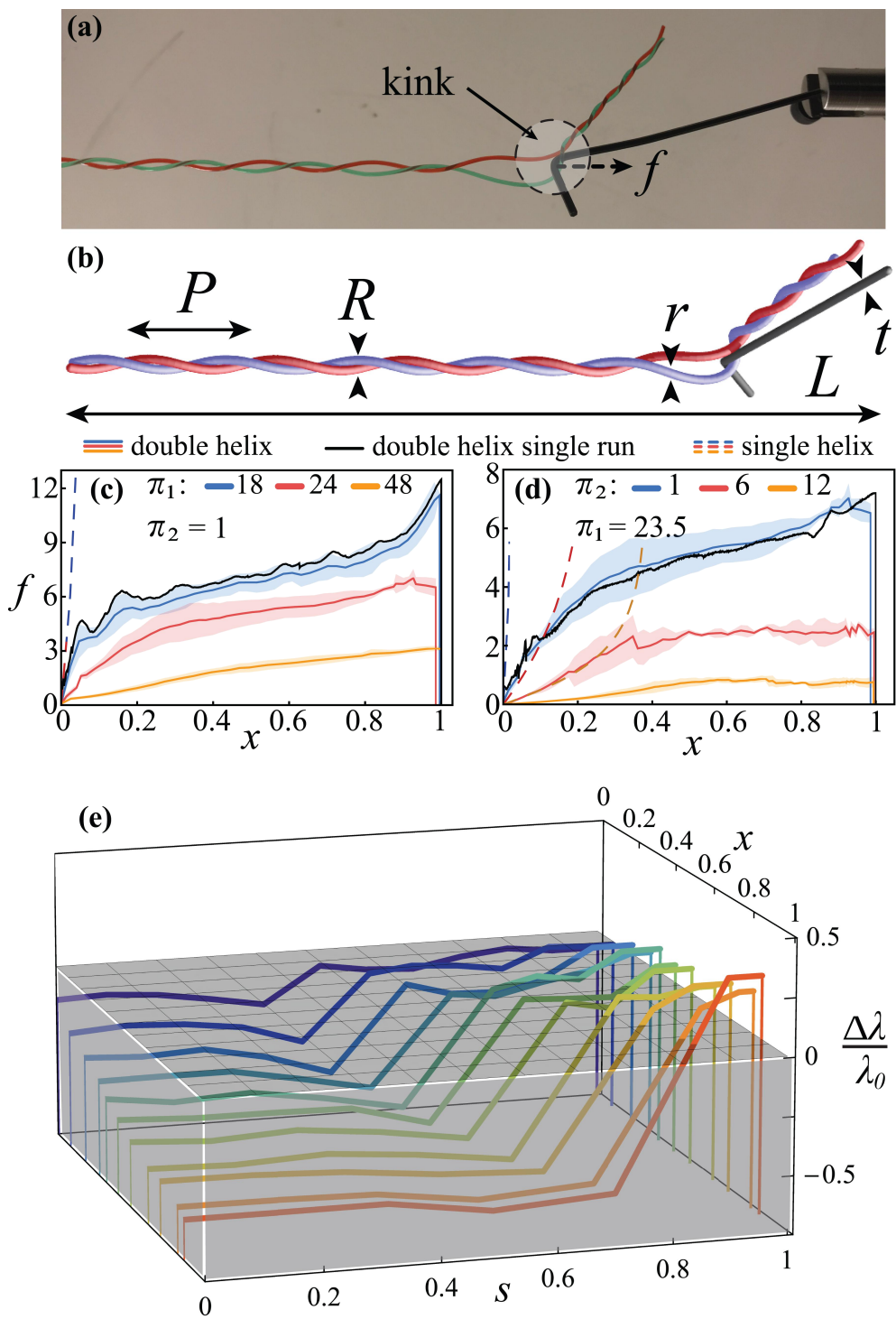
The unlinking of the homochiral helices during this process can be quantified in terms of the Calugareanu-Fuller-White (CFW) theorem^{24,19,82}, which states that $Lk = Tw + Wr$. Link (Lk) quantifies the oriented crossing number of the two filaments averaged over all projection directions (or Gauss Linking integral) and effectively counts the number of full turns one filament makes around the other⁶². Twist (Tw) is the integrated rotation of one filament around the two-filament-centerline. Writhe (Wr) is the (negative) integral of the geometric torsion of the centerline. To quantify the topology of the double helix, we treat the two interwoven filaments as two edges of a ribbon and compute the local link density $\lambda(s)$. $\lambda(s)$ is defined as the link per unit length along the double helix centerline as a function of the centerline arclength s and the twist density $\tau(s)$. For a relatively straight double helix, $Wr \approx 0$, so that $\lambda(s) \approx \tau(s)$ ³⁹. Since Lk is topologically invariant while Tw is not, we characterize the ribbon in terms of λ . In Figure 2.2(e) we show the evolution of the link density λ calculated from images of the helix taken as the tine moved. We see that a relatively uniform $\lambda(s)$ changes to a step-like $\lambda(s)$ as the tine induces a flow of link toward the free end of the curl. This leads to overwinding in front of the tine and underwinding behind while link flows through the helical braid from the clamped to the free end. For tine displacements $x \gtrsim 0.2$, the scaled jump in the link density $\Delta\lambda/\lambda_0 > 0$ across the tine (λ_0 being the initial link density) increases faster than the rate at which is expelled from the free end. This accumulation eventually reaches a plateau as the tine gets closer to the free end, and then induces a flux of link at the free end that unlinks the filaments, the end goal of combing.

We now turn to correlate the experimentally observed spatio-temporal evolution of link density associated with the motion of the tine to the evolution of the force on the tine. For a double helix that is tightly wound initially, as the tine propagates, $\lambda(s)$ ahead of the tine increases, and the scaled pitch $\pi_1 = P/r$ decreases locally, leading to a localized link pulse*, the spatial extent of which is de-

*The abrupt change in link density, termed here a link pulse, is more visible in Figure 2.3(e) than its experimental counterpart, since link density measurements could not be performed with as high of a resolution in experimental curls as in simulated ones.

Figure 2.2 (following page): Combing a double helix. **(a)** As the tine moves down the double helix, it forms a kink about which the helix whirls as link flows out of the bundle. **(b)** Schematic of combing a double helix with pitch P , helix radius R (half the distance between individual filament centerlines), filament radius r , tine radius t and helix height L . **(c-d)** Scaled force $f = \frac{l_0 F}{B}$ applied by tine over scaled distance combed $x = \frac{d}{D}$, where F is unscaled force, d is unscaled distance combed, $l_0 = 0.01\text{m}$ is a characteristic length, B is single filament bending rigidity and D is total tine displacement required to detangle the helices. Dashed curves show theoretical force predicted for stretching a single helix; black curves show a single representative combing. We scan the parameter space varying **(c)** $\pi_1 = P/r$ and **(d)** $\pi_2 = R/r$. See appendix for details and variation of $\pi_3 = t/r$. **(e)** Change in link density $\Delta\lambda$ normalized by initial link density λ_0 for $\pi_1 = 18$, $\pi_2 = 1$, plotted for several normalized tine locations, showing flow of link from clamped to free side and eventually out free end by twirling of the free ends about one another. In all experiments, $r = 4.25 \cdot 10^{-4}$ m and helix height $h = 0.15$ m.

Figure 2.2: (continued)



terminated by tine, hair, and helix radii, as well as helix nominal pitch. Increasing link density causes the double helix to stiffen and eventually the tine jams (measured as a sharp increase in the force extension curve) when the local link density is larger than a threshold that depends on the helix radius, helix nominal pitch, filament radius and the coefficient of friction. When one of the filaments slides relative to another, the relative shear often leads to the kinked configuration seen in Figure 2.2(a,b) accompanied by a peak in applied force. If the filament does not break, eventually the tine breaks through and the force decreases, before the same cycle repeats again. During this process, the kinked double helix twirls about the axis of tine motion (see Figure 2.11). If the double helix is loose enough initially, link propagates more easily from the tine location to the free end, $\lambda(s)$ never crosses the threshold needed for kinking, and the force required to comb never peaks (as seen for $\pi_1 = 48, \pi_2 = 1$). These are the only ways by which link flows out of the free end, via untwisting of the free ends of the individual filaments, and via the twirling rotation of the kinked portion of the double helix (in a manner similar to what has been observed in viscous filaments⁸⁴).

By using link, and in contrast to the use of curvature and torsion, we can completely characterize the untangling of the double helix and conditions for kinking in terms of the local density of the scalar quantity $\lambda(s)$. Furthermore, the flow of λ out the free end of the double helix corresponds well to the change in global Lk , which in turn characterizes the overall detangling of the helix in a topologically invariant way.

2.5 NUMERICAL ANALYSIS OF COMBING

To quantify our experiments on the non-linear topological mechanics of interacting filaments, we use a numerical approach that models each hair using the Kirchhoff-Cosserat theory^{17,50} and solve the equations using the discretization, contact-force and numerical integration scheme described in Gazzola et al. (2018).²⁷ In the limit of very thin filaments such as hair (where the length \gg the thickness), the model naturally reduces to the Kirchhoff-Love theory for inextensible, unsharable filaments⁴⁵. We define $s \in [0, L_0]$ as the material coordinate (also the arc length) of the rod of rest length L_0 , $x(s)$ as the position vector of the centerline, and a triad of orthonormal directors $d_1(s), d_2(s), d_3(s) = \partial_s x$ that defines the cross-section orientation. Then any body-convected vector v with lab-frame coordinates \bar{v} may be written as $v = Q\bar{v}$, where $Q(s) \in SO(3)$ is a rotation matrix, and the bending and twist strain vector is given by $\kappa = \text{vec}(\partial_s Q^T Q)$ (κ_0 is rest-state curvature). If $N(s)$ is the internal force resultant, f_g as gravitational force line density, the equilibrium equations for the boundary value problem are^{50,27}

$$0 = \partial_s N + f_g \quad (2.1)$$

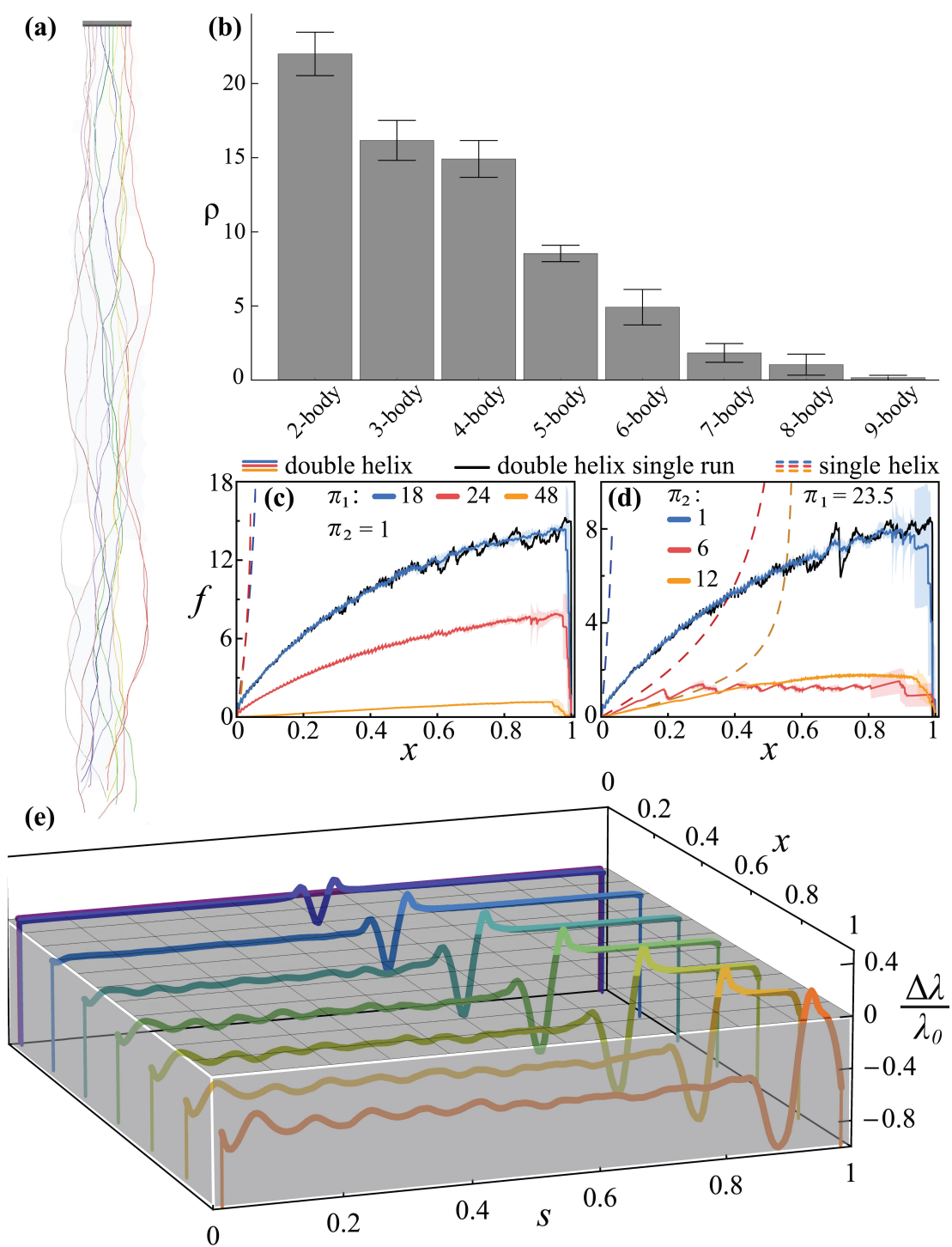
$$0 = \partial_s (B(\kappa - \kappa_0)) + \partial_s x \times n \quad (2.2)$$

where B is the matrix of bending and twisting stiffnesses, subject to the boundary conditions of the filaments being clamped at one end and free at the other.

To simulate the initial state of a curl of hairs such as that depicted in Figure 2.1(b), we start with a collection of clamped filaments hanging in a gravitational field $|f_g| = \rho A g$ ($g \approx 9.8 \text{ N/kg}$, ρ is the filament mass density and A is the filament cross-sectional area), resulting in a curl such as that shown in Fig 2.3(a). We then introduce an intrinsic curvature at each node, randomly drawn from a Gaussian distribution with mean and variance matching the distribution of curvatures (see appendix for details), shown in Figure 2.1(b). Finally, we let the hairs relax elastically to their new rest configurations, determined by a competition between nonzero intrinsic curvature and gravitational

Figure 2.3 (following page): Numerical results. **(a)** Simulated curl of 12 hairs modeling those in Figure 2.1(b). **(b)** Hair interactions as in Figure 2.1(d) for simulations similar to (a), where ρ = number of interactions per unit length (in meters). $L_0 = 0.2$ m, $r = 7.5 \cdot 10^{-5}$ m and $E = 1$ GPa. See appendix for 3-dimensional curl results. **(c-d)** Scaled force $f = \frac{l_0^2 F}{B}$ applied by tine over scaled distance combed $x = \frac{d}{D}$, where parameters are defined as in Figure 2.2. Dashed curves show theoretical force predicted for stretching single helix an equivalent distance; black curves show single representative combing. We scan the parameter space varying **(c)** $\pi_1 = P/r$ and **(d)** $\pi_2 = R/r$. See appendix for details and variation of $\pi_3 = t/r$. **(e)** Change in link density $\Delta\lambda$ normalized by initial link density λ_0 for helix with $\pi_1 = 18$, $\pi_2 = 1$, plotted for several tine locations, qualitatively reproducing experimental trends from Figure 2.2(e). Filament parameters are same as in Figure 2.2, except E values are scaled down by 0.078. See appendix for simulation settings.

Figure 2.3: (continued)



straightening (see appendix). After the hairs relax, we count interactions using the same method as used in experiments, leading to the histogram of interactions per unit length in Figure 2.3(b). We find that pairwise interactions dominate in agreement with experimental results (see appendix where we show that these interactions do not change qualitatively in a 3-D array).

To follow the combing of an elastic double helix as in Figure 2.2, we start with a random distribution of initial internal strains and anneal the pair of filaments into a double helix, clamped at one end. We then insert a rigid rod as a tine between the two helices close to the clamped end and move it quasi-statically towards the free end. As in experiments, the initial helix-tine system features links to both sides of the tine insertion point; as the tine moves toward the free end, it detangles the curls in its path. In Figure 2.3c-d we show the numerically computed force applied by the tine during combing, and see that the results are similar to our experiments shown in Figure 2.2(c,d)[†]. Comparing the evolution of the helix topology computed using the algorithms described in Charles et al (2019),¹⁵ Figure 2.3(e) shows that this also matches the experimental pattern of overwinding and underwinding shown in Figure 2.2(e); the oscillations in $\lambda(s)$ on the clamped side of the tine come from slight periodic shearing of the clamped side filament segments with respect to each other, a phenomenon that occurs on too fine a resolution to be observed in experiments. The small discrepancies between the quantitative values observed in the numerical and experimental results may come from our scaling of the simulated filaments' bending stiffness[‡].

[†]The high-frequency oscillations seen in the mean force curves are due to the oscillation in contact force between the tine and double helix filaments as the tine passes by each discretization node in the double helix filaments.

[‡]Note that the numerical calculations presented here neglect contact friction. However, we tested a subset of these simulations with contact friction and obtained force-displacement curves with the same qualitative shape as the ones shown here. Hence, for simplicity, we neglect contact friction in all simulations shown here.

2.6 OPTIMAL COMBING STRATEGY

Complementing our analysis of the topological mechanics of combing a double helix, we now consider how a curl’s resistance to combing varies with the style of combing, e.g. short strokes versus long strokes. Noting that a single helix pitch corresponds to one helix filament revolving once around the other helix filament, we fix $R/r = 1$ and $P/r = 24$ and vary q , the number of pitches that initially separate the tine from the free end of the double helix. In experiment (Figure 2.4(a)) and simulation (Figure 2.4(b)) we find that significant tine jamming—as indicated by the plateaus in the force-displacement curves—occurs only when we start combing more than 4-5 helix pitches away from the free end[§]. The differences between the two sets of curves is likely due to not accounting for friction in the computations, and explains the larger number of plateaus seen in the large- q experiments relative to the more smooth force evolution seen in computations. Nevertheless, we see that starting to comb nearer to the free end allows link to be expelled more easily, leading to complete untying before the differential link density across the tine surpasses the threshold for kink formation and jamming, consistent with experience.

To quantify this intuitive result, we define a cost $C(q)$ for combing a double helix of length L using each strategy. To illustrate the trade-offs between f_{\max} , the maximum dimensionless force during combing, and the amount of detanglement quantized in terms of the number of strokes q_0/q needed to complete the combing process ($q_0 = 25$ is a fixed number of pitches characteristic to the q -values used in these combing strategies), we use the simplest linear cost that can interpolate between pain and time. Writing this cost $C(q) = \gamma f_{\max} + (1 - \gamma) \frac{q_0}{q}$ (see appendix for details), we can vary the relative cost of the two effects by varying γ . Varying γ allows us to optimize a combing strategy based on the initial nature of the double helix; for very curly hair, choosing $\gamma \sim O(1)$ is

[§]Quantitative differences in the shape of experimental and numerical force-displacement curves in Figure 2.4 could stem from our model’s neglect of contact friction.

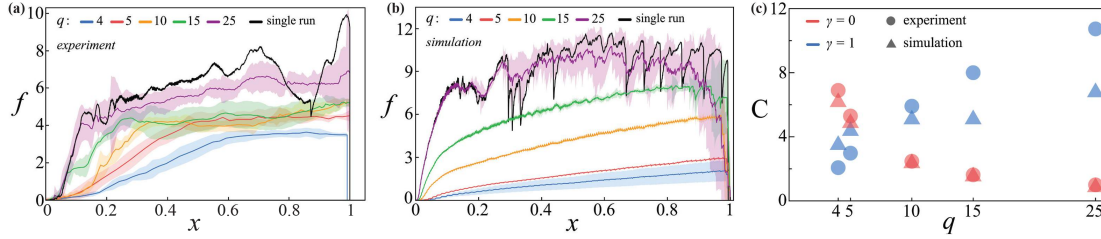


Figure 2.4: (a-b) Scaled force f over scaled distance combed x for (a) experimental and (b) simulated double helices with varying number of links. Scaling of x is different for each curve since the total raw tine displacement needed to comb each curl is different. Below a certain link threshold, combing finishes without kink formation. Black curves show a single representative combing for $q = 25$. Filament parameters are the same as in Figure 2.2. (c) Cost C to comb a 10m double helix over number of downstream pitches q detangled per combing, using the strategies shown in (a-b). Note that q is intrinsic to combing strategy. C combines effective pain and time required to comb; $\gamma = 0$ considers only time and corresponds to straight hair; $\gamma = 1$ considers only pain and corresponds to curly hair. Simulation and experiment how optimal combing strategy shifts depending on hair curvature.

more sensible, while for straight hair, choosing $\gamma \sim 0$ is better. Using the results for the maximum force from Figure 2.2-2.3, we calculate the cost $C(q)$ for the case of curly and straight hair. In Figure 2.4(c), we see that for straight hair ($\gamma \sim 0$), the cost decreases as q increases, i.e. the number of strokes decreases, while for curly hair ($\gamma \sim 1$), the cost is lowest for small q as it is biased to minimize the cost associated with the maximum force.

2.7 CONCLUSIONS

Our study has shown that the many-body problem of combing relatively straight hair can be simplified to the problem of combing a double helix, and in this context, we have provided a measure of link density during combing as a function of helix geometry and combing procedure. We have connected topology, geometry and mechanics by quantifying the relation between flow of link through the tine and out the free end, to the time-varying force felt on the tine. Our results also suggest that the two-body problem also has the ability to capture the correct optimal strategy of combing a tangle by balancing the cost of many short strokes relative to longer, potentially more painful ones. While hair material and internal geometric properties such as stiffness, frictional coef-

ficient, pretwist and cross-sectional shape would likely quantitatively impact our results, we expect the connections presented here between mechanics, geometry, and topology to be applicable to any curl of hair. Going forward, a natural next step is to account for variations in these material properties, hairs' strong frictional anisotropy, and hairs' response to combing as a function of humidity and temperature.

ACKNOWLEDGEMENTS.

For partial financial support, we thank the National Science Foundation grants NSF DMR 20-11754, NSF DMREF 19-22321, and NSF EFRI 18-30901.

2.8 APPENDIX

HAIR CURL INTERACTIONS

In Figure 2.1(d) (main text), we show the number of N -body interactions as a function of N in a relatively straight curl of horse hair, finding that two-body interactions dominate. To quantify the nature of these interactions, we segment the curl into sections, and then count and characterize the internal interactions of each strand using the interaction definitions in Figure 2.1(c), noting that our definition of interaction is an upper bound on the true number of interactions.

We note that the dominance of two-body interactions depends, to some degree, on the length of segment used to compartmentalize the curl. Taking the limiting cases, one can see that as the segment length approaches zero, only two-body interactions will be seen, while as the segment length approaches the total length of the curl, only a single interaction will be seen: that involving every hair (except those hairs which never cross other hairs, which can effectively be excluded from the bundle since they do not contribute to the tangle). Since our goal is to investigate the local interactions making up the global tangling of the hair, we sought a segment length that would isolate local

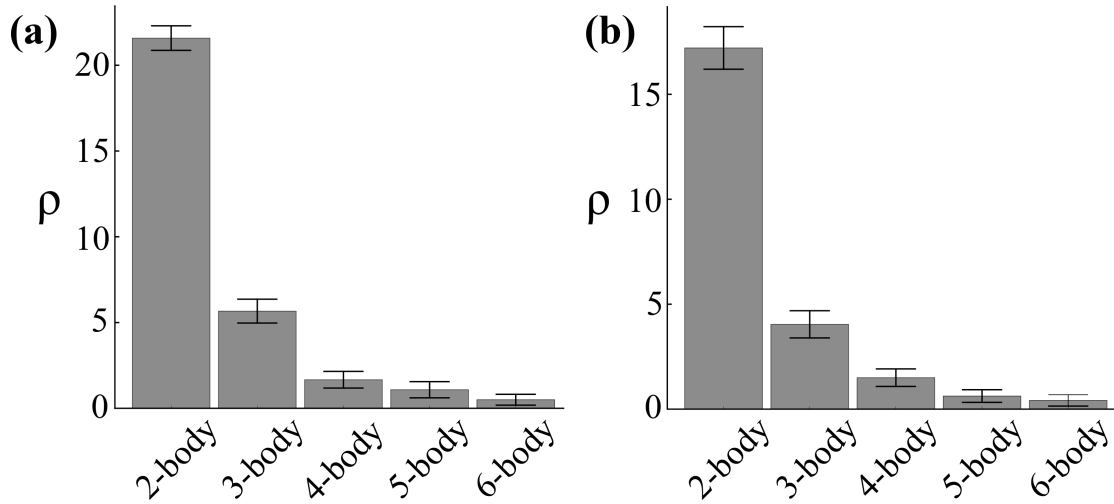


Figure 2.5: Hair curl interactions in three dimensions. Histogram of hair interaction types for simulated curls similar to those used for Figure 2.3(b) of the main text. Here, we clamp the top of the hairs in a planar triangular lattice, letting all hairs hang down in the same direction, loosely filling a volume of space below the triangular lattice. We segment the curl into 20 layers, count interaction types defined in Figure 2.1(c) (main text) within each layer and average over all layers and curls. In three dimensions we can no longer use projected intersections to define hair interactions. In (a) we define an interaction by hairs being in contact. In (b), we use a linking number threshold to define interactions. In particular, we segment the curl into twenty segments; in any single segment, if $Lk(A, B) > m$, where A and B are the parts of two hairs which lie in the given segment, then A and B interact. We empirically determine that $m = 0.4$ is roughly the smallest linking threshold that provides nontrivial segregation of interaction types. Presumably, were m and segment length scaled equivalently, results would change only as a function of segment length, not directly as a result of changing m . Here $\rho =$ number of interactions per unit length (in meters), and we again find pairwise interactions to be dominant. Bar height represents mean ρ while error bars show standard error in ρ .

interactions—i.e., those that take place over a length scale comparable to the characteristic length over which the hair curves. We chose 20 segments empirically to produce a segment length roughly equal to that characteristic length.

We also note that, while the plurality of two-body interactions would likely be less pronounced for curlier hair, we restrict ourselves to relatively straight curls—i.e., an individual hair’s radius of curvature is on the same order as its length. Other curl properties, such as volume density of hairs in the region of space occupied by the curl, hair thickness, and average hair curvature, may also affect the precise relative abundances of N -body interactions. However, for this study, we limit ourselves to dry-combing of relatively straight horse and human hair, focusing on the potential to reduce a

complex many-body problem to a feasible two-body problem, and leaving for future work a more detailed investigation of variations between curls.

To reproduce the computation leading to Figure 2.3(b) of the main text, now generalizing the result to hairs interacting in a fully three dimensional context, we simulate twelve hairs with their top ends clamped in a planar triangular lattice. The hairs hang freely down from their clamped tops, loosely filling the volume below the triangular lattice. As with the two-dimensional array of hairs considered in Figure 2.3(b), we then introduce intrinsic curvature into the hairs. The random curvature at each node of each hair is sampled from a Gaussian distribution of curvatures with mean 0 and standard deviation $\frac{1}{m}$, matching the local curvatures of the hairs used in experiment.

To study hair interactions, we use similar methods to those used in Figure 2.1(d) and 2.3(b) of the main text. However, we can no longer use the crossing criterion for determining whether two hairs interact, since this ignores the three dimensional nature of the curl. Instead, we employ two interaction criteria which lead to similar results: in Figure 2.5(a), we use contact; in Figure 2.5(b) we consider two hairs to interact within a single layer of the curl if the Lk between the segments of the two hairs within that layer is greater than a fixed threshold, here set to $Lk_{\text{thresh}} = 0.4$, determined empirically to maximize intersection classification accuracy. We again find pairwise interactions to be the most prevalent, regardless of the definition of an interaction.

Although it is quite difficult to perform this same study on an experimental fully three-dimensional curl of hairs, we can extrapolate from our numerical results that pairwise interactions would dominate in such an experimental curl as well. In particular, the qualitative similarity between Figs. 2.1(d) and 2.3(b) of the main text suggests that real hair curvatures are distributed similarly to the independently randomly sampled curvatures used in simulation. By comparison to the procedure used in simulation, the similarity between simulated and experimental results (Figs. 2.1(d) and 2.3(b) of the main text) implies that for real hairs, there is significant statistical independence between the local hair curvatures at points close in arclength along the same hair and equivalent points

on nearby hairs. To curls of hair characterized by such independence, we apply the term “thermalized,” and hence conclude that our computational results on thermalized three-dimensional curls should mimic what would be seen in a real curl.

ELASTICITY VERSUS GRAVITY IN FREE-HANGING HAIR

In Figure 2.1(b) of the main text, we show a curl of hair used in studying hair interactions. Upon close inspection, one can see that at the bottom of this curl, the hairs appear to flair out – i.e. the curvature of the hanging hairs appears to be greatest in a small region at the bottom of the hairs. The characteristic length l_g of an individual hair (radius r , bending stiffness B) at which gravity is balanced by elasticity is given by $l_g \sim (B/\rho g r^2)^{1/3} \sim (Er^2/\rho g)^{1/3}$. For hair that has a natural curvature κ^* , when $l_g \kappa^* \gg 1$, gravity is unimportant. This is equivalent to stating that near the free end of the hair, it naturally curls up into its rest curvature while straightening out elsewhere.

Thus, we should not then be surprised that, in Figure 2.1(b) of the main text, the region at the bottom of the hairs in which the hairs flair out according to their natural curvatures is quite small.

APPLYING THE SINGLE HELIX EXTENSION CURVE TO COMBING A DOUBLE HELIX

To gain insight into the effects of inter-filament contact during combing, we compare our force-displacement curves (Figures 2.2-2.3 in the main text) to the naive curves obtained using the analytic force-extension curve predicted by Love⁴⁵. Love considers a filament for which the rest configuration is a single helix with angle α and helix radius R . If one end is clamped, the external load F and torque M which must be applied axially to the helix’s free endpoint to deform it to a helix along the

same axis with angle α_1 and radius R_1 are shown to be

$$F = C \frac{\cos \alpha_1}{R_1} \left(\frac{\sin \alpha_1 \cos \alpha_1}{R_1} - \frac{\sin \alpha \cos \alpha}{R} \right) - B \frac{\sin \alpha_1}{R_1} \left(\frac{\cos^2 \alpha_1}{R_1} - \frac{\cos^2 \alpha}{R} \right) \quad (2.3)$$

$$M = C \sin \alpha_1 \left(\frac{\sin \alpha_1 \cos \alpha_1}{R_1} - \frac{\sin \alpha \cos \alpha}{R} \right) + B \cos \alpha_1 \left(\frac{\cos^2 \alpha_1}{R_1} - \frac{\cos^2 \alpha}{R} \right) \quad (2.4)$$

. We apply the above formula for F to our experimental and numerical double helices.

To apply Love's result to our experimental double helices, we assume that the tine initially sticks to its initial position within the filaments—an assumption validated by the initial conservation of link and overwinding early on in the combing experiments (Figure 2.2). We neglect the free side, considering only the initially stretching of the clamped side, and compute the change in helix angle throughout the clamped side of the double helix. In particular, if the tine sticks to the filaments, then tine displacement d equals change in length ΔL of the clamped-side helix, and the arclength S of the clamped side of the underlying filaments (i.e. the arclength of the section of the underlying filaments extending from the clamp to the tine) remains constant. Using $\alpha = \sin^{-1}(L/S)$, we compute the new helix angle

$$\alpha_1 = \sin^{-1}((L + d)/S) \quad (2.5)$$

where L is the initial length of the clamped side of the double helix.

How we compute the new helix radius R_1 relies on whether the double helix is tightly wound (i.e. $R/r = 1$). If $R = r$, then the radius cannot change, so we set $R_1 = R$. If, on the other hand, $R > r$, we again apply the no-slip tine assumption. In particular, if the tine sticks to both underlying filaments, then the angle traversed by each filament about the helix centerline from the clamp to the tine remains constant. Calling this angle χ , we have

$$\chi = \frac{S \cos \alpha}{R} \quad (2.6)$$

as constant, so

$$R_1 = R_0 \frac{\cos \alpha_1}{\cos \alpha_0}. \quad (2.7)$$

Combining this result (for $R > r$, or using $R_1 = R$ for $R = r$) with our result for the new helix angle α_1 , we can apply Love's formula for F above.

Note that in Figure 2.2 of the main text, the single-helix curve hugely overestimates the force required to stretch a tightly-wound ($R/r = 1$) double helix. We can understand this by noting that to keep filament length constant, stretching a tightly-wound helix requires unwinding the helix. In particular, since $\chi = S \cos \alpha / R$ and α increases toward $\pi/2$ with stretching while S and R remain constant, χ will decrease toward 0. As χ approaches 0, the filament becomes nearly straight and the force required to continue stretching diverges. Hence, the theoretical single-helix force quickly diverges for our tightly-wound double helices. Note that for tightly-wound helices, we cannot simultaneously apply a no-slip assumption, keep $R_1 = R$ constant, and assume no stretching of the underlying helix filaments. In reality, the tine likely does not entirely stick to the filaments even initially in the tightly-wound case. However, since twirling does not immediately begin in this case and we see overwinding behind the tine, the tine must somewhat pull the underlying filaments along with it, justifying the use of the no-slip assumption as a rough approximation of how the filaments underlying the double helix are actually stretched. A similar failure of the no-slip condition likely explains why the single-helix curve also overestimates the true force felt in the experiments with $R > r$.

When applying the single-helix extension formula to our numerical double helices, we have the freedom to use the exact shape of the helix at each time step, since such data is readily accessible from the simulation. However, for consistency, we apply the same no-slip assumption described above to our simulated double helices. Hence, in Figure 2.3 of the main text we again see that the single-helix curve overestimates the combing force for the same reasons as in Figure 2.2.

VARYING TINE RADIUS

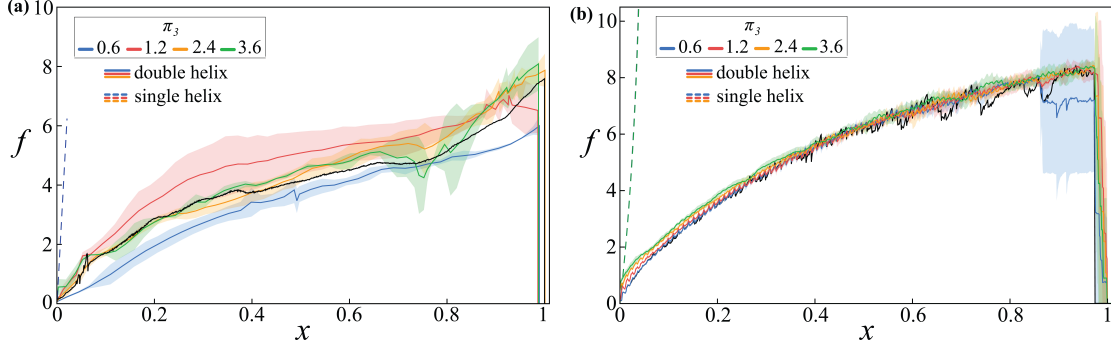


Figure 2.6: Force to comb a double helix under variation in tine radius t in (a) experiment and (b) simulation. We show scaled force $f = \frac{l_0^2 F}{B}$ applied by tine over scaled distance combed $x = \frac{d}{D}$, where F is unscaled force, d is unscaled distance combed, $l_0 = 0.01\text{m}$ is reference length, B is single filament bending rigidity and D is total tine displacement required to fully unlink the tangle. Dashed curves show theoretical force predicted for stretching single helix an equivalent distance. Black curves show a single representative combing, for $\pi_3 = t/r = 1.2$ in (a) and $\pi_3 = 0.6$ in (b). We vary tine radius relative to hair radius $\pi_3 = t/r$, keeping helix radius $R = r$ and pitch $P = 23.5r$ fixed. Comparing to Figures 2.2 and 2.3 of the main text, t affects combing force much less than R or P . Note that all combing experiments and simulations in main text used $\pi_3 = 0.9$.

To explore the double-helix parameter space, we varied three dimensionless ratios of length scales: $\pi_1 = P/r$, $\pi_2 = R/r$ and $\pi_3 = t/r$. The effects of varying π_1 and π_2 are shown in Figures 2.2 and 2.3 of the main text. In Figure 2.6, we show the effect of varying π_3 . Contrasting Figure 2.6 to Figures 2.2 and 2.3, we see that the effect of tine radius on the force required to comb the curl is much smaller than that of the helix pitch or radius.

UNCERTAINTY IN FORCE-DISPLACEMENT CURVES

In Figures 2.2(c,d), 2.3(c,d), 2.4(a,b) and 2.6, we show mean combing force as a function of tine displacement, with a cloud depicting the standard deviations in force during combing. In Figure 2.7 we report quantitatively the mean of combing force standard deviation relative to mean combing force $\sigma/f = \langle \sigma(x)/f(x) \rangle$ for each parameter set tested. In all cases except $n = 4$ in Figure 2.7(d), corresponding to the force-displacement curves in Figure 2.4(b), $\sigma/f \lesssim 0.2$. However, looking at

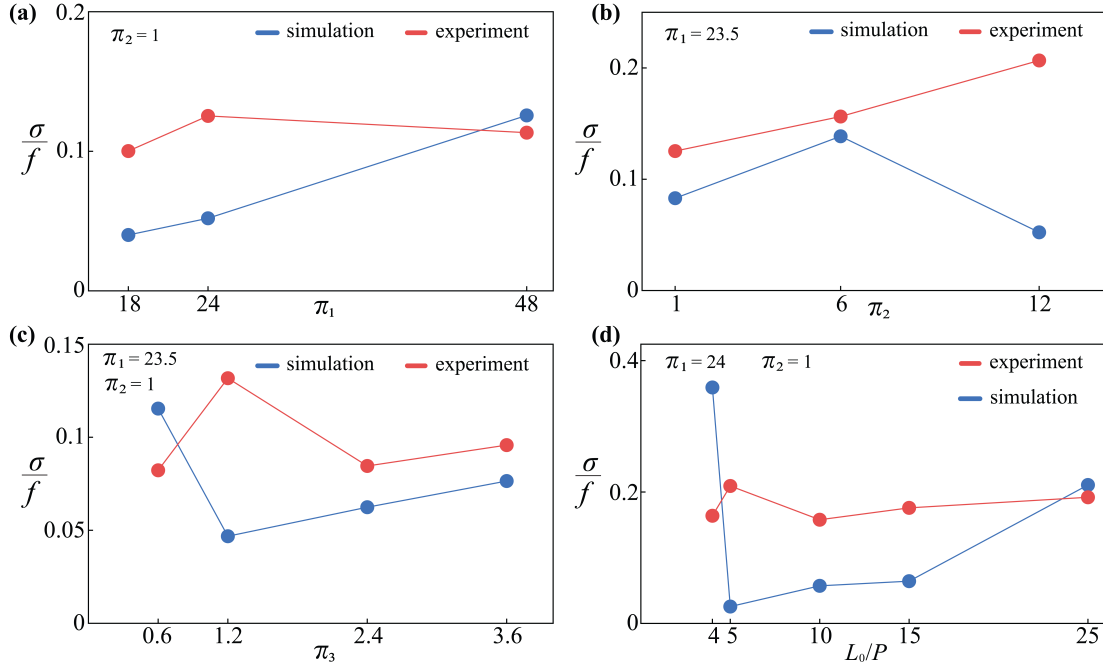


Figure 2.7: Variations in force-displacement curves. We show the average (over time) of standard deviation relative to mean combing force $f/x = \langle \sigma(x)/f(x) \rangle$ for each parameter set in (a) Figs. 2.2c and 2.3c, (b) Figs. 2.2d and 2.3d, (c) Figure 2.6 and (d) Figs. 2.4a-b. In most cases, combing force standard deviation is below the mean combing force by a factor of 5-10.

the corresponding force-displacement curve in Figure 2.4(b), the larger value of σ/f appears to come, at least partially, from the small mean combing force. We expect this run to have a smaller mean combing force than the others, since we are detangling the fewest links in this case.

LINK CURRENT

In Figure 2.8 we show the rate at which Link leaves the double helix, or link current dLk/dx , through the free end, for the experiment used in Figure 2.2(e) and simulation used in Figure 2.3(d). The experimental link current appears more jumpy because we are only able to sample the total Link at discrete times during the experiment. From the experimental link current shown in Figure 2.8(b), we can see a distinct trend: at first Link leaves the double helix slowly. Then, once the link density

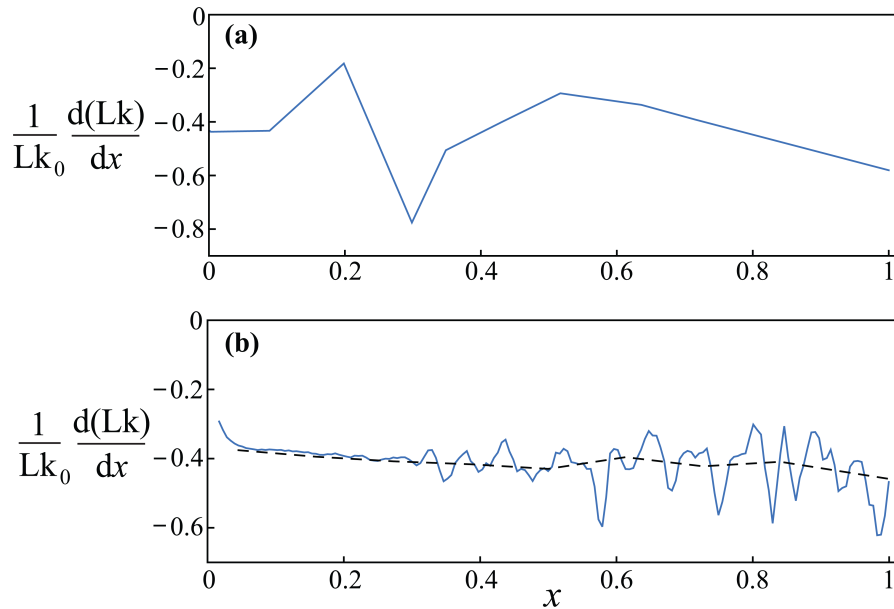


Figure 2.8: Link current. We show the rate of Link dLk/dx flowing out the free end of the double helix as a function of tine position x , relative to initial total Link Lk_0 , for (a) the experimental combing analyzed in Figure 2.2(e), and (b) the simulated combing analyzed in Figure 2.3(e). The experimental link current appears jumpy due to the fact that we can only sample the total link at discrete time intervals during the combing. In the numerical version of this experiment, we sample the total link nearly continuously (solid blue curve shows continuous Lk while dashed black curve shows moving average) and find a distinct pattern of linking current: the current starts small and negative while the gradient in link density builds up around the tine. As the link density gradient near the tine increases, Link is pushed toward the free end and hence the magnitude of the linking current increases. As link starts to flow out the free end at a constant rate, the link current plateaus, until finally the tine detangles the entire double helix.

gradient across the tine and, hence, the overwinding ahead of the tine, passes a critical threshold, the magnitude of the link current increases to a plateau. This plateau value corresponds to the rate at which Link is pushed out of the double helix through the free end while the tine forces more Link from the clamped toward the free end as it leaves detangled filaments in its wake. Note that the plateau value of link current and combing distance required before the link current plateaus depend on the geometry of the particular helix being combed; e.g., tighter curls (smaller P and R) would accelerate overwinding ahead of the time, and likely cause the link current to plateau earlier and at a higher value. We show Figure 2.8 as a representative example for one choice of helix parameters.

Note that Link is naturally defined as a global quantity⁶². While a local linking current has been constructed³⁹ it is difficult to apply it to a series of discrete snapshots of a ribbon without accumulating significant errors from finite time and space discretization. However, the centerline of the double helices combed in Figures 2.2-2.3 of the main text remain nearly planar. Hence, there is no global or local Writhe to speak of, and we can approximate local link density with local twist density, $\lambda \approx \tau$. Fortunately, Twist Tw is naturally defined as an integral of the local twist density τ , making τ much easier than λ to compute accurately. Note that λ shown in Figure 2.3(e) (main text) and Lk shown in Figure 2.8 were computed for simulated double helices using the algorithms described in Charles et al (2019).¹⁵

COST OF COMBING

In Figure 2.4(c) of the main text, we show the cost of combing an imaginary $L = 10m$ long double helix using the combing strategies studied in Figure 2.4(a,b). Consistent with the experiments shown in Figure 2.4(a) of the main text, we assume the imaginary double helix has $r = 0.000425m$ and $P/r = 24$. In the main text, we note that one pitch corresponds to one helix filament making a single full revolution around the other helix filament, mathematically equivalent to one link. We then define q to be the number of pitches between the tine insertion point and braid free end. Hence the length- L braid has $q_{\text{tot}} = L/P = 1000$ links that must be combed through.

We imagine combing the long double helix using a sequence of combings, each of which detangles q links, or pitches, of the long double helix. For the first combing, the tine is inserted q pitches away from the free end, and is pulled through to the free end, detangling those q links. For each subsequent combing, the tine is inserted q pitches further away from the free end than it was inserted for the previous combing. Each time, it is pulled through to the free end, detangling q new pitches. In all combings after the first one, the tine must push the q pitches through some amount of previously-detangled helix arclength. During this part of the combing, no new links build up in

front of the tine; rather, the tine causes the q links to translate down the double helix to the free end.

Our cost function incorporates effective pain inflicted and time spent combing the curl; letting $f_{\max} = F_{\max} \left(\frac{\ell_0}{B} \right)$ be the maximum dimensionless force felt during combing, we choose the simplest cost that can interpolate between these two contributions:

$$\text{Cost } C(q) = \gamma f_{\max} + (1 - \gamma) \frac{q_0}{q} \quad (2.8)$$

where $q_0 = 25$ is a fixed number of pitches characteristic to the q -values used in these combing strategies, and $\gamma \in [0, 1]$ spans possible hair geometries. In particular, as indicated by the force-displacement curves in Figures 2.2-2.3 of the main text, combing curly hair requires more force, hence more pain, while combing straight hair is rather painless. Hence, setting $\gamma = 1$ selects the pain term from the cost and corresponds to combing curly hair, while $\gamma = 0$ chooses the time term and corresponds to combing straight hair.

Note that our cost function implicitly incorporates an approximate mechanical work performed in combing the length- L helix using each combing strategy. To see this, consider $C(q)^2$:

$$C(q)^2 = (\gamma f_{\max})^2 + 2\gamma(1 - \gamma)f_{\max} \frac{q_0}{q} + (1 - \gamma)^2 \frac{q_0^2}{q^2}. \quad (2.9)$$

The cross-term is proportional to a product of f_{\max} and $\frac{q_{\text{tot}}}{q}$, the latter of which is the total number of combings $\eta(q)$ required to detangle the length- ℓ braid. Since most combing occurs after overwinding has occurred, the mechanical work performed by the tine is

$$W \propto f_{\max} \sum_{i=1}^{\eta(q)} i \propto f_{\max} (\eta^2 + \eta). \quad (2.10)$$

The cross term in $C(q)^2$ incorporates the linear term in this expression for work; hence, while not

directly incorporating mechanical work, our cost is closely related to the work done by the tine.

SIMULATION SETTINGS

We model each hair using the Cosserat theory of elastic rods^{17,50}, and solve the governing equations using the numerical method of Gazzola et al. (2018) and Charles et al. (2019)^{27,15}. To simulate large numbers of hairs at once, we parallelize the integration scheme within each timestep, computing forces and torques and updating filament positions, velocities and other quantities for all filaments simultaneously. To parallelize computation of contact forces, we check each filament separately for contact with other filaments, and only update the given filament's external forces, avoiding multiple calls to the same memory block by different threads at the same time.

We use the simulation and filament parameters laid out in Figures 2.9 and 2.10, where we define the characteristic damping coefficient as

$$\gamma_{char} = m/(l_0 \cdot t_{char}), \quad t_{char} = l_0/v_{char}, \quad v_{char} = \sqrt{F_C l_0/m} = \sqrt{\pi^2 EI/(m l_0)} \quad (2.11)$$

for a filament of total mass m with characteristic length scale l_0 , stretched by the characteristic force $F_C = \pi^2 EI/l_0^2$, the critical compressive buckling force of an inextensible filament. Thus,

$$t_{char} = \sqrt{4m l_0^3/(Er^4 \pi^3)} \text{ seconds}, \quad \gamma_{char} = \sqrt{Er^4 \pi^3 m/(4l_0^5)}. \quad (2.12)$$

For double helix simulations, we use $l_0 = 0.01$ m, $m = l_0 \lambda$, where $\lambda = (6.65 \cdot 10^{-4})$ (kg/m) is a typical mass per unit length for nylon filaments of radius $r = 4.25 \cdot 10^{-4}$. Since the simulations occur quasi-statically, we rescale mass m and gravitational field g inversely, keeping mg constant while increasing m by a factor of $7.52 \cdot 10^5$ to increase simulation stability.

For hair bundle simulations, we use $l_0 = 0.01$ m and $m = l_0 \lambda$ with $\lambda = 3.1 \cdot 10^{-6}$ m. We again

Figure 2.9: Table: double helix simulation parameters

radius r	$4.25 \cdot 10^{-4} \text{ m}$
helix height b	0.15 m
damping γ	$353 \text{ kg}/(\text{ms}) \approx 164\gamma_{\text{char}}$
mean E	0.27 GPa
Poisson ratio ν	0.5
spatial discretization δl	0.014 m
time discretization δt	$(0.08 \frac{\text{s}}{\text{m}}) \delta l$

Figure 2.10: Table: hair crossings simulation parameters

radius r	$7.5 \cdot 10^{-5} \text{ m}$
hair length L_0	0.2 m
damping γ	$800 \text{ kg}/(\text{ms}) \approx 9.2 \cdot 10^4 \gamma_{\text{char}}$
E	1 GPa
Poisson ratio ν	0.5
spatial discretization δl	0.002 m
time discretization δt	$(0.008 \frac{\text{s}}{\text{m}}) \delta l$

rescale m and g inversely keeping mg constant, this time increasing m by a factor of 10^8 to increase simulation stability.

EXPERIMENTAL AND COMPUTATIONAL IMAGES OF COMBINING A DOUBLE HELIX

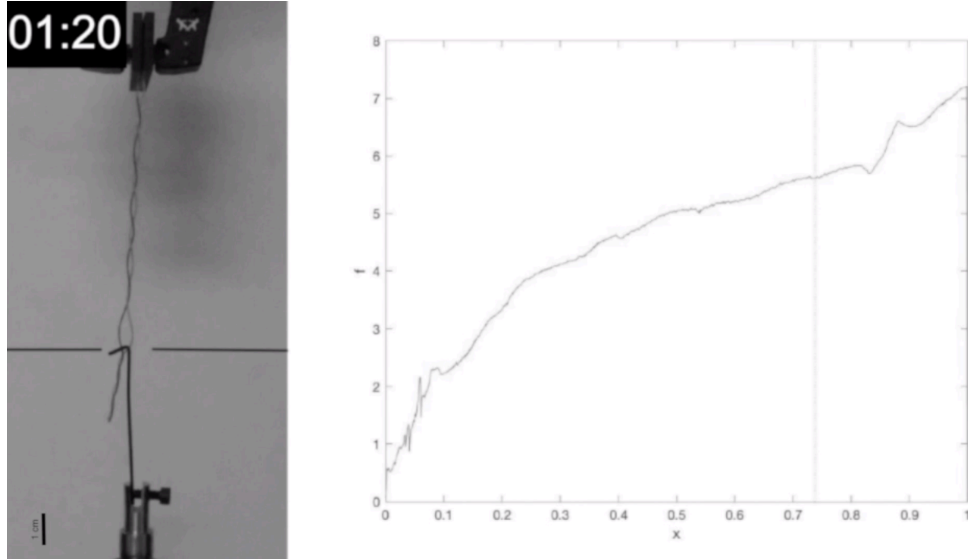


Figure 2.11: Experimental combing of a double helix. We mold two nylon filaments around a helically-grooved cylinder, forming them into two identical helices that we entwine into a single double helix. We clamp the double helix at one end and let the other end hang freely. This assembly is then pierced at the midpoint of the double helix centerline arclength by a single stiff rod which moves downward to detangle the curl. We use an Instron 5566 material testing machine to measure the force extension curves of a stiff rod piercing and pulling downward on the pinned, hanging helices. Here we show the combing process and corresponding force-displacement curve. The experiment shown is the same as that used to generate Figure 2.2(e) of the main text, with $\pi_1 = 18$, $\pi_2 = 1$.

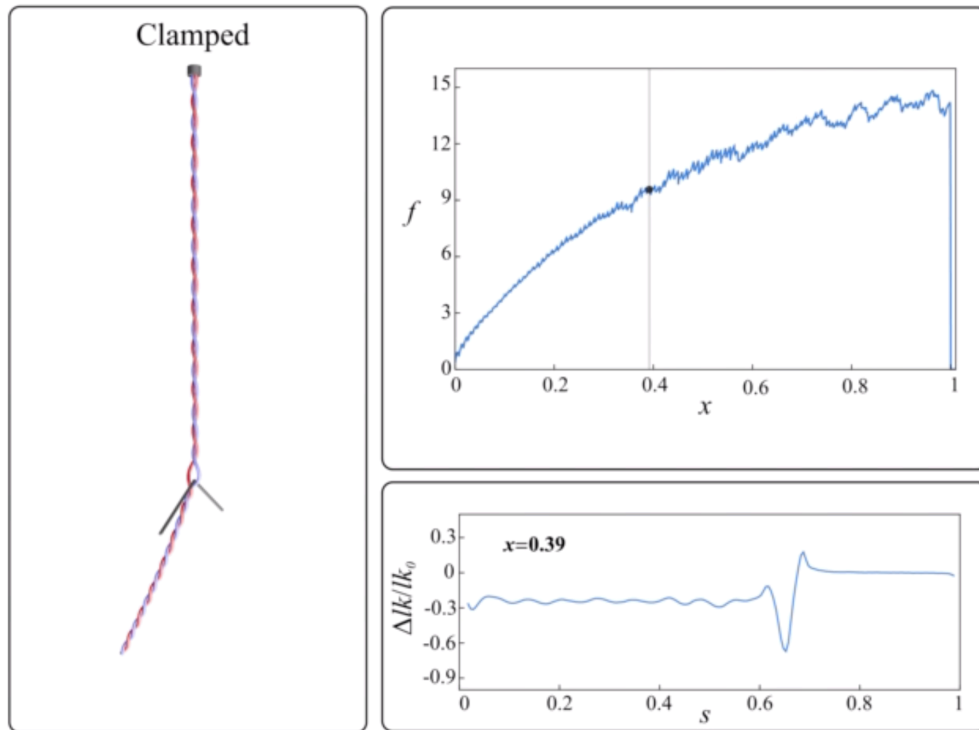


Figure 2.12: Simulated combing of a double helix. We clamp a double helix at the top allowing it to hang free. We insert a tine halfway down the tangle and gradually displace the tine toward the free end at a constant rate. The simulation proceeds quasi-statically. We show simultaneously a visualization of the combing process, the force-displacement curve and the local change in link density as a function of rescaled arclength s and rescaled tine displacement x . The simulation shown corresponds to the one used to generate Figure 2.3(e) of the main text, with $\pi_1 = 18$, $\pi_2 = 1$. See Tables 2.9 and 2.10 for simulation settings.

Prose is like hair; it shines with combing.

Gustave Flaubert

3

Detangling hair using feedback-driven robotic brushing

Building on the results of the paper presented in Chapter 2, with Josie Hughes, Nicolas Charles, L. Mahadevan, and Daniela Rus, we published a paper on feedback-controlled robotic hair brushing in the proceedings of the 2021 IEEE International Conference on Soft Robotics. This work also validates our geometric and topological modeling of hair detangling in a more applied setting. The full paper is included here, with minor edits to the format. The references are likewise altered from the original publications to fit this dissertation.

3.1 ABSTRACT

The brushing of hair requires a complex understanding of the interaction between soft hair fibers and the soft brushing device. It is also reliant on having both visual and tactile information. Guided by a recently developed model of soft tangled fiber bundles, we develop a method for optimizing hair brushing by robots which seeks to minimize pain and avoid the build up of jammed entanglements. Using an experimental setup with a custom force measuring sensor and a soft brush end effector, we perform closed-loop experiments on hair brushing of different curliness. This utilizes computer vision to assess the curliness of the hair, after which the hair is brushed using a closed loop controller. To demonstrate this approach hair brushing experiments have been performed on a wide variety of wigs with differing amounts of curl. In addition to hair brushing the insight provided by this model driven approach could be applied to brushing of fibers for textiles, or animal fibers.

3.2 INTRODUCTION

Soft robotics is rapidly furthering our understanding of the design, control and fabrication of softer structures and systems⁶⁶. It is also extending our understanding of how we interact with complex soft objects and environments⁶⁸ through the provision of improved modeling techniques and controllers. This expands the range of materials and environments within which robots can operate effectively, allowing robots to perform some of the more complex tasks that humans perform with ease. One such application where this is particularly true is in assistance and care robots¹⁶. With the globally increasing population, longer life expectancy and growing demands on health care systems, the use of robots in personal care and assistance is one area where robots could make a significant humanitarian impact⁶³.

With current advances in soft robotic technologies, machine learning and modelling, developing robots for care and health care applications is becoming increasingly feasible⁶. Within this domain



Figure 3.1: Experimental setup for the investigation of robotic hair brushing showing the wig, sensorized brush and robot arm.

one task which has had limited exploration is hair-brushing. Although a routine task for humans, it relies on a complex understanding between the interaction between the deformable brush bristles and the soft hair fibers, and requires both visual and tactile feedback. Hair brushing is typically a self-care task, however for those who cannot perform the task, it has been shown that having assistance in this task benefits both mental and physical health.³⁵

Within the domain of robots for personal care, there have been a number of notable examples. There has been the development of robotic systems for hair washing³⁴, shaving and make-up assistant robots^{74,73}, and rehabilitation robots⁵⁸. There is also increasing interest in the possibilities for

robotic care-givers, or robots that support human care-givers⁵⁴. To allow robots to extend their task solving abilities to more complex tasks such as hairbrushing, we need not only novel safe hardware, but also an understanding of the complex behavior of the soft hair and tangled fibers.

The goal of this work is to develop a platform to explore the complex task of the manipulation and brushing of hair fibers —in particular, to develop a model of soft fiber bundles which accounts for complex tangling behavior when undergoing manipulation or brushing interactions. The ability to manipulate soft fiber bundles has a wide range of applications including hair brushing or textile fiber manipulation. In this project we will focus on how the model can be applied to the problem of hair brushing, developing a control approach to allow a robot with a sensorized soft bristle brush to comb hair using an approach which minimizes the pain felt by the user, and the time spent undertaking the procedure.

This task is complex as every head of hair is different, and the interaction between hairs when combing is highly complex, with jamming and tangles forming depending on the brushing strategy used. If the incorrect brushing strategy is used, the process can be very painful and damaging to the hair. Thus, we need to understand the interactions between the soft hair strands to identify the principles of an efficient hair brushing technique. In addition, we need to develop methods of incorporating sensory information (visual and force feedback) to create an effective brushing strategy. Whilst there has been some prior modelling and investigation of hair brushing and combing, the focus has predominantly been on the mechanical, dynamic and visual properties of hair^{2,65,64}, as opposed to the tangling and combing behavior.

Our approach to robot hair brushing utilizes a model of entangled soft fiber bundles as sets of entwined double helices. This provides an improved understanding of hair brushing and entangled hairs and allows us to identify the key characteristics of soft hair which influence brushing strategies. To brush and manipulate the hair we have created a soft bristle end effector which is sensorized to allow forces during brushing to be measured. Using this sensorized soft brushing end effector (Figure

3.1), we can explore how this model can be used to optimize the control strategy for hair brushing. Using this setup, we propose a control strategy that uses force-feedback from the sensorized brush. We demonstrate this approach on a number of wigs which represent a wide range of different hair styles and types, and demonstrate how our control approach utilizes our improved understanding of hair combing to minimize both time and pain. As such, we make a number of contributions:

- A robotic setup with a sensorized soft brushing end effector that allows for hair-brushing to be investigated
- A control strategy based on a novel model of the tangling of soft bundles of fibers
- Demonstration of the approach on a number of different hair types

The remainder of the paper is organized as follows. Section II introduces the methods, including the model of tangled fibers used, and how this has been used to inform the development of a control strategy. Section III presents the experimental setup for the hair brushing experiments, and the methods of sensorizing the system and implementing the control strategy. The results from experiments are given in Section IV, which is followed by Section V, a discussion of the outcomes of the paper and a review of the main conclusions.

3.3 METHODS

MODEL OF UNTANGLING NATURAL CURL

The complexity of modeling hair combing arises from the many-body and extended nature of the entangled hair interactions. To better understand the behavior of untangling, we consider a minimal model for the combing of a double helix⁵⁶. Although combing involves interactions with the many-body bundle of entangled hairs, recent experimental results in Plumb-Reyes et al. (2021)⁵⁶ suggest

that the dominant interactions are of a pairwise (i.e., two-body) nature. Thus a model that considers two entwined helices of the same chirality, clamped at the top end and hanging freely at the bottom (Figure 3.2), with a single, stiff comb bristle moving through the double-helix is sufficient to explain the mechanics of combing qualitatively.

There are two key phenomena involved in this interaction: link current and over/under winding. Over- and under-winding describe the stretching of the clamped end of the helices (between the fixed upper base and the comb) and the compression of the free end, respectively. When the comb is moved through the helix there is generally an initial rise in the force extension curve before a leveling off, corresponding to an initial over-winding of the helix in front of the tine before a current of link⁶², a topological measure of entanglement, leaves through the free end and softens the curve.

Considering these phenomena can also help explain the utility of the minimal model in relation to the complex reality. The likelihood of an interaction more complex than the pairwise one modeled by the entwined helices increases with the curliness (later defined by equation 3.13) of the hairs⁵⁶. However, the closer an entanglement is to the free end, the closer it is to being removed from the hairs. This is captured in the dynamical balance between the jamming-like over-winding of the helices and the detangling loss of link through the free end. Additionally, combing nearer the free ends reduces this many-body complexity concern as pairwise links are removed before neighboring hairs can get more involved.

From this model, there are two key results which inform the development of a brushing controller. Firstly, small pitch and more tightly wound helices lead to larger forces required, thus the curlier the hair, the greater the resultant brushing forces. Secondly, starting combing nearer to the free end allows link to propagate out the free end faster and easier. This allows for untangling before the link density in front of the comb becomes too high and the comb/tine begins to jam. Hence we recover the intuitive result that one should start combing ones hair far from the scalp and gradually work upward. Thus, to detangle hair, the hair should be brushed starting from near the free ends

and working up, optimally removing a given amount of link entanglements with each brush stroke.

Figure 3.2(a) shows an illustration of this model, and the key parameters which define the double helix model. These are P , the length of one entanglement which corresponds to the length of one period of the double helix, R the radius of the curl, r the radius of this hair and l_0 , the length of the hair. From this, a measure of the amount of curl can be given by P/R , and the number of entanglements to remove through brushing is given by P/l . In this work we make the simplifying assumption that r is approximately constant for human hair.

We note that the simulations used in Plumb-Reyes et al. (2021)⁵⁶ can be extended to model the brushing of a many-body tangle of hair. In such a model, each hair would be treated as a Cosserat elastic rod⁵⁰ and each comb tine as a rigid rod, with all tines and hairs interacting via contact forces. A demonstration of how a hair bundle can be modeled numerically is shown in Plumb-Reyes et al. (2021)⁵⁶. We propose applying this simulation scheme to a large bundle of hairs combed by several tines. In such a simulation, we could track over what combing length scale two-body interactions accumulate into many-body interactions and produce more complex tangles in the bundle. These results could further inform the control algorithm to design a combing strategy that maximizes the stroke length of each brushing iteration while avoiding the build-up of two-body interactions into many-body tangles.

PROBLEM DEFINITION

Given this model, we can define the hair brushing problem. This is the removal of entanglements from hair which is hanging free from the top of the head. The hair can be described by the length, l_0 , and we define a curliness ratio as:

$$R_C = R/P \tag{3.1}$$

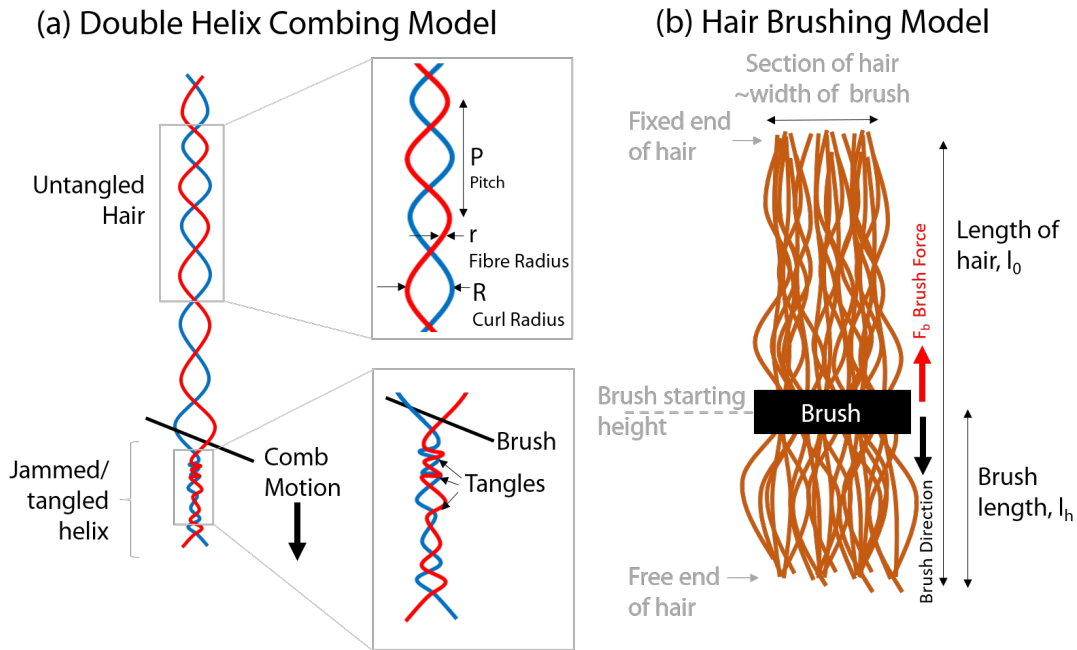


Figure 3.2: (a) Simplified minimal model of a double helix of hair undergoing combing. (b) Model of the hair brushing problem showing the hair brush and the quantities that describe the problem.

such that the number of entanglements in the section of the hair can be given by:

$$q_0 = l_0/P. \tag{3.2}$$

A control approach must be developed to optimize for brushing time, whilst ensuring that the maximum force when brushing (F_{max}) does not exceed the pain threshold F_T . This pain threshold has been identified experimentally by brushing hair with a sensorized hairbrush, and identifying the force at which pain starts to be felt. Using the principles identified by the model, the brushing should start from the free end and work upwards to gradually release entanglements. The length and height of the brushing process should be optimized for a given hair type and length. The brush length, l_b , for a specific iteration of brushing is measured from the bottom of the hair to the height at which the brushing starts. The combing device is kept parallel to the ground and brushed down-

wards. The force during brushing is measured in the direction of brushing.

OPTIMIZATION

The cost of hair brushing has two key components: pain inflicted and time taken. The brushing length (b_l), and hence number of entanglements removed in each brush must optimized with respect to these two costs. The relative costs of these two metrics varies for different amount of curl and entanglements (R_C).

The cost related to pain can be considered to be proportional to the maximum force experienced, and thus is high for longer brushing lengths on curlier hair. In contrast, the cost relating to time is determined by the number of brushing cycles, so longer brush lengths across any hair will minimize this cost. For straight hair with low values of R_C the time cost will dominate, thus longer brushing value should be selected. In contrast, for curlier hair, the pain cost will dominate so shorter brush lengths should be selected. From the model of hair entangling, we know the relationship between force and curliness is not linear, thus we need a more representative way of formulating this optimization problem.

We propose using an adapted Sigmoid function, specifically the Logistic function, to map from curliness (R_C), to the selection of the initial brushing height (b_{l0}). A Sigmoid function offers a monotonically decreasing function in which for low values of curliness we get a large brushing length, whereas for high curliness we get a shorter brushing length. This is illustrated in Figure 3.3. Although other non-linear functions are suitable, this function is particularly suited as a single parameter can be used to capture the rate of change of the ‘S’-shaped properties of the function. Using this function, we can describe the optimal brushing height as a function of R_C using:

$$b_{l0} = \frac{q}{q_{tot}} = \frac{1}{1 + e^{(k(R_c+0.5))}} \quad (3.3)$$

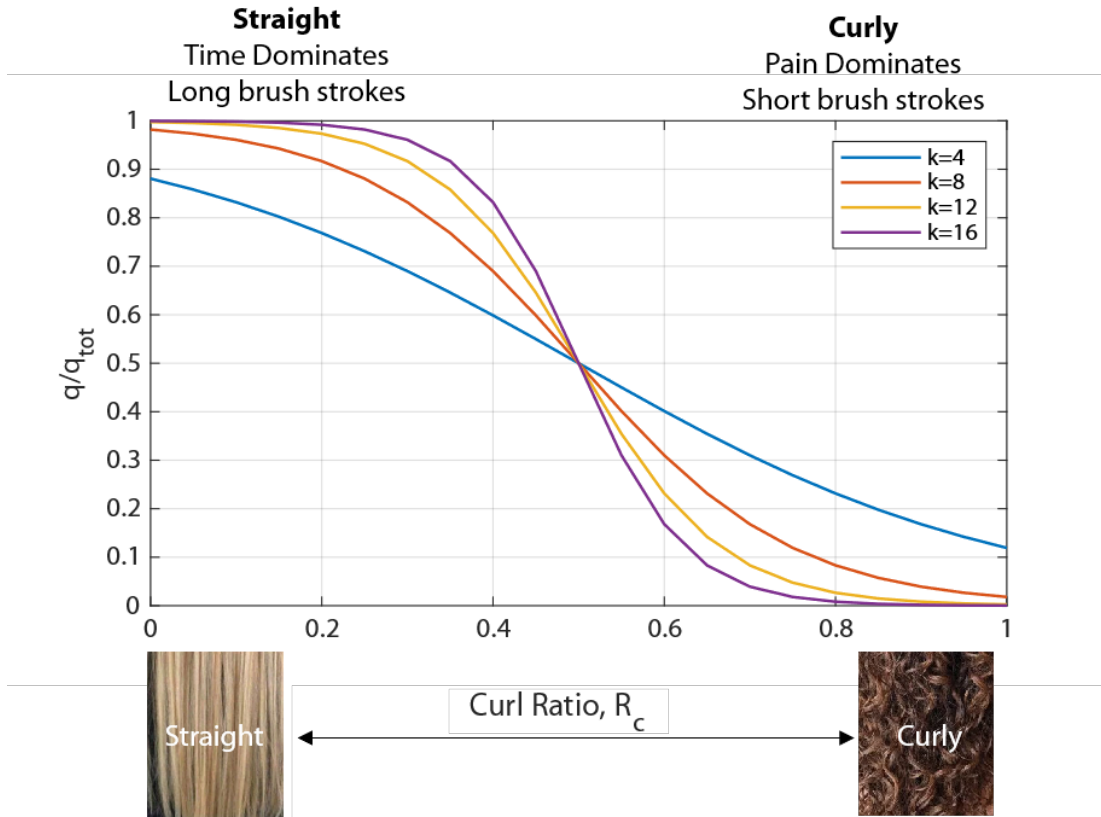


Figure 3.3: Illustration of the optimization problem showing the different regions in which different costs (i.e. pain or time) dominate.

where the value of k should be optimized experimentally by finding the maximum brush length (b_l/l_0) for a hair with a given curl ratio that does not exceed F_T .

CONTROL APPROACH

Using the optimized mapping identified in equation 3.3, an estimation of the initial brushing height can be identified. Although, as a base strategy we can iterate each brush stroke until the full length is brushed. This strategy assumes ideal behavior and that each entanglement is fully removed and the hair behaves as a perfect helix.

Using a closed-loop controller allows for online optimization and customization in response to the specific hair being combed. In particular, if there are especially entangled areas, we can adapt the brushing height to ensure the maximum pain threshold F_T is not exceeded. We propose the following closed-loop controller for iterative brushes which is based upon the optimized brush length identified in equation 3.3. Under this controller, after starting from the height optimized for the specific curl ratio, the following round of brushing is adapted if the force experienced is too high, allowing for repeated brushing at low heights if knots occur, or if entanglements are not brushed out in a single iteration. In addition, the incremental length added can be increased if forces are significantly lower than the maximum threshold.

An additional component of this controller is identifying when the hair section is fully brushed. We define this as when the full length of the hair is being brushed, and there is minimal change in the maximum force between brushing iterations (i). This boolean condition is defined as:

$$finished = \begin{cases} 1, & \text{if } |f_{max, i} - f_{max, i-1}| < 0.4 \ \& \ b_l \geq l_0 \\ 0 & \text{otherwise} \end{cases} \quad (3.4)$$

where the threshold value was found experimentally.

VISION PIPELINE

The control approach relies on having an estimation of the metric that defines the curl of the hair, R_c . To estimate this, an image is taken at a fixed distance away from the head. The image is cropped to include only the hair and is converted to a greyscale image. From the greyscale image the x and y direction image gradients (G_x and G_y) are found using the Sobel gradient operator³⁰. Gradients have been shown to be useful in other texture identification tasks⁶⁹. Images of straighter hair have a far higher component of edges in the x direction, while images that are curlier have a more equal distribution of edges in the x and y plane. This is visually demonstrated in the gradient plots in Fig-

Algorithm 1: Closed-loop brushing control

```
Take picture, compute  $R_c$  (eqn. 3.5),  $b_{l0}$  (eqn. 3.3);
Initialize sensor and arm;
iteration,  $i = 0$ ;
 $b_l[i] = b_{l0}$ ;
while  $finished \neq true$  do
    move to brushing height  $b_l[i]$ ;
    start brushing in -z direction ;
     $f=0$ ;
    while  $brush\ height \leq bottom\ of\ hair$  do
         $f = [f; read\ force]$ ;
        if  $f \geq f_T$  then
            stop brushing, break;
        end
    end
    stop brushing;
     $f_{max} = max(f)$ ;
    if  $f_{max} \geq f_T$  then
         $b_l[i + 1] = b_l[i](F_T/F_{max})$ ;
    else
         $b_l[i + 1] = b_l[i] + b_i - b_i(F_{max}/0.5F_T)$ ;
    end
     $i = i + 1$ ;
end
```

ure 3.4. Thus, by taking the ratio between the sum of these two gradient fields we can calculate a metric that provides a ratio of the ‘straightness’, to the ‘curliness’ of the hair:

$$R_c = abs \left(\frac{\sum G_y}{\sum G_x} \right). \quad (3.5)$$

For straight hair, $\sum G_y$ is very small, and thus the ratio R_c is approximately 0. For curly hair, the $\sum G_y$ starts to become closer to $\sum G_x$, resulting in a ratio closer to 1. By placing an upper bound on R_c of 1, R_c provides an alternate metric for the ratio of P to R .

We demonstrate that these metrics are a reasonable measure of the curliness of hair by computing the ratio R_c , for a number of different images of hair, and plotting them alongside the measured ratio (R/P), which forms the ground truth for this experiment. This results are shown in shown in Figure 3.4.

3.4 EXPERIMENTAL SETUP

To explore the control strategies for hair brushing we have developed an instrumented soft brushing end effector which is mounted on the end of a robot arm. The setup is shown in Figure 3.5. The robot arm allows for a wide variety of trajectories to be performed and provides speed control. The end effector is constructed from a hairbrush which has soft bristles. The brush is mounted on a load cell which is connected to the end effector of the robot arm. This allows the force normal to the load cell to be measured. The signal from the load cell is amplified using an instrumental amplifier and measured with a microcontroller. The load cell has been calibrated, and the readings are converted into Newtons and sent through a serial bus to the control PC at 10Hz. The control policy is implemented, and the hairbrush is mechanically controlled by sending position commands to the robot arm and attached hair brush. A diagram of the system is shown in Figure 3.5.

To test the system and controller, we use a head mount on which various wigs can be attached using hair pins. The head is mounted on a variable height mount such that the bottom of the hair is kept in a fixed location relative to the robot and camera setup. Each wig is set in to a ‘pre-brushed’ state by turning upside down and shaking for 10-15 seconds. This returns the wigs to an entangled state and allows experiments to be repeated with a similar state of entanglement.

The wig is placed such that the free end of the hair is at a fixed point relative to the arm. A webcam is also mounted in a fixed position relative to this position, and is used to capture the image to determine the curl ratio R_c . The brushing height can then be determined, and the brush moved to

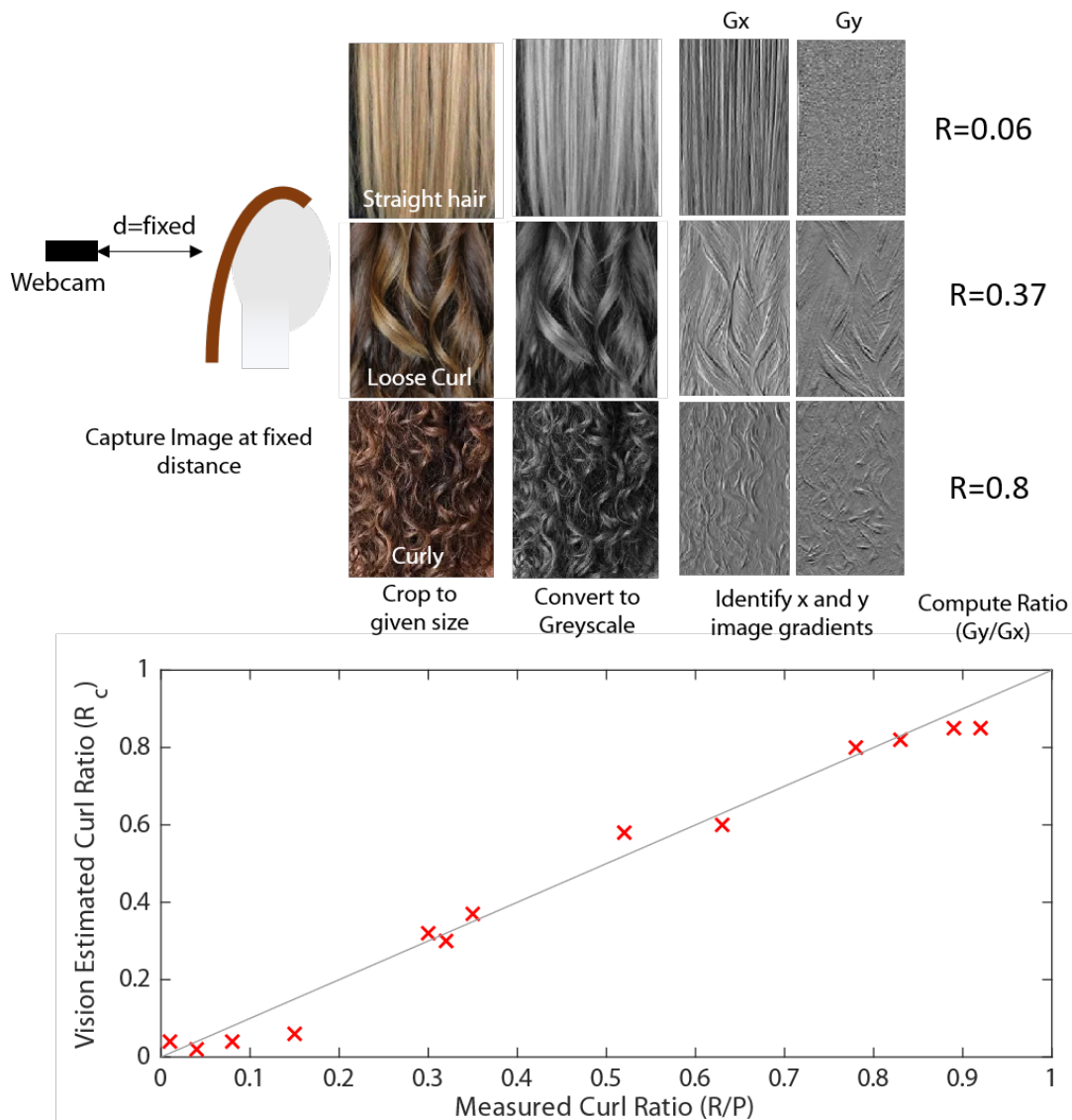


Figure 3.4: (Top) the vision pipeline on example images: cropping, conversion to greyscale, determining gradients and then determining the ratio. (Bottom) figure showing the R_c captured using vision, and the measured (R/P) value.

this height before the brushing regime starts. The brush is moved from the brush height in a fixed plane downwards to below the end of the hair. This is repeated until the robot determines the process is finished. The depth of brushing (horizontal distance between the hair and the brush) is kept

constant for all experiments and was chosen experimentally such that brush bristles interact with both straight hair which has less volume, and also curly hair.

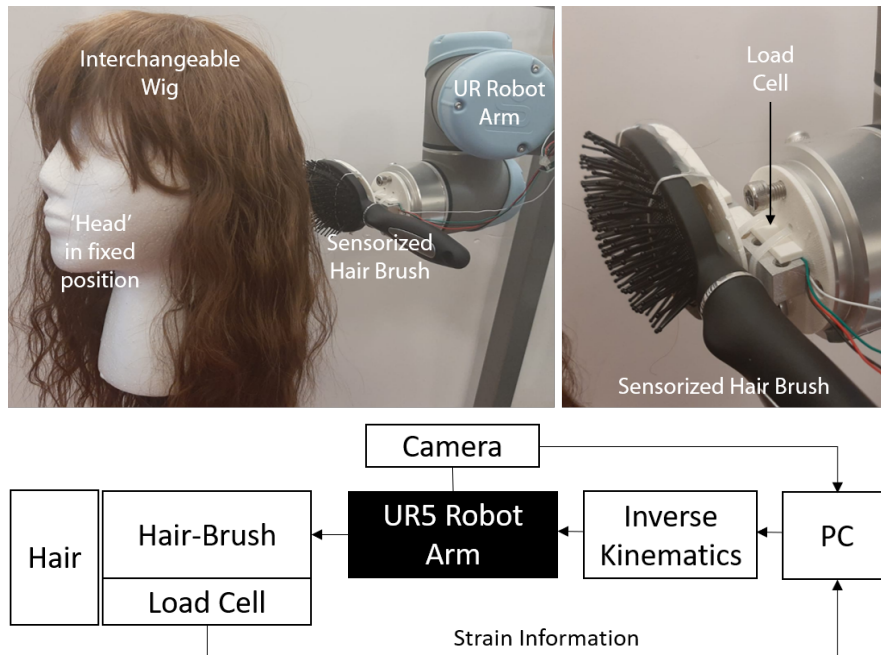


Figure 3.5: (Top) The experimental setup and the sensorized hair brush. (Bottom) Block diagram of the hair brushing system.

3.5 EXPERIMENTAL RESULTS

EXPLORATION OF HAIR BRUSHING

To demonstrate and validate the model, we have performed a set of brushing experiments for which we show the progression of the force with brushing time. First, we show repeated brushing of a single wig with the brushing height fixed. We see the expected rise in force as the hair fibers start to jam, after which the force applied to the brush overcomes this jamming force and brushes free. The brush force is the highest for the first brush, however, and reduces with subsequent iterations as

entanglements are removed. After three brush cycles the maximum forces measured on each brush cycle start to plateau, demonstrating that entanglements and potential jams are being removed. This validates the method of identifying when brushing has finished as given in equation 3.4.

We next perform a similar experiment but where the brushing height is varied. Each height experiment was repeated 5 times, with the hair ‘reset’ between experiments. The average of each set of experiments is shown in Figure 3.6(ii). When brushing the entire length of the hair fibers we measure building force, with the rate increasing as the fibers jam, until the brush finally pulls through these entanglements. When the brush height is reduced, the maximum force reached reduces significantly, and we also see more reliability in the repeated experiments.

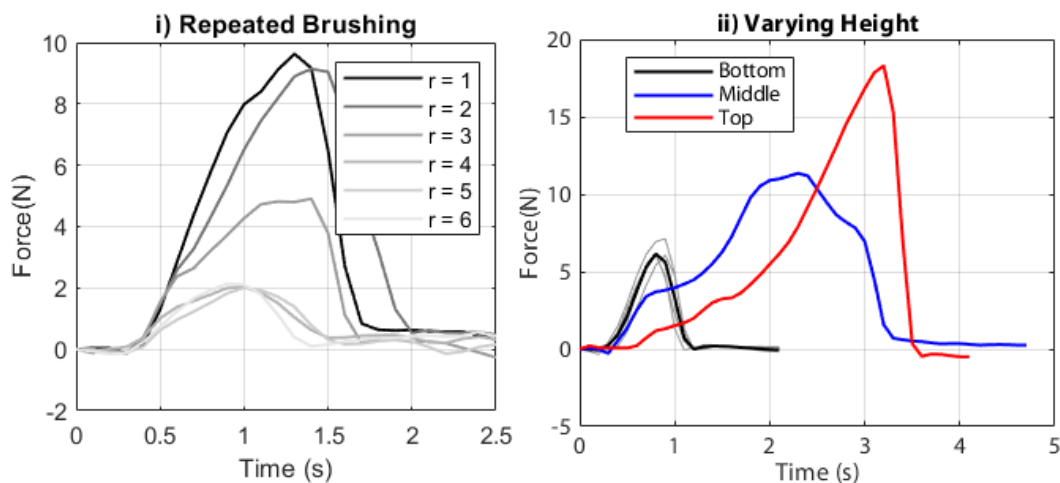


Figure 3.6: Exemplar timeseries from the sensorized hairbrush when brushing (i) the same hair at a repeated high for 6 iterations, (ii) varying the height of brushing.

The model suggests that the velocity of brushing should have a minimal effect on the experienced force. To test this we use the hair brushing platform to explore the variation in force measured for different speeds of brushing. Figure 3.8 shows the variation in maximum brushing force for different brushing speeds. This is performed for the two wigs, one straight and one curly, with the brushing height fixed. The wigs are reset between each test.

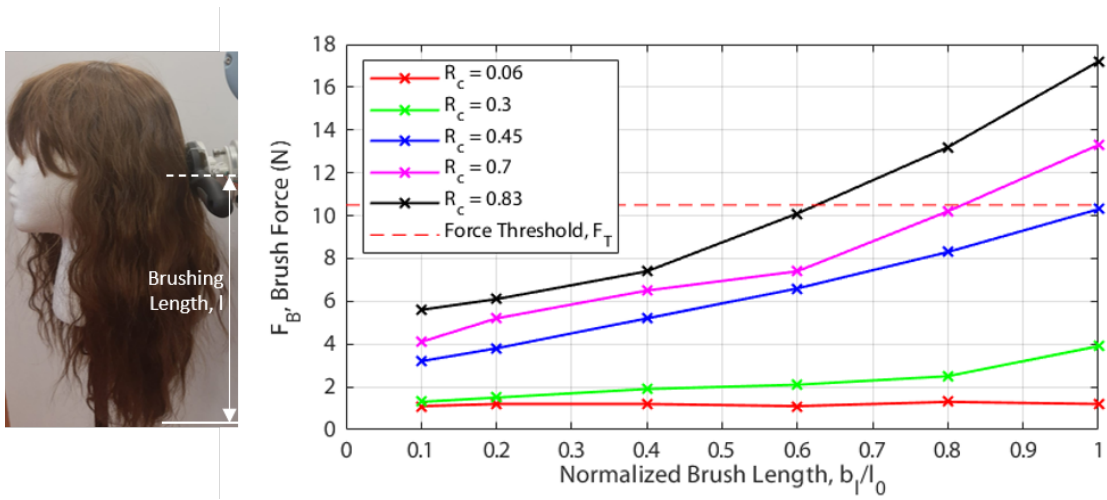


Figure 3.7: Variation in maximum force with normalized brushing length for hair with different curliness.

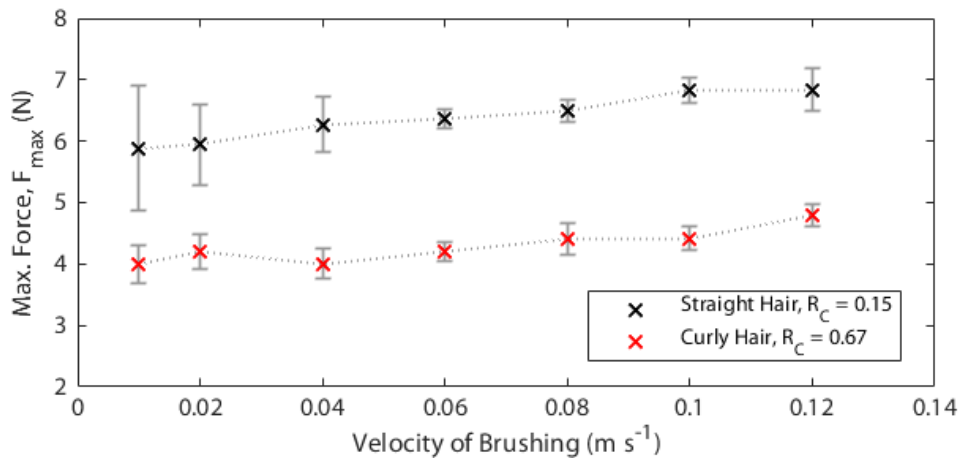


Figure 3.8: Average maximum force for different velocities and orientations of brushing for a fixed brush length, and on the same hair ($R_c = 0.4$).

As expected we see that the velocity has minimal effect on the brushing force, in particular for straight hair. For curly hair, whilst the maximum force is approximately constant, there is far greater uncertainty for slower motion. This suggests that although velocity does not affect the maximum force, a slightly faster speed reduces variability in the forces experienced. The maximum speed of these experiments were limited by the capabilities of the robot arm, and thus it remains relatively

low; further work could explore the effects of faster, jerkier hair brushing motions.

OPTIMIZATION

To optimize the selection of brushing height, we must fit the sigmoid function proposed in equation 3.3 to experimental data. For a number of wigs with different hair types, we identify the maximum normalized brushing length that can be performed without exceeding the brushing force threshold, F_T . We can then fit a sigmoid function to these data points to identify the optimal value of k to ensure efficient brushing without exceeding the maximum force threshold.

The results of this process are shown in Figure 3.9, where the optimal value of k is found to be 8.5. It can be seen that the sigmoid function has been fitted to the points such that the curve is lower than any of the experimental results to ensure that the maximum force threshold is not exceeded at any point. There is close agreement between the experimental results and the sigmoid function, validating this choice of function.

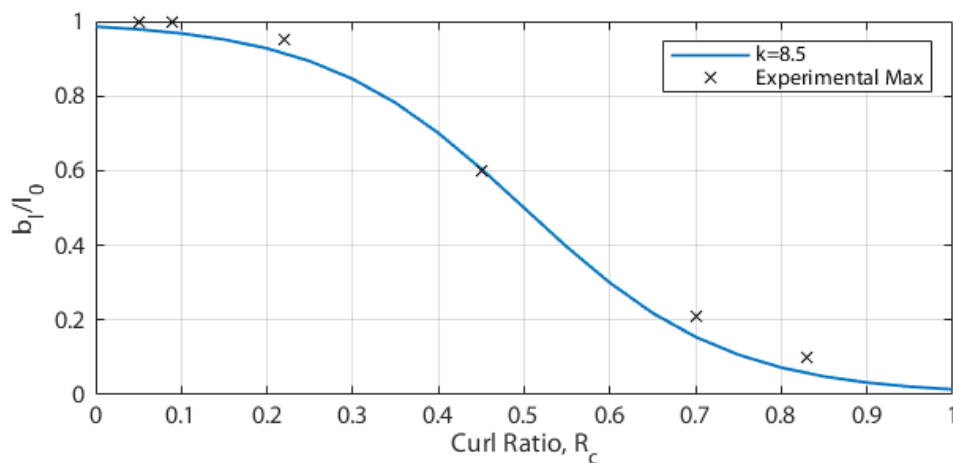


Figure 3.9: Optimized sigmoid function (equation 3.3) to allow identification of the optimal starting brush height for hair with different amounts of curl.

BRUSHING DEMONSTRATION

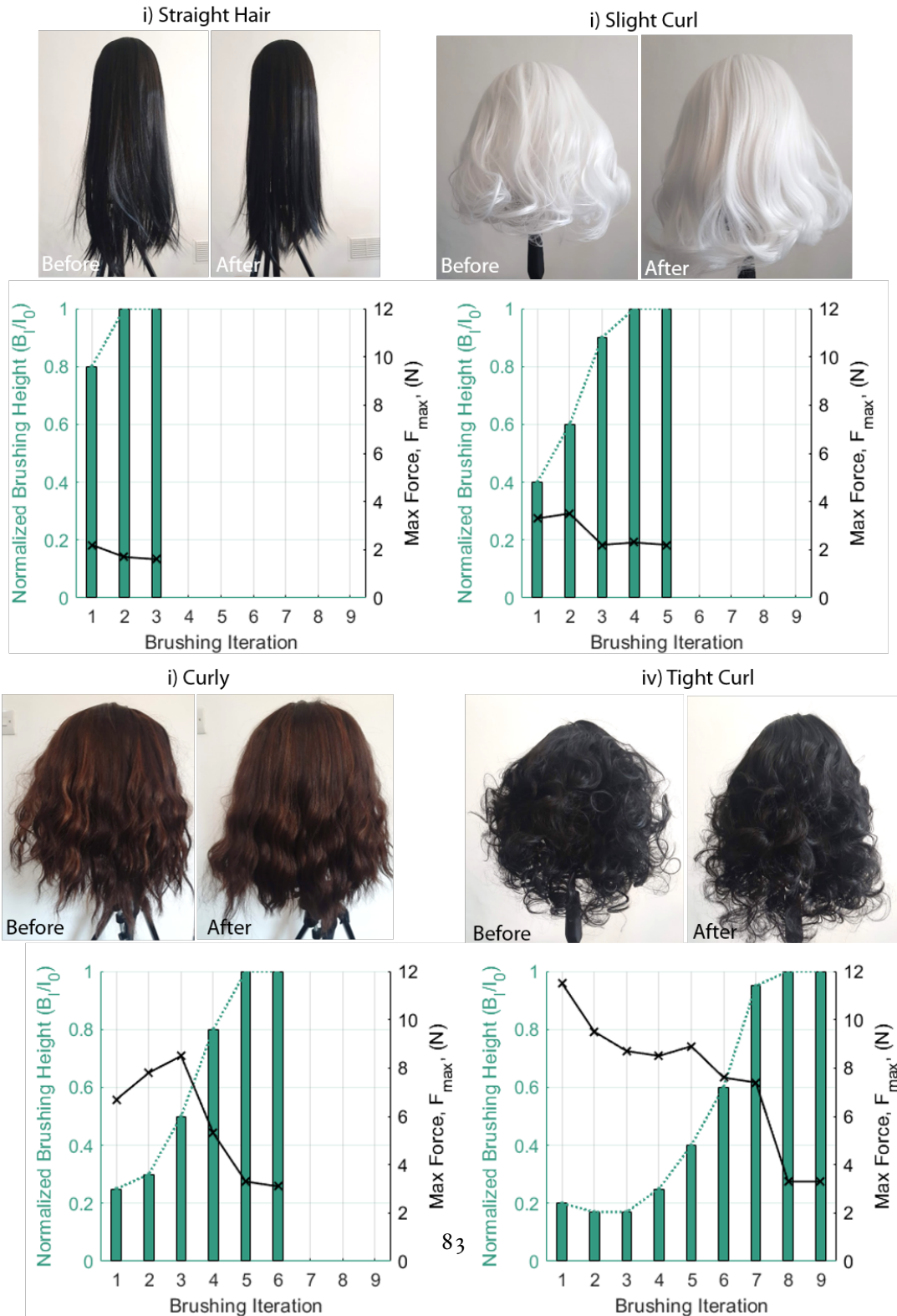
To demonstrate the hair brushing approach, we test the controller on a number of wigs which have been selected to show a variety of different lengths, hair types and curl ratios. We have selected four examples with varying hair type to demonstrate the process. In each of these, we show the iterative brush height that is selected, and the measured maximum force for each of these iterations. This is shown in Figure 3.10 alongside before and after photos of the hair. The visual results of the hair before and after are also shown. We observe that, in the case of straight hair, the approach is simplistic, the estimated ratio performs well and minimal iterations are required. As the amount of curl increases, more brush strokes are required, and the forces increase. Finally, when we move to the curliest hair we see the ratio predicted using vision is initially too high, and thus the brush height must be reduced to remove some of the entanglements that form. In all cases we can see an improvement to the hair after brushing.

To benchmark and contrast the performance of the control approach developed, we compare the performance to a ‘naive’ brushing approach and human brushing. In the ‘naive’ approach we brush at a fixed interval which increases by thirds each time (e.g. $B_l = 0.33, 0.67, 1$). We also compare to a human baseline where the human was asked to brush the section of hair using the sensorized hairbrush. Whilst this human baseline considers only a single person and therefore their specific approach, it can provide an order of magnitude estimate of human performance. All control strategies were repeated on wigs with a variety of curl ratio with the total time to brush, and also the maximum force recorded. This comparison between approaches is shown in Figure 3.11.

When considering the maximum force that is achieved the optimized robot solutions show similar response to that of human brushing, although the human performs marginally better at the extremes. The naive approach leads to significantly higher forces for the curly hair, significantly exceeding the pain threshold ($F_T \approx 10\text{N}$). However, this approach is still faster than the optimized

Figure 3.10 (following page): Demonstration of hair with increasing curliness using the control approach showing the maximum force and normalized brushing length for each iteration.

Figure 3.10: (continued)



solution. Throughout the experiments the human performs faster, however the robot's movement is limited by the capabilities of the robot arm, and thus there is considerable room to optimize this process and close the performance gap.

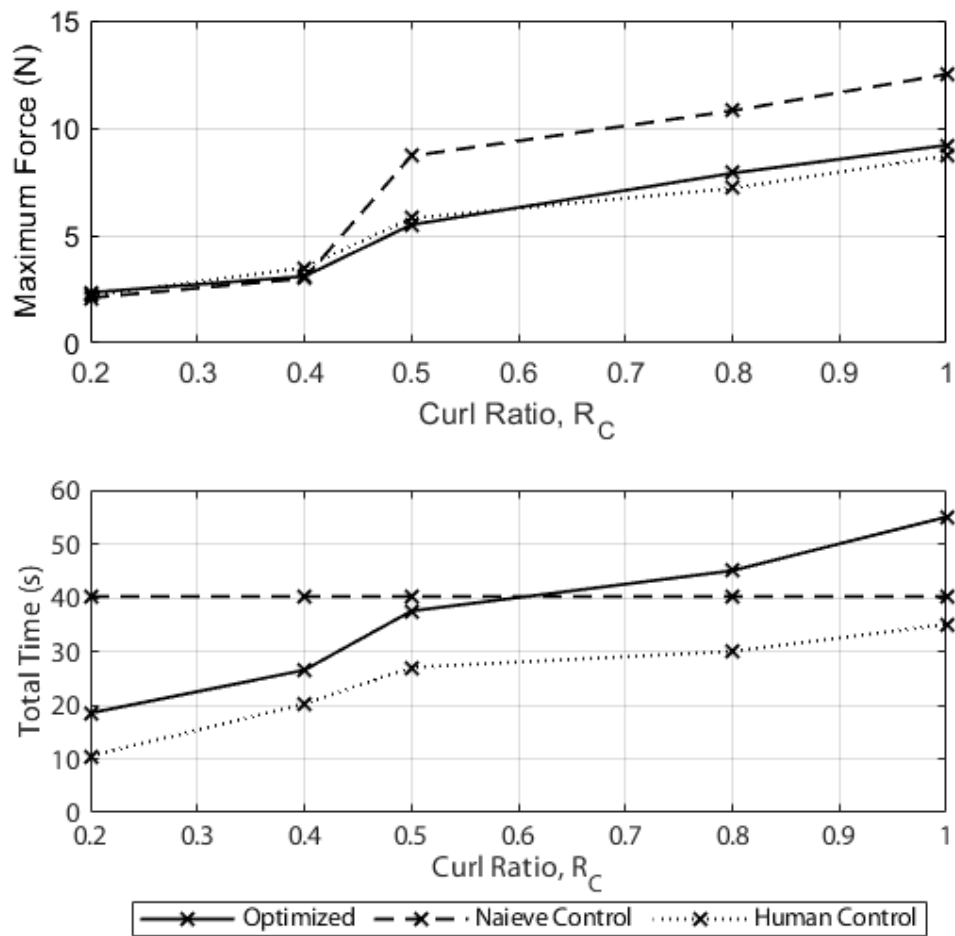


Figure 3.11: Comparison between developed controller, human brushing and also a naive controller for the consideration of maximum force (top) and brushing time (bottom).

3.6 DISCUSSION & CONCLUSION

In this work we introduce an experimental model for the combing of entangled chiral hairs using a visuo-motor feedback loop that builds on recent work to comb a double helix⁵⁶. Our model provides significant insight into the behaviors of the combing of hair with respect to the number of entanglements, and how these can be efficiently and effectively brushed out by choosing appropriate brushing lengths. We propose using a sigmoid function to select brushing height for different hair, where computer vision is used to identify the curliness of hair.

Using this model, we have developed a control approach for brushing hair for various hair types. By developing a sensorized soft brush end effector, we have validated this approach experimentally and benchmarked it in comparison to a human approach and a naive approach. While this work has demonstrated effective hair-brushing, there is significant room for improvement, including investigating more complex combing trajectories and increasing the complexity of our model through many-hair combing simulations. Performing such simulations would allow us to increase the complexity of our algorithm to capture nuances in the differences in the mechanics of combing across different hair types and hair styles.

Another area for future work is performing more realistic experiments on humans, to gain more subjective feedback from the experimental subjects. Pain is a highly complex phenomena, and to truly understand the performance of the robot with respect to this metric, human experiments are required.

One advantage of this approach presented its adaptability, due to the use of a sigmoid function to optimize the starting brush height. This allows the model to be easily adapted when the task is varied by using a different brushing device or a different task, such as brushing wider/complex complex textile-based fibers. By fitting the sigmoid function to a set of minimal experimental data the approach can be readily adapted.

In addition to further exploration of hair brushing, the model of entwined soft hairs could have significant further applications. For example, it could be used to develop robotic approaches to dealing with ropes and other fibrous systems, or even robots that efficiently manipulate spaghetti.

ACKNOWLEDGEMENT

We would like to acknowledge support of the grants and funding that has made this work possible.

*Whenever I mess up an experiment I just think of what a
pigeon considers a successful nest.*

Dr. Nick Chiappini

4

Topology and Mechanics of Entangled Rigid Rods

In this chapter we are interested in studying another system that exhibits an interesting relationship between its mechanics and its topology. Taking a common bird's nest as the inspiration for a biologically-inspired material, we explored how geometric relations between the individual constituents (rods) of the randomly packed network related to its material response to stress. This involved connecting the macroscopic story (mechanical stress-strain behavior) with the internal one (areas of entanglement between groups of rods). This connection presents potential insights into how to optimize the design and preparation of randomly packed entangled materials. This work was completed with L. Mahadevan, Yeonsu Jung, Elodie Couttenier, Hunter S. King, and Hao-Yu Greg Lin.

4.1 ABSTRACT

We examine the mechanical response and geometric configuration of randomly packed thin steel rods as a biologically-inspired material analogue of a bird's nest. We find that the rod networks exhibit clear plastic deformation and aging across the small-strain regime ($\varepsilon < 0.15$). We use X-ray CT to reconstruct 3-D images of the rod networks before and after compression. We define and calculate an entanglement field $e(X, Y, Z)$ over intermediate length scales within the network. We also calculate the volume fraction and orientational order parameter. We relate the macroscopic compressive stress response to changes in the internal configurations of groups of rods. These geometric and topological tools can be used to characterize many material systems in which physical entanglement is an important characteristic, such as cotton or wool fibers and fiber-reinforced concrete.

4.2 INTRODUCTION

Gather a pile of sticks off the forest floor and shake or drop them, and they will struggle to hold any cohesive shape or structure. A bird's nest of the types shown in Fig. 3.1, however, is carefully constructed to hold its shape and provide shelter for the bird and its offspring. A single bird's nest can be made from many different types and shapes of materials (i.e., twigs, leaves, grass, spider silk, plastic bags, etc), including mud or saliva to strengthen cohesion.⁹ To specifically study the role of physical entanglement, we will consider a minimal model for a nest: a randomly packed volume of thin, rigid rods. This minimal model will allow us to isolate one important facet of a nest or nest-like material: how the physical entanglement of groups of rods plays a role in the material cohesion and mechanical response of the bulk material. The phenomenon of randomly packed objects forming a solid-like state is called jamming.⁴³ The formation of these jammed states is an ongoing area of study in condensed matter physics.⁴⁹⁻⁸⁰ Macroscopic cohesion and mechanical response for these types of systems has been studied for various particle shapes like staples or stars.²⁹⁻⁸⁵ We will treat the

jammed state as the starting point for analyzing how shifts in the configurations of groups of rods on the intermediate scale relate to the macroscopic stress-strain relationship of the conglomerate.

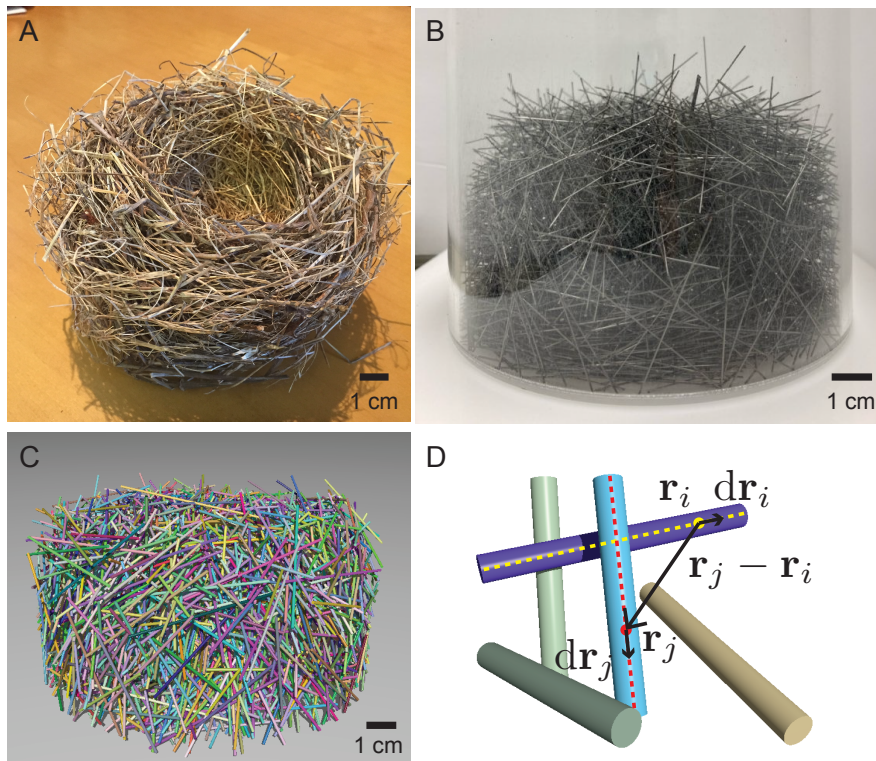


Figure 4.1: Bird's nest and the model system for the present study. (a) Bird's nest. (b) An entangled pile of steel rods in an acrylic container. The rods in the container were shaken so that they were randomly oriented. (c) 3-D reconstruction of each rod from X-ray CT scans. (d) Example rod configuration in a local subdomain. Centerline coordinates were obtained from a custom image segmentation method (see SI for more details).

4.3 RESULTS

4.3.1 MECHANICAL DEFORMATION

We know bulk properties of the rod network are related to the geometry of the constituent parts (e.g., average contact number and stress value for a given strain). More interesting features can be observed by looking at the shape of the stress-strain curves for a given rod geometry. These features

imply that the configurations of the rods with respect to each other (and the way these configurations change under stress) is an important factor in the network's material response. In other words, the networks made of these stiff steel rods do not simply behave as an extension of their individual material properties, but rather as a system driven by the internal interactions between groups of rods.

Do these jammed rod networks behave like an elastic material in any strain regime? As seen in Fig. 4.2(b and c), even for very low applied tensile and compressive strains, the networks show clear hysteresis and non-linearity in their stress-strain curves. This implies that plastic deformations play an important role alongside any elastic response from bending, even in the very low strain regime. Irreversible configuration changes between rods in response to deformation could give rise to this behavior. To test whether dissipation factors in to this behavior, the strain rate was also varied. Even so, no significant difference in the hysteresis was observed (see Fig. 4.2(b)).

The elasto-plasticity of the rod network was further examined by testing the memory of the system. Aging in the network is shown in Fig. 4.2(d), where a single rod network undergoes an initial larger stress softening, before the softening decreases more steadily in subsequent equal deformations. This implies the network is damaged (equivalently, the rods are reconfigured) through repeated loading. This general behavior is similar to that observed in rubber [21, 67, 10] and crumpled sheets [3], where logarithmically decreasing trends in softening rate over repeated cycles are observed (see Fig. 4.2(d) inset).

Stress softening behavior and clear elasto-plastic stress-strain response could imply that changing rod configurations and interactions are an important driver of the mechanical response of the rod networks. It is therefore important to analyze and characterize the internal geometry of the system. However, because the internal geometry of the rods is extremely complex and will vary with every randomly packed network of rods assembled, it is useful to choose a metric that is invariant to the specific positions of every rod, while still capturing the importance of their relative entanglements.

The linking number, a topological invariant that characterizes the entanglement of two closed space curves, can be adapted to these randomly packed rod networks to give a quantitative upper bound on the entanglement of groups of straight rods. This entanglement field is an adaption of Gauss's linking integral and is defined as

$$e(X, Y, Z) = \frac{1}{4\pi} \int \int \frac{(\mathbf{dr}_i \times \mathbf{dr}_j) \cdot (\mathbf{r}_i - \mathbf{r}_j)}{|\mathbf{r}_i - \mathbf{r}_j|^3} \quad (4.1)$$

where \mathbf{r}_i and \mathbf{r}_j are the positions along the centerline of each rod and the domain (X, Y, Z) of the integral is a chosen sub-volume of the entire entangled rod network. For a single pair of rods, Eq. 4.1 will be minimized when the two rods are parallel, and/or the rods are far apart from each other. In this way, the entanglement field can give a quantitative upper bound on its namesake. The actual value of this integral corresponds to Average Crossing Number (ACN) which is defined as the number of crossings of a curve via every viewing angle on the rod network¹¹. It is still elusive whether ACN as an entanglement parameter can effectively capture how much rods are entangled, outside of extreme examples. For instance, the entanglement map of a group of highly and regularly interwoven rods (such as a 3-D textile) will have a greater value and hold together more cohesively than an equivalent number of rods all packed in the same orientation (like a bundle of firewood). However, observing how the distribution of ACN changes (both numerically and spatially) between the neutral and deformed states of the rod networks can still shed light on the role of local entanglement in determining the bulk mechanical properties. This topological measurement can be generally applicable to various filamentary objects regardless of disorder, thickness, flexibility, and closed-ness of curves.¹¹

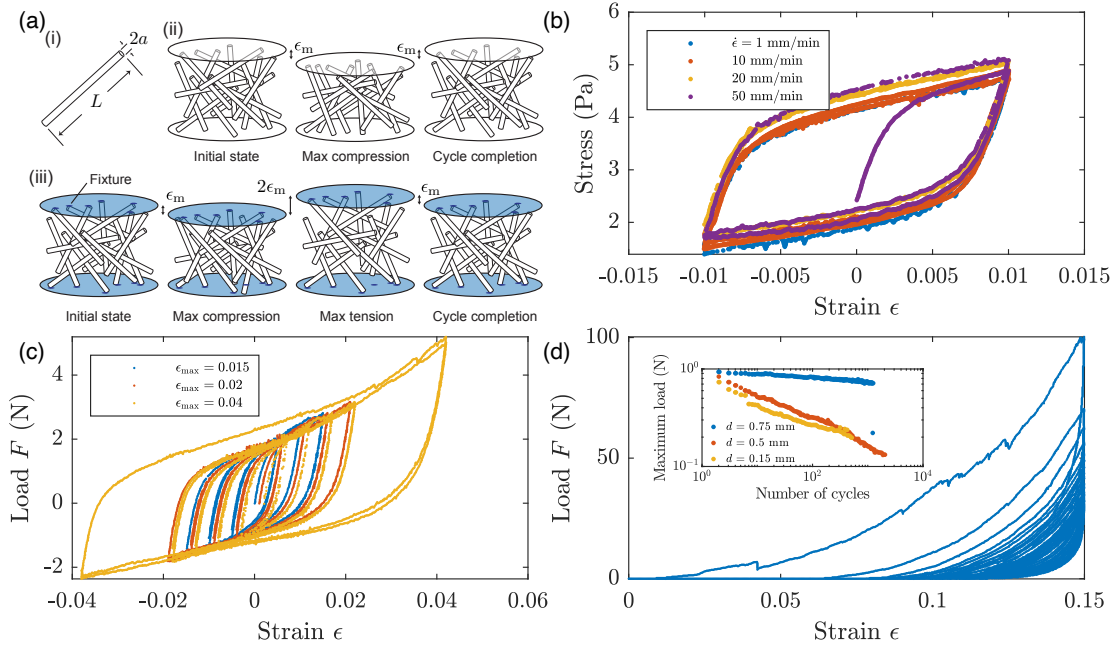


Figure 4.2: Mechanical testing of rod networks. (a) (i) Rod dimensions (ii) Compressive strain cycle (iii) Compressive-tensile strain cycle. (b) Load (N) measured by the INSTRON in a compressive-tensile strain cycle $\epsilon = \pm 0.04$. Measurements done with a rod network made of $d = 0.25$ mm rods. To apply a pulling force, rods in contact with top and bottom plates were fixed with epoxy. The attached rods were kept connected with top and bottom plates while the cycle was running (see (iii)). (c) Load (N) measured by the INSTRON in a compressive-tensile strain cycle $\epsilon = \pm 0.01$ for different rates of applied strain between 1 mm/min and 50 mm/min with three different $\epsilon_{\max} = 0.015, 0.02$, and 0.04. ϵ_{\max} means the maximum strain that each compressive-tensile strain cycle attains. Measurements done with a rod network made of $d = 0.25$ mm rods. (e) Load (N) measured by the Instron for repeated compressive cycles up to strain $\epsilon = 0.15$ (See (ii)). Measurements done with a rod network made of $d = 0.25$ mm rods. Inset shows maximum load (N) measured by INSTRON over repeated compressive cycles up to strain $\epsilon = 0.15$ for rod networks of different diameters.

4.3.2 EXPLORING THE CONFIGURATION OF A ROD NETWORK

X-ray tomographic images allowed us to observe configuration parameters in a entangled rod network. From a stack of x-ray cross-sectional images, we obtained centerlines of every rod in a rod network so that useful information could be obtained. The typical number of rods in a container of 150 mm diameter is 3,000 for these experiments. The typical height of the rod network is 100 mm so that the typical number density of rod networks presented in the study is 10^{-3} mm^{-3} . This is slightly above the concentrated regime ($n \approx 1/aL^2$) of a solution of rod-like chains²². This implies

that the rod networks are highly entangled with isotropic orientational distribution. While the real orientational distribution from X-ray images tends to be slightly oriented in the horizontal direction most probably due to gravity, it is sufficient to assume isotropic orientation of rods (see SI).

The hallmark of entangled rod networks is the highly restricted motion of each rod despite the low volume fraction of rods, $\varphi_c \approx 0.01$. As shown in Fig. 4.1(d), the motion along a rod is almost free, while the motion perpendicular to the polymer is restricted by neighboring rods. The average distance that the rod can move perpendicular to its longitudinal axis, the tube radius²², is given by $b = 1/nL^2 \approx 1$ mm. In the concentrated regime, $n \approx 1/aL^2$, it is trivial that the tube radius is close to the rod diameter. Thus, the sliding of rods along its axis is the principal mode of movement in the entangled rod network.

The number of contacts per rod, c , can also confirm the restricted motion of each rod (see SI). The average number of contacts per rod, $\langle c \rangle$, measured $\langle c \rangle \approx 5$ from these experiments, agrees with the prediction (with $\varphi \approx 0.01$) in Philipse (1996)⁵⁵ under the assumption of isotropic orientation. This tells us that each rod on average is in contact with around five different rods, which severely limits perpendicular motions (translation and rotation).

4.3.3 OBSERVATION IN LOCAL STATISTICS AND CORRELATION

Observation in an intermediate scale, whose characteristic dimension is larger than rod diameter but is smaller than rod length, allows for better understanding of disorder in a network of rods. Because the entire domain is in the same order of magnitude as the rod length, observation at the rod length scale might not be able to resolve fine structural characteristics. Taking a closer look at how rods are in contact with each other above the rod diameter scale, we could investigate geometric and topological properties associated with contacts between rods.

We define a cube-shaped neighborhood $\Omega(\mathbf{r}; l_s)$ with side length of l_s , that is, $\Omega(\mathbf{r}; l_s) = \{\mathbf{r}' \mid \|\mathbf{r}' - \mathbf{r}\|_\infty < l_s\}$. Local properties defined in this scale fluctuate with finite spatial correlation. Even local

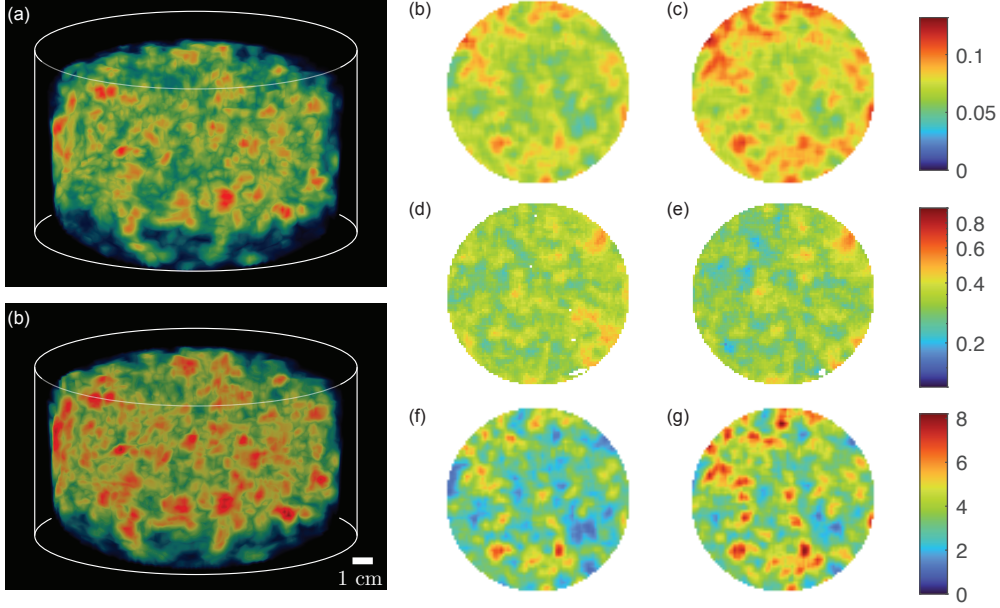


Figure 4.3: Visualization of volume fraction, orientational order parameter, and entanglement. Maximum intensity projection of volume fraction in the initial (a) and deformed states ($\varepsilon = 0.15$) (b) shows local volume fractions increases due to the compression. 2D visualization of depth-averaged volume fraction (b and c), orientational order parameter (d and e), and entanglement field (f and g) shows how each local quantity respond to the compression (c,e, and g) from the initial state (b,d, and f). Depth-averaged quantity was calculated by $\bar{*}(x, y) = \int_0^H *(x, y, z) dz$ where $*$ can be φ , S , and e .

volume fraction in the rod network, $\varphi(\mathbf{r}) = V_{\text{rods}}(\mathbf{r})/l_s^3$ with $V_{\text{rods}}(\mathbf{r})$ being the total volume of rods in $\Omega(\mathbf{r}; l_s)$ fluctuates significantly as shown in Fig. 4.3.

Orientalional order parameter in Ω , $S(\mathbf{r}) = \frac{1}{2} \langle 3 \cos^2(\theta_i) - 1 \rangle$, with θ being the angle between the i th rod and the average angle of every rod in Ω , also fluctuates but in a different manner than the volume fraction. Likewise, entanglement as defined in Eq. 4.1 fluctuates over the subdomains. Volume fraction, entanglement field, and orientational order defined in $\Omega(\mathbf{r}; l_s)$ are local quantities that fluctuate with finite spatial correlation and they provide spatial information on what regions of the network are more or less crowded, randomly oriented, and entangled, respectively.

4.3.4 PERTURBED DISORDER DUE TO COMPRESSION

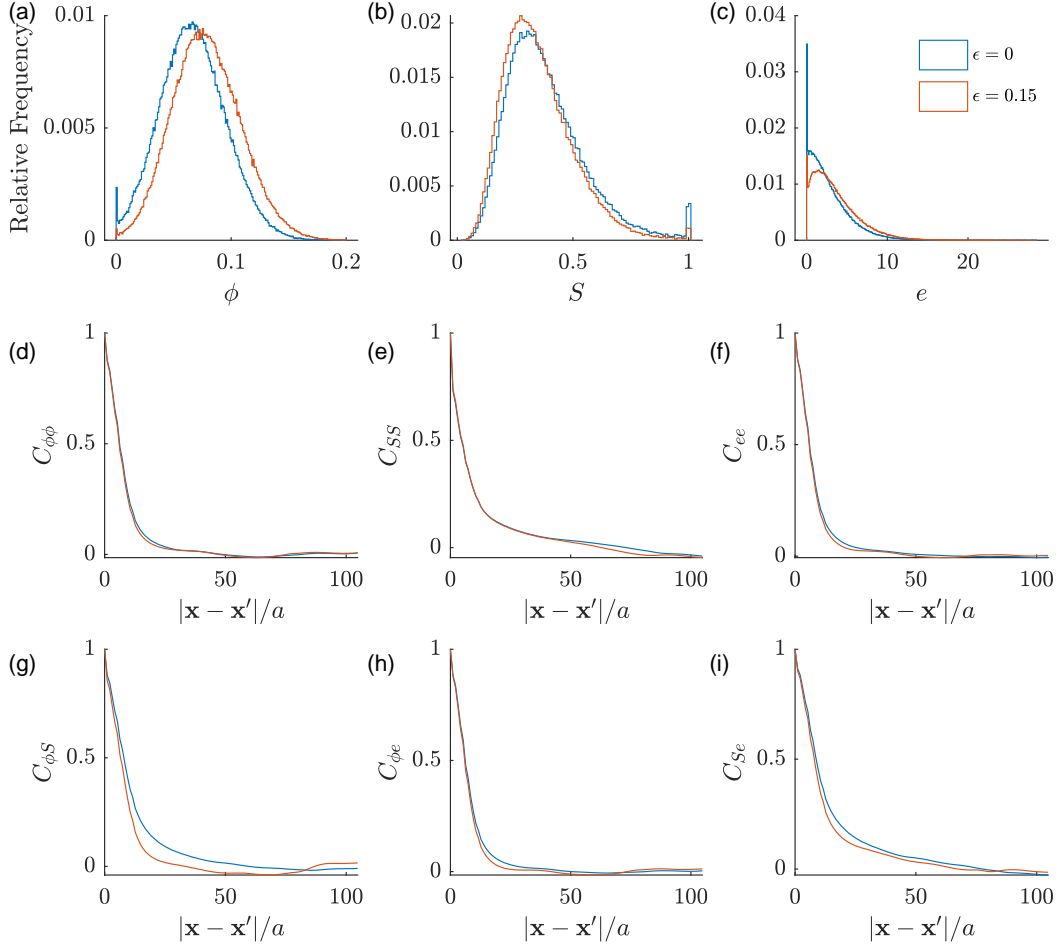


Figure 4.4: Perturbed disorder in volume fraction, orientational order parameter, and entanglement due to the compression ($\epsilon = 0.15$) from the initial state ($\epsilon = 0$). Histograms of volume fraction (a), orientational order parameter (b), and entanglement (c) in $\Omega(\mathbf{x}, l_s)$ with $l_s = 10a$ for the rod aspect ratio of 76 ($a = 0.66$ mm and $l = 50$ mm). Less occupied regions in the rod network becomes more occupied due to the compression, as shown in the shift of histograms (a-c) and reduced population peaks at the unoccupied regions (regions having $\phi = 0$). Note that S is shifted toward zero with the reduced peak at $S = 1$, meaning that rods slid to less occupied regions with high orientational disorder. Spatial auto-correlations of ϕ (d), S (e), and e (f) and cross-correlations of ϕ (g), S (h), and e (i). Correlation C_{AB} is defined in Eq. (4.2) where A and B can be any combination among ϕ , S , and e . To obtain numerical values for C_{AB} , we calculated numerical correlation coefficients $R(i, j, k) = \sum_p \sum_q \sum_r A(p, q)B(p + i, q + j, r + k)/(N - ijk)$ with N the number of 3D grid points and spherically averaged $R(i, j, k)$.

The fluctuations in local variables are shown in Fig. 4.3. In the initial state, there are numerous positions where the volume fraction is null (where orientational order would be unity) and entanglement would be null. These sparse or unoccupied regions become occupied when the rod network is compressed. As shown in Fig. 4.4(a-c), the fraction of unoccupied regions is reduced for $\varepsilon = 0.15$. The local volume fraction itself can be viewed as the degree to which the local domain is occupied by rods. As such, compressive strain causes the histogram of volume fraction to shift in the right-hand direction. We can expect that more occupied regions will usually have lower S and higher e , from the fact that the rods are randomly oriented.

Spatial correlation function between A and B is defined as

$$C_{AB} = \langle (A(\mathbf{x}) - \langle A \rangle)(B(\mathbf{x}') - \langle B \rangle) \rangle \quad (4.2)$$

where $\langle \cdot \rangle$ denotes the ensemble average over local subdomains. Auto-correlation and cross-correlation correspond to the cases where $A = B$ and $A \neq B$, respectively. As shown in Fig. 4.4(d-i), auto- and cross-correlations of local quantities decrease exponentially in general with different correlation lengths. This exponential decay in correlations implies that the locations of highly occupied regions occurs randomly. Typical correlation lengths of all correlation curves (d-i) is on the order of l_s , meaning that these local quantities are in fact highly uncorrelated (between themselves and between each other). It can be hypothesized that contact events in a network of rods occur locally and do not propagate spatially. Compression likely reduces the correlation lengths because of the reduced height of the entire domain.

4.4 DISCUSSION

The results of our mechanical testing of the entangled rigid rod networks showed that the stress-strain response was a combination of elastic and plastic deformations. In order to connect these

observations to the many-body internal interactions inherent in the network, we reconstructed a 3-D image of the rods from X-ray CT scans. We computed the coarse-grained internal feature of rod contact number and found evidence that rods moving via relative sliding motion was the principal plastic deformation mode. We also analyzed finer internal features to get a fuller picture of how plastic deformation occurred in the network. We found that average volume fraction ϕ increased overall under compression and that the tail of the volume fraction distribution extended as previously sparse or unoccupied areas were filled in with rods. Orientational order decreased for similar reasons to volume fraction; initially sparse or unoccupied regions in the network with higher orientational order were replaced by groups of disordered rods. We saw a shift in entanglement field values through a large decrease in areas with initially low or zero entanglement and a shift to the right end of the field distribution. This implied that compression principally recruited new areas of entanglement within the network. These observations can explain how the entangled rod networks respond to compressive strain on multiple length scales and can inform the design of entangled materials with specific mechanical, geometric and topological properties.

4.5 MATERIALS AND METHODS

4.5.1 SAMPLE PREPARATION

This work focuses on the random packing of high aspect ratio (α between 33 and 333) objects to form a complex network that can be studied for its bulk and internal structural properties. For this experiment, the constituent parts of the randomly packed networks were made by cutting stainless steel rods of varying diameters (d between 0.15 and 0.76 mm) to a uniform length $l = 50.5 \pm 1.6$ mm. The rods (a single diameter value per network) were dropped steadily and in small numbers—so as to avoid adding any pre-entangled groups—into a cylindrical container with a diameter three times the length of a single rod. This larger size minimized the undue influence of the container it-

self on the final orientation of the rods. In test runs while designing the experiment, we observed that as the container diameter approached the length of a single rod, the orientation of the rod network was strongly vertical. For the purely mechanical stress measurements, rods were added until the network reached a height $h \approx 110$ mm. For the analysis of stress and internal geometry and topology, the rods were added to a height of $h \approx 80$ mm. During the network preparation, the container was jostled by a motor and inverted by hand several times to excite the rods and reach a predicted steady-state packing fraction φ_f determined by the rod aspect ratio ($\varphi_f \alpha \approx \text{constant}$, see SI).⁵⁵ Both network heights of 110 mm and 80 mm showed similar final packing fractions and uniformity. Overall, we observed that the final configurations of rods were not very sensitive to the specifics of the preparation procedure (in terms of speed or strength of the jostling and rod addition rate).

4.5.2 MECHANICAL TESTING

The physical properties of the rod networks were tested using an INSTRON universal testing machine to study their compressive and tensile response. To test compression, a load was applied vertically downward on the still-contained rod network to focus on the vertical response. To study tension, a petri dish containing a few millimeters of epoxy resin was added to the bottom of the container before the rods were added and randomly packed. After curing, another dish was placed on top, and the network was flipped to secure both surfaces. The lower surface was fixed while the upper surface was attached to the load cell of the INSTRON, which pulled the top petri dish upward, applying tensile stress to the network. Mechanical testing focused on the low strain regime ($\varepsilon \leq 0.15$) to try to study any elastic response.

To analyze the internal structure, rod networks were prepared using the same procedure for mechanical testing but using fewer rods (thereby achieving lower network height) to cut back on computational time and cost. The rod packing fraction φ_f was kept consistent across network heights of

$\approx 110\text{mm}$ and $\approx 80\text{mm}$. The unloaded rod networks were scanned using x-ray computed tomography and a full 3-D image of the network was reconstructed. Then, after putting the rod networks under compressive strains $\varepsilon = 0 - 0.15$, they were imaged again in order to quantitatively compare the data sets and to analyze the relationship between internal structure and stress response.

4.5.3 IMAGE ANALYSIS

The x-ray tomography images were first filtered and binarized to split foreground (rods) and background (void) images. The binarized images were processed with the Euclidean distance transform to obtain the catchment basins for the watershed algorithm. The watershed algorithm based on the distance transformed basin usually brings about oversegmentation and inappropriate segmentation near close contacts. For reliable segmentation of close contacts among rods, we skeletonized the watershed-segmented image, located branch points of the resulting skeleton, and removed the branch points from the image. The remaining skeleton image only contains the line segments to be merged. To merge the line segments, we developed a custom algorithm to determine which line segments were originally connected, based on geometric variables such as distance and angle (see SI for further details).

4.6 SUPPLEMENTAL INFORMATION

VOLUME FRACTION AS A FUNCTION OF ASPECT RATIO

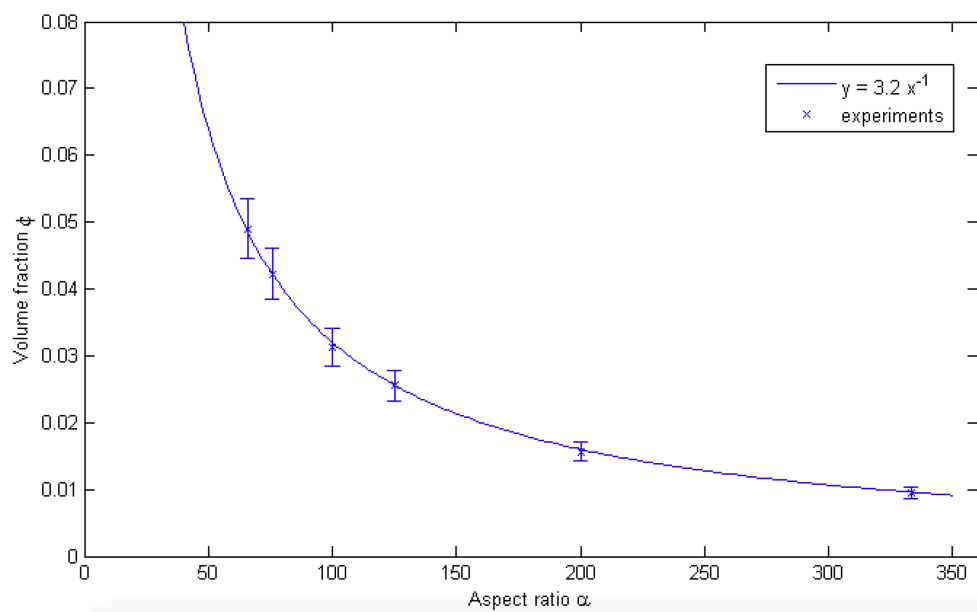


Figure 4.5: Volume fraction of randomly packed entangled rigid rods as a function of individual rod aspect ratio. Curved fitted to $\alpha = 3.2$. Results are in agreement with model in Philipse et al. (1996).⁵⁵

CYCLIC SOFTENING

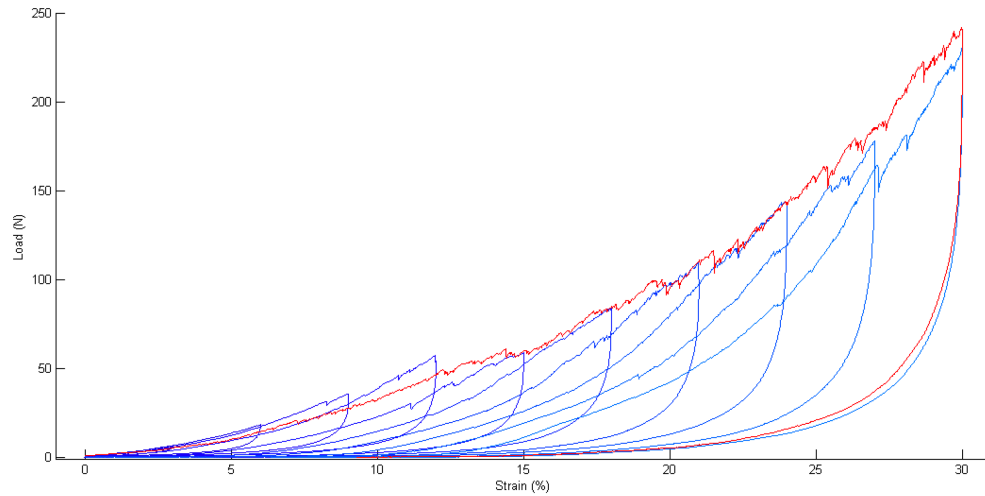


Figure 4.6: Cyclic uniaxial compressive straining of a rod network starting at $\varepsilon = 0.06$ and increasing by $\Delta\varepsilon = 0.03$ each cycle until $\varepsilon = 0.30$ maximum strain (blue curves) compared to a single (non-cycled) deformation to $\varepsilon = 0.30$ (red curve). Softening behavior similar to that of the Mullins effect in rubber is observed.²¹

ORIENTATIONAL ORDER DISTRIBUTION

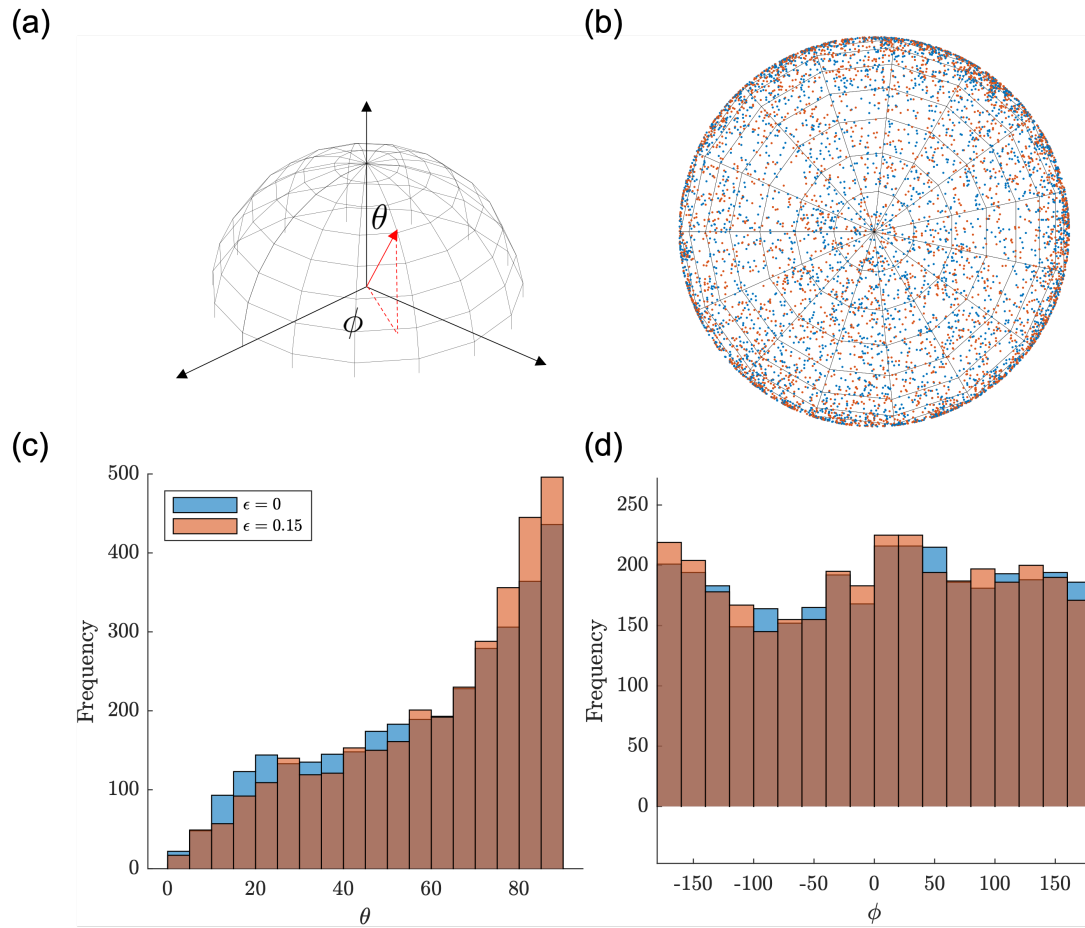


Figure 4.7: Orientational distribution of an entangled network of rods with $d = 0.76$ mm and $L = 50$ mm. (a) Definitions of polar angle θ and azimuthal angle ϕ of a rod axis. (b) Distribution of orientations as points over an unit hemisphere. (c) Distribution of polar angle. Compression makes rods horizontally oriented. (d) Distribution of azimuthal angle. Unlike polar angle, azimuthal orientational distribution was rarely affected by compression.

ROD CONTACT NUMBER DISTRIBUTION

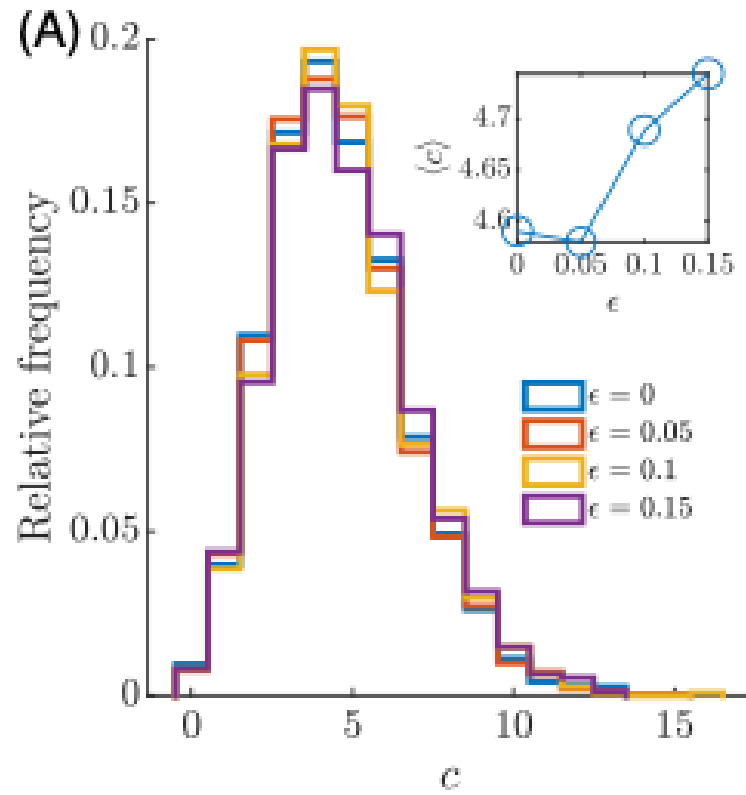


Figure 4.8: Rod contact number distribution of an entangled network of rods with $d = 0.76$ mm and $L = 50$ mm. Only negligible shifts in the distribution of and average (inset) contact numbers are observed before and after applied compressive strain.

ROD SEGMENTATION PROCEDURE

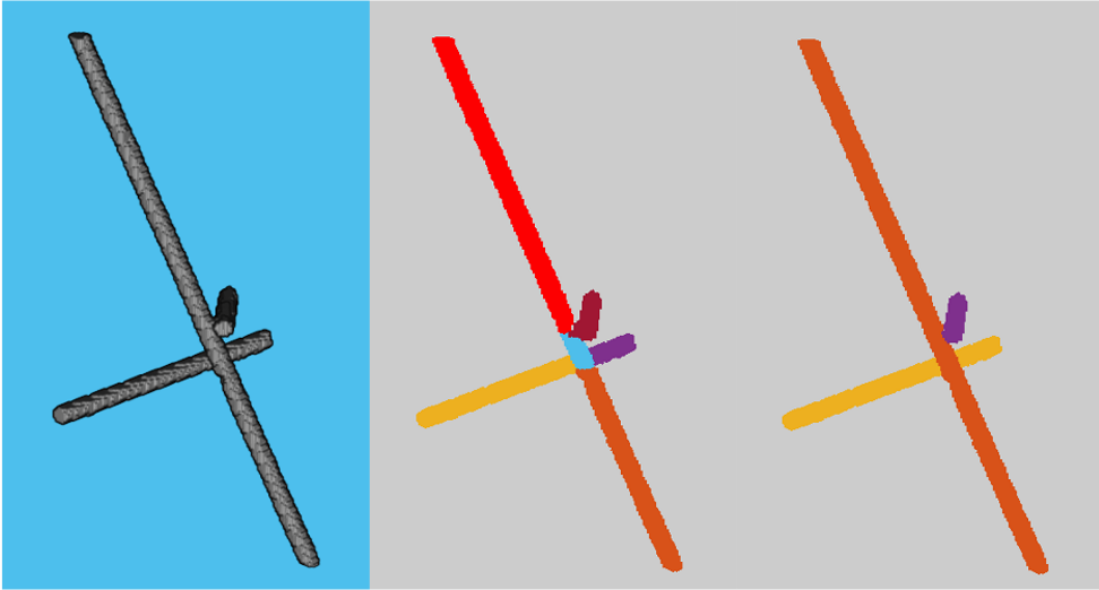


Figure 4.9: (Left) Even after watershed transform, there were still connected rods in the stack. (Center) After the branch removal, we could separate rods, but we obtained over-segmented components. (Right) By carefully checking angles and distance between components, over-segmented rods were merged into a single rod.

We present a walk-through of how we reconstructed a 3-D image of each individual rod in the randomly packed rods X-ray CT imaging data. The whole image processing procedure was done by MATLAB scripts using MATLAB functions and some custom-written functions and classes. When we denote a MATLAB built-in function below, we use ‘function name’ format.

PRE-PROCESSING

We read the X-ray tomographic images read and cropped them to size. Typically, the stack of x-ray images contains about $500 \times 500 \times 500$ voxels. We reduced noise in the stack by edge-preserving anisotropic diffusion filtering (`imdifusefilt`). We were then able to identify the background (air) and foreground (rods) in the voxels by global thresholding with an optimal value.

WATERSHED SEGMENTATION

To obtain catchment basins, we applied 3-D distance transform ('bwdist') for the binarized stack. To obtain a mask for watershed algorithm, we found regional minima of H-minima transform using 'imextendedmin' and imposed the extended minima voxels in the binarized stack using 'imimposemin'. We performed a watershed transform ('watershed') with the mask.

ELIMINATING FALSE BRANCH POINTS

Most of the rods in this step were still inappropriately segmented, and multiple rods that were close to each other were labeled as a single connected component. To eliminate those false branch points between individual rods, we first skeletonized the connected components using 'bwskel', and found the branch points using 'bwmorph3'. We performed another watershed transform with the updated mask that did not contain any branch points.

REPAIR PROCESS

Even after the branch removal, there were still many inappropriately segmented components. This is due to the usual watershed transform algorithm over-segmentation issue. Thus, we developed a custom algorithm for a repair process to merge lines that should have been labeled as a single component. This custom algorithm checks the distance between line endpoints, the angle between line directions, and the angle between the line direction and the direction from rod center to rod center. If these three values are lower than certain chosen values, the algorithm connects the over-segmented components into a single rod (see Figure 4.9 for a demonstration of this repair process).

5

Conclusion and Future Directions

In this dissertation, we presented a framework for studying interacting thin elastic rods using geometric, topological and mechanical methods. We then applied different facets of this framework to two interesting systems inspired by detangling hair and constructing a bird’s nest. We focused on one important aspect shared by both the hair and nest problems: physical entanglement. We showed results on the connections between the mechanical behavior and the topological properties of the models, including: force-displacement and the link current in the detangling of a double helix, and stress-strain behavior and the entanglement map in randomly packed rods. In this concluding section we will present ideas and preliminary results that can further explore our model systems and make for interesting future research directions.

DETANGLING REAL HAIR

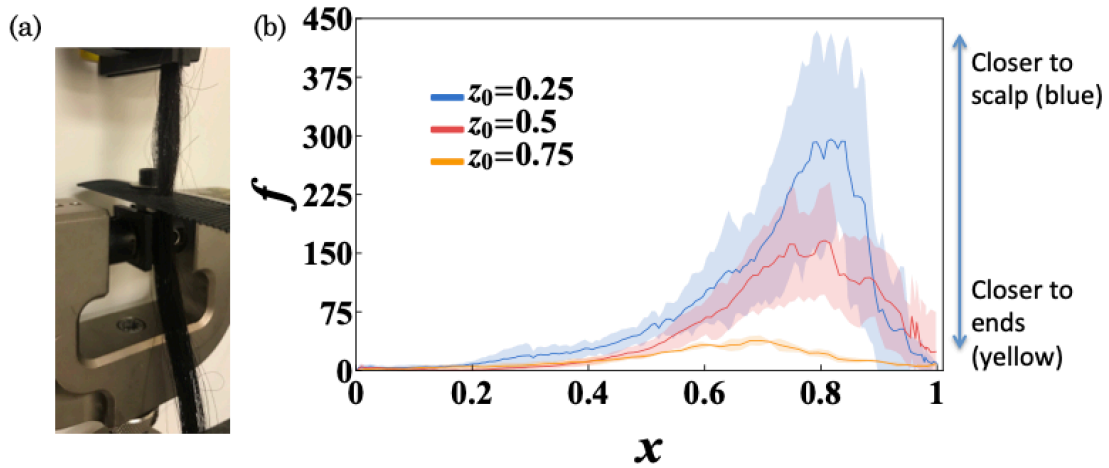


Figure 5.1: (a) Image of the experimental hair combing set up. A common pocket comb is fixed to an Instron testing machine and pulled downward through a curl of hanging hair (horse, in this case) from different starting heights. (b) Scaled force $f = \frac{r^2 F}{B}$ applied by pocket comb over scaled distance combed $x = \frac{d}{D}$, where F is unscaled force, d is unscaled distance combed, $r = 10^{-4}$ m is the characteristic radius of hair, B is the bending rigidity of hair and D is the total tine displacement through the hair curl. Different curves are different scaled starting heights $z_0 = \frac{D}{L}$ where $L = 20$ cm is the total length of the curl.

Building on the work from Chapter 2, we conducted some preliminary combing experiments

with curls of horse and human hair. Using an Instron 5566 material testing machine and a standard plastic pocket comb (Fig. 5.1(a)), we measured the force extension curves for different comb starting heights (Fig. 5.1(b)). The curls of hair were prepared by randomly jostling them while hanging under gravity to create groups of initially entangled hairs. Similar to the experimental and numerical results for combing a double helix (Fig. 2.4(a,b)), we see the obvious advantage in maximum force of starting the combing process closer to the free ends of the hairs. In Fig. 5.1(b), we can see that even repeating the yellow curve three times would be less total work than following the blue curve once (for the same total combing length). There are, however, some noticeable qualitative differences between the double helix minimal model and detangling real hair that merit further investigation. For example, the increasing region of each real hair force extension curve is noticeably longer (as a proportion of the total length of the curve) than for the double helix, and the region where the real hair curves level off is noticeably shorter. This could be due to more complex interactions between the many tines and many hairs of the pocket comb-hair curl system and potentially lower link density compared to the model system from Chapter 2. Our minimal model provides the basis for further experiments that could build new understanding and help further investigate questions related to the many-body interactions of entangled filaments.

TOPOLOGY OF CURLY HAIR

We focused our combing model on characterizing the detangling process in relatively straight hair ($1/\kappa \approx l$, where κ is the curvature of the hair and l is the length). We found (Fig. 2.1) that the majority of hair-hair interactions in the relatively straight regime were pairwise, which influenced our choice of the double helix as the minimal geometric model. For curlier hair types, the dominance of pair-wise interactions may not hold true. However, there are still topological invariants that could prove useful in characterizing higher order (3-, 4-, ..., n -body) interactions and that could shed

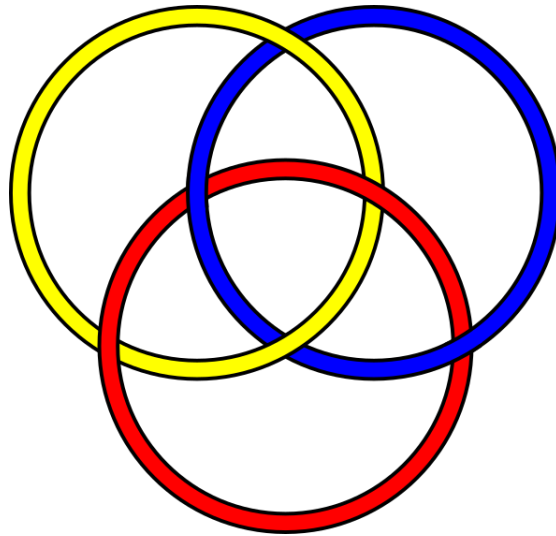


Figure 5.2: Borromean rings. The three rings together are linked topologically while no two pairs of rings are linked at all. This is the simplest example of a Brunnian link and one potential complex interaction that neighboring hairs could exhibit during detangling.⁴

light on the detangling process. One example of such a topological invariant is shown in Fig. 5.2, which shows a Borromean ring, the simplest version of a Brunnian link. A Brunnian link is any set of closed curves that are non-trivially linked but that become un-linked if any one of the curves is removed. Thinking back to the link counting rules laid out in Fig. 1.6, we can see that no two pairs of the curves in Fig. 5.2 are linked but that through their triplet interaction a topological invariant appears and they cannot be separated trivially. These types of interactions may be increasingly present in curlier hair types. Studying how they are removed mechanically (from some simplified higher order analogue to the double helix, for example) would help us model how detangling happens in a wider range of systems.

DISENTANGLING RANDOMLY PACKED RODS

In Chapter 3, we analyzed the relationship between small strains applied to randomly packed rods and internal changes in their geometry, topology and structure. We focused on how the internal

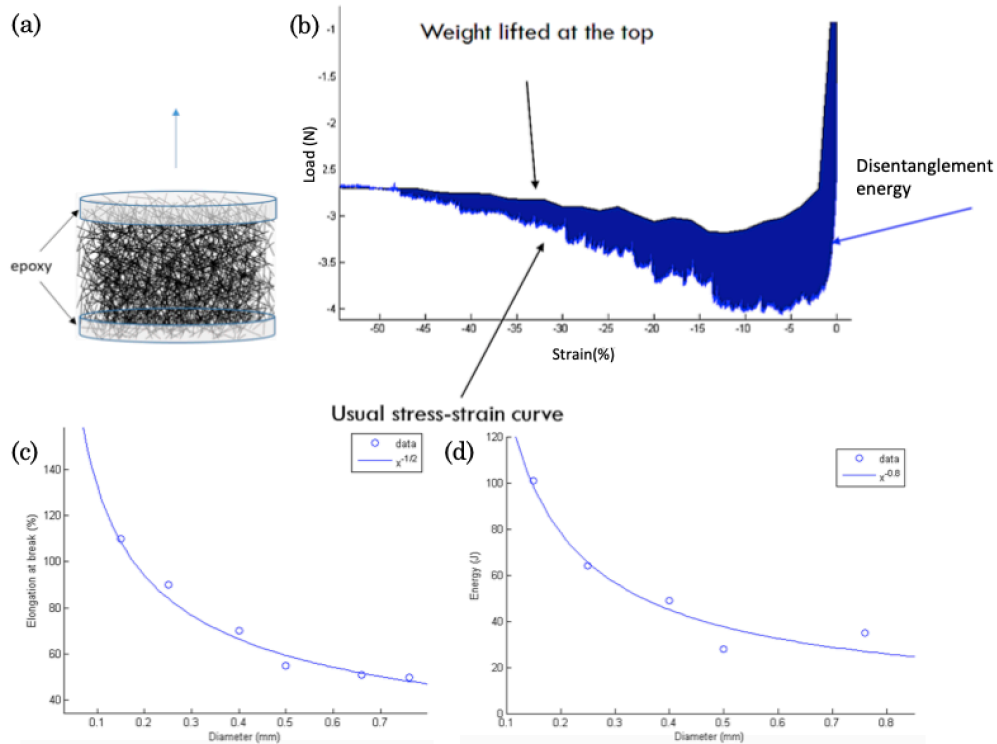


Figure 5.3: (a) Schematic of the randomly packed rods with attached petri dishes on the top and bottom that are then pulled apart in an Instron material testing machine. (b) Load-strain curve for disentangling the rods and weight of the top part of the rods as they are pulled upward by the Instron load cell. The difference between the two curves (highlighted in blue) represents the total disentanglement energy. (c) Elongation of the system of randomly packed rods when the top and bottom parts separate from each other for different individual rod diameters. Separation is defined as when the weight measured on the scale converges to the force measured by the load cell. (d) Total disentanglement energy measured for different individual rod diameters.

structure of the rods changed under mechanical compression. We can also ask how the same randomly packed rods respond to tensile strain. By attaching petri dishes with a few millimeters of epoxy to the top and bottom of the randomly packed rods (Fig. 5.3(a)), we were able to use an Instron material testing machine to pull apart the rods while measuring the applied force. We were interested in the force necessary to disentangle the rods, which we measured by using a scale to subtract the weight of the top section of rods hanging on the load cell during separation. We were also able to numerically integrate the difference between the load cell force and the weight of the hanging

rods to get the total disentanglement energy (Fig. 5.3(b)). We calculated this energy for different diameters of randomly packed rods and observed that the thinner, denser rods actually took more energy to disentangle even though they weighed less and the total force measured by the load cell was lower (Fig. 5.3(d)). We also measured how much the rods would extend before breaking apart and saw a similar inverse relationship with individual rod diameter (Fig. 5.3(c)). Connecting this mechanical data with quantitative observations of the internal geometry and topology of the rods (as in Chapter 4) would provide understanding of how the system responds to tensile strain. These experiments would involve a specialized setup that could simultaneously collect X-ray CT data and mechanical stress-strain data. With these insights we could more completely model, predict and design the properties of these types of entangled, packed materials.

References

- [1] 8, O. (2011). Torsion of a square section bar. CC BY 3.0.
- [2] Akkermans, R. L. & Warren, P. B. (2004). Multiscale modelling of human hair. *Philosophical Transactions of the Royal Society of London. Series A: Mathematical, Physical and Engineering Sciences*, 362(1821), 1783–1793.
- [3] Amir, A., Oreg, Y., & Imry, Y. (2012). On relaxations and aging of various glasses. *Proceedings of the National Academy of Sciences*, 109(6), 1850–1855.
- [4] AnonMoos (2006). The borromean rings are a link with the property that removing one ring unlinks the others. Public domain.
- [5] Archer, L. A. (1999). Polymer disentanglement in steady-shear flow. *Journal of rheology (New York : 1978)*, 43(6), 1617–1633.
- [6] Banerjee, H., Tse, Z. T. H., & Ren, H. (2018). Soft robotics with compliance and adaptation for biomedical applications and forthcoming challenges. *International Journal of Robotics and Automation*, 33(1).
- [7] Bao, Y. & Qi, Y. (2017). An image-based hair modeling and dynamic simulation method. *IEEE access*, 5, 12533–12544.
- [8] Berger, M. A. (1991). Generation of coronal magnetic fields by random surface motions. i : Mean square twist and current density. *Astronomy and astrophysics (Berlin)*, 252(1), 369–376.
- [9] Biddle, L. E., Broughton, R. E., Goodman, A. M., & Deeming, D. C. (2018). Composition of bird nests is a species-specific characteristic. *Avian Biology Research*, 11(2), 132–153.
- [10] Brieu, M., Diani, J., Mignot, C., & Moriceau, C. (2010). Stress softening of carbon black filled sbrs submitted to various large strain uniaxial tension cycles. *Procedia Engineering*, 2.
- [11] Buck, G. & Simon, J. (2012). The spectrum of filament entanglement complexity and an entanglement phase transition. *Proc. R. Soc. A Math. Phys. Eng. Sci.*, 468(2148), 4024–4040.
- [12] Calogreanu, G. (1959). *Rev. Math Pures Appl*, 4(5).

- [13] Carleton, J. B., Rodin, G. J., & Sacks, M. S. (2017). Layered elastomeric fibrous scaffolds: An in-silico study of the achievable range of mechanical behaviors. *ACS biomaterials science & engineering*, 3(11), 2907–2921.
- [14] Charles, N., Gazzola, M., & Mahadevan, L. (2019a). Topology, geometry, and mechanics of strongly stretched and twisted filaments: Solenoids, plectonemes, and artificial muscle fibers. *Phys. Rev. Lett.*, 123, 208003.
- [15] Charles, N., Gazzola, M., & Mahadevan, L. (2019b). Topology, geometry, and mechanics of strongly stretched and twisted filaments: Solenoids, plectonemes, and artificial muscle fibers. *Physical review letters*, 123(20), 208003–208003.
- [16] Cianchetti, M., Laschi, C., Menciassi, A., & Dario, P. (2018). Biomedical applications of soft robotics. *Nature Reviews Materials*, 3(6), 143–153.
- [17] Cosserat, E. & Cosserat, F. (1909a). *Theorie des Corps Deformables*. Paris, France: A. Hermann et Fils.
- [18] Cosserat, E. & Cosserat, F. (1909b). *Théorie des corps déformables*. Ithaca, N.Y.: Cornell University Library.
- [19] Călugăreanu, G. (1959). L'intégrale de Gauss et l'analyse des nœuds tridimensionnels. *Rev. Math. Pures Appl.*, 4, 5–20.
- [20] Daily-Diamond, C. A., Gregg, C. E., & O'Reilly, O. M. (2017). The roles of impact and inertia in the failure of a shoelace knot. *Proceedings of the Royal Society A: Mathematical, Physical and Engineering Sciences*, 473(2200), 20160770.
- [21] Diani, J., Fayolle, B., & Gilormini, P. (2009). A review on the Mullins effect. *European Polymer Journal*, 45.
- [22] Doi, M. & Edwards, S. F. (1978). Dynamics of rod-like macromolecules in concentrated solution. Part 1. *J. Chem. Soc. Faraday Trans. 2 Mol. Chem. Phys.*, 74(6), 560–570.
- [23] Fuller, F. B. (1971a). *Proc. Nat. Aca. Sci. USA*, 68(815).
- [24] Fuller, F. B. (1971b). The writhing number of a space curve. *Proceedings of the National Academy of Sciences - PNAS*, 68(4), 815–819.
- [25] Gauss, C. F. (1867). Complete works, fifth band. *Königliche Gesellschaft der Wissenschaften zu Göttingen*, (pp. 605).
- [26] Gazzola, M., Dudte, L. H., McCormick, A. G., & Mahadevan, L. (2018a). Forward and inverse problems in the mechanics of soft filaments. *Royal Society Open Science*, 5(6), 171628.

- [27] Gazzola, M., Dudte, L. H., McCormick, A. G., & Mahadevan, L. (2018b). Forward and inverse problems in the mechanics of soft filaments. *Royal Society open science*, 5(6), 171628–171628.
- [28] Gerbode, S. J., Puzey, J. R., McCormick, A. G., & Mahadevan, L. (2012). How the cucumber tendril coils and overwinds. *Science*, 337(6098), 1087–1091.
- [29] Gravish, N., Franklin, S. V., Hu, D. L., & Goldman, D. I. (2012). Entangled granular media. *Phys. Rev. Lett.*, 108, 208001.
- [30] Gupta, S. & Mazumdar, S. G. (2013). Sobel edge detection algorithm. *International journal of computer science and management Research*, 2(2), 1578–1583.
- [31] Gurtner, G. & Durand, M. (2009). Structural properties of stiff elastic networks. *Europhysics letters*, 87(2), 24001.
- [32] Gutierrez, H. M., Rust, J. P., & Seyam, A.-F. (1995). Modeling and simulation for control in carding. *Textile research journal*, 65(11), 638–643.
- [33] Hearle, J. W. S. & Morton, W. E. (2008). *Physical Properties of Textile Fibres*. Woodhead Publishing Series in Textiles. Cambridge: Elsevier Science & Technology.
- [34] Hirose, T., Fujioka, S., Mizuno, O., & Nakamura, T. (2012). Development of hair-washing robot equipped with scrubbing fingers. In *2012 IEEE International Conference on Robotics and Automation* (pp. 1970–1975): IEEE.
- [35] Iliffe, S., Haines, A., Gallivan, S., Booroff, A., Goldenberg, E., & Morgan, P. (1991). Assessment of elderly people in general practice. 2. functional abilities and medical problems. *Br J Gen Pract*, 41(342), 13–15.
- [36] Jim.belk (2007a). The four types of oriented link crossings. Public domain.
- [37] Jim.belk (2007b). Two curves with varying linking number. Public domain.
- [38] Kabla, A. & Mahadevan, L. (2007). Nonlinear mechanics of soft fibrous networks. *Journal of the Royal Society interface*, 4(12), 99–106.
- [39] Kamien, R. (1998). Local writhing dynamics. *The European physical journal. B, Condensed matter physics*, 1(1), 1–4.
- [40] Kamien, R. D. (2002). The geometry of soft materials: a primer. *Rev. Mod. Phys.*, 74, 953–971.
- [41] Leaf, G. A. V. & Oxenham, W. (1981). 16-the compression of yarns part i: The compression-energy function. *The Journal of The Textile Institute*, 72(4), 168–175.

- [42] Lee, M. E. M. & Ockendon, H. (2006). The transfer of fibres in the carding machine. *Journal of engineering mathematics*, 54(3), 261–271.
- [43] Liu, A. J. & Nagel, S. R. (2010). The jamming transition and the marginally jammed solid. *Annual Review of Condensed Matter Physics*, 1(1), 347–369.
- [44] Love, A. (1944). *A Treatise on the Mathematical Theory of Elasticity*. New York: Dover, 4th edition.
- [45] Love, A. E. H. (1920). *A treatise on the mathematical theory of elasticity*. Cambridge [Eng.]: At the University Press, 3d ed. edition.
- [46] McCormick, A. (2013). Discrete geometry and physics of elastic curves.
- [47] NatureFramingham (2020). Osprey Nest on Human Built Structures. CC.
- [48] Nelson, D. R. (2004). Vortices weave a tangled web. *Nature (London)*, 430(7002), 839–840.
- [49] Onoda, G. Y. & Liniger, E. G. (1990). Random loose packings of uniform spheres and the dilatancy onset. *Phys. Rev. Lett.*, 64, 2727–2730.
- [50] O’Reilly, O. M. (2017). *Modeling Nonlinear Problems in the Mechanics of Strings and Rods: The Role of the Balance Laws*. Interaction of mechanics and mathematics. Cham: Springer International Publishing AG.
- [51] Pan, N. (1992). Development of a constitutive theory for short fiber yarns: Mechanics of staple yarn without slippage effect. *Textile research journal*, 62(12), 749–765.
- [52] Panaitescu, A., Grason, G. M., & Kudrolli, A. (2017). Measuring geometric frustration in twisted inextensible filament bundles. *Physical review. E*, 95(5), 052503–052503.
- [53] Patil, V. P., Sandt, J. D., Kolle, M., & Dunkel, J. (2020). Topological mechanics of knots and tangles. *Science (American Association for the Advancement of Science)*, 367(6473), 71–75.
- [54] Pfadenhauer, M. & Dukat, C. (2015). Robot caregiver or robot-supported caregiving? *International Journal of Social Robotics*, 7(3), 393–406.
- [55] Philipse, A. P. (1996). The Random Contact Equation and Its Implications for (Colloidal) Rods in Packings, Suspensions, and Anisotropic Powders. *Langmuir*, 12(24), 5971–5971.
- [56] Plumb-Reyes, T., Charles, N., & Mahadevan, L. (2021). Combing a double helix. arXiv:2103.05211.
- [57] Poincloux, S., Adda-Bedia, M., & Lechenault, F. (2018). Geometry and elasticity of a knitted fabric. *Physical review. X*, 8(2), 021075.

- [58] Polygerinos, P., Wang, Z., Galloway, K. C., Wood, R. J., & Walsh, C. J. (2015). Soft robotic glove for combined assistance and at-home rehabilitation. *Robotics and Autonomous Systems*, 73, 135–143.
- [59] Popletibus (2016). Illustration of the frenet frame. CC BY-SA 4.0.
- [60] rabbit, S. (2007). The frenet-serret frame moving along a helix in space. CC BY-SA 4.0.
- [61] Rheude, M. (2020). Eagle Nest: Closeup. USFWS.
- [62] Ricca, R. L. & Nipoti, B. (2011). Gauss' linking number revisited. *Journal of knot theory and its ramifications*, 20(10), 1325–1343.
- [63] Robinson, H., MacDonald, B., & Broadbent, E. (2014). The role of healthcare robots for older people at home: A review. *International Journal of Social Robotics*, 6(4), 575–591.
- [64] Robinson, V. (1976). A study of damaged hair. *J Soc Cosmet Chem*, 27, 155–161.
- [65] Rosenblum, R. E., Carlson, W. E., & Tripp III, E. (1991). Simulating the structure and dynamics of human hair: modelling, rendering and animation. *The Journal of Visualization and Computer Animation*, 2(4), 141–148.
- [66] Rus, D. & Tolley, M. T. (2015). Design, fabrication and control of soft robots. *Nature*, 521(7553), 467–475.
- [67] S. Cantournet, R. Desmorat, J. B. (2009). Mullins effect and cyclic stress softening of filled elastomers by internal sliding and friction thermodynamics model. *International Journal of Solids and Structures*, 46.
- [68] Shibata, M. & Hirai, S. (2006). Soft object manipulation by simultaneous control of motion and deformation. In *Proceedings 2006 IEEE International Conference on Robotics and Automation, 2006. ICRA 2006*. (pp. 2460–2465).: IEEE.
- [69] Stevens, K. A. (1981). The information content of texture gradients. *Biological cybernetics*, 42(2), 95–105.
- [70] Swift, K. (2020). Crow/Raven. Corvid Research.
- [71] Tal, E. J. (2016). Dyed wool carded at jamieson mill. CC BY-SA 4.0.
- [72] Tapadia, P. & Wang, S. (2003). Yieldlike constitutive transition in shear flow of entangled polymeric fluids. *Physical review letters*, 91(19), 198301–198301.
- [73] Topping, M. (2002). An overview of the development of handy 1, a rehabilitation robot to assist the severely disabled. *Journal of intelligent and robotic systems*, 34(3), 253–263.

- [74] Topping, M. J. & Smith, J. K. (1999). The development of handy 1. a robotic system to assist the severely disabled. *Technology and Disability*, 10(2), 95–105.
- [75] Török, T. & Kliem, B. (2005). Confined and ejective eruptions of kink-unstable flux ropes. *The Astrophysical Journal*, 630(1), L97–L100.
- [76] van der Heijden, G. & Thompson, J. (2000). *Nonlinear dynamics*, 21(71).
- [77] Vickispix (2020). Red-Tailed Hawk Nests. CC.
- [78] Ward, K., Bertails, F., Kim, T.-Y., Marschner, S., Cani, M.-P., & Lin, M. (2007). A survey on hair modeling: Styling, simulation, and rendering. *IEEE transactions on visualization and computer graphics*, 13(2), 213–234.
- [79] Warren, P. B., Ball, R. C., & Goldstein, R. E. (2018). Why clothes don’t fall apart: Tension transmission in staple yarns. *Physical review letters*, 120(15), 158001–158001.
- [80] Weiner, N., Bhosale, Y., Gazzola, M., & King, H. (2020). Mechanics of randomly packed filaments—the “bird nest” as meta-material. *Journal of Applied Physics*, 127(5), 050902.
- [81] White, J. H. (1969a). *Am. J. Math*, 91(693).
- [82] White, J. H. (1969b). Self-linking and the gauss integral in higher dimensions. *American journal of mathematics*, 91(3), 693–728.
- [83] Witz, G. & Stasiak, A. (2009). DNA supercoiling and its role in DNA decatenation and unknotting. *Nucleic Acids Research*, 38(7), 2119–2133.
- [84] Wolgemuth, C., Powers, T., & Goldstein, R. (2000). Twirling and whirling: Viscous dynamics of rotating elastic filaments. *Physical review letters*, 84(7), 1623–1626.
- [85] Zhao, Y., Liu, K., Zheng, M., Barés, J., Dierichs, K., Menges, A., & Behringer, R. P. (2016). Packings of 3d stars: stability and structure. *Granular Matter*, 18.



THIS THESIS WAS TYPESET using \LaTeX , originally developed by Leslie Lamport and based on Donald Knuth's \TeX . The body text is set in 12 point Egenolff-Berner Garamond, a revival of Claude Garamont's humanist typeface. The above illustration, "Science Experiment 02", was created by Ben Schlitter and released under [CC BY-NC-ND 3.0](#). A template that can be used to format a PhD thesis with this look and feel has been released under the permissive [MIT \(X11\)](#) license, and can be found online at github.com/suchow/Dissertate or from its author, Jordan Suchow, at suchow@post.harvard.edu.